SURFACE-TUNABLE PHOTOLUMINESCENCE AND NONLITHOGRAPHIC PATTERNING OF BLOCK COPOLYMER-STABILIZED CADMIUM SULFIDE QUANTUM DOTS

By

Chih-Wei Wang
B.Sc., The University of British Columbia, 2002

A Thesis Submitted in Partial Fulfillment of the
Requirements for the Degree of

MASTER of SCIENCE

in the Department of Chemistry

ABSTRACT

The static and time-resolved photoluminescence properties of polystyrene-*b*-poly(acrylic acid) (PS-*b*-PAA)-stabilized cadmium sulfide quantum dots (CdS QDs) are characterized for the first time, demonstrating tunable emission spectra and quantum yields via different chemical treatments of the PAA layer at the QD surface. Samples with the PAA layer in its cadmium carboxylate form show more intense band-edge emission, relatively high quantum yields, and impressive long-term stability compared to samples in which the PAA layer is in its acid form. In addition, a new and versatile nonlithographic strategy for the lateral patterning of these polymer-stabilized CdS QDs in thin polymer films is demonstrated, involving simple spin-coating of polymer blend solutions and the resulting phase separation between the PS brush layer surrounding the QDs and a poly(methyl methacrylate) (PMMA) homopolymer. Subsequent selective removal of the PMMA component allows the production of various photoluminescent PS/QD features with structural hierarchy on glass substrates, including cellular and wire-like networks and arrays of spatially correlated islands. Finally, the polymer compatibility and photoluminescence of PS-*b*-PAA-stabilized QDs is utilized to demonstrate their application as fluorescent tracers for laser scanning confocal fluorescence microscopy (LSCFM) imaging of phase morphology in PS/PMMA polymer blends.

Supervisor: Dr. Matthew Moffitt, (Department of Chemistry)

Acknowledgements

I would like to express my most sincere thanks to Professor Matthew Moffitt first for introducing me to this fascinating area of chemistry, the hybrid area of polymer and nano science, and second for his thorough guideness throughout the course of this work. I am also very grateful to him for his constant encouragement, patience and support; in addition, his scientific attitude, insights and boundless enthusiasm has a tremendous positive effect on me.

I would also like to specially thank my parents for raising and educating me, making sacrifices in order to give the best they could to me. I would also like to thank my younger brother for looking after my parents while I am away from home. I can never thank them enough

I would also like to thank Jenny for the positive influence she had on me academically and also for her endless love, care, patience, support and forgiveness for the past years. Thank you for everything, Jenny.

In addition, I would like to thank:

Dr. Subhajit, Bandyopadhyay, who was a senior fellow graduate student in the Petch lab during the time when most of the work was carried out, for many useful discussions, constant encouragement, friendship, wisdom and delicious food.

My group members, Huda Yusuf, Rob Cheyne, and Yunyong Guo for many useful discussions on the research and also being supportive and reliable group members.

Dr. Frank van Veggel for kindly sharing the instruments and also for many useful discussions on the fluorescence data. Dr. Frank van Vegeel's group members, Peter Diamente, Sri Sivakumar, Dr. Venkataramanan Mahalingam and Dr. V Sudarsan for many useful discussion on the various aspects of the nanoparticle research and also for their instrumental technical supports.

People in the Petch lab for making the lab a pretty nice place to spend so many hours for so many days

Employees in the chemistry department for making the department feel just like home.

Brent Gowen in the electron microscopy laboratory for his tremendous help with TEM imaging.

Table of Contents

List of Schemes and Figures

List of Tables

CHAPTER 1

GENERAL INTRODUCTION

1.1 . Introduction

Colloidal semiconducting nanoparticles, or quantum dots (QDs), have attracted a great deal of interest in recent years, due to their size-dependent optical and electronic properties, which arise from quantum confinement and surface effects.[1-6] In particular, the intense and size-tunable light emission exhibited by colloidal II/IV semiconductors (e.g. CdS, CdSe) have made these nanoparticles intriguing candidates as fluorescent bio-labels, or as functional elements in materials with potential applications in photonics, electroluminescence, and sensing. A key issue behind the synthesis of colloidal QDs is their functionalization with appropriate organic ligands.[7] This organic surface layer provides the inorganic nanoparticles with solubility, stability, and processability in a range of organic media through favorable interactions with the surrounding environment. As well, specific interactions between the organic layer and the nanoparticle surface can play an important role towards passivating trap states caused by surface defects, thus optimizing photoluminescence quantum yields.[7-11]

Critical to their application in functional materials and devices is the ability to control the spatial distribution of nanoparticles, by either self-assembly (bottom-up) or lithographic (top-down) methods, since the ordering of quantum dots on various length scales from nanometer to micrometer dimensions will determine the collective properties of the assembly. The collective behaviour of nanoparticle assemblies arises from a wide range of effects operating on different length scales, including dipole-dipole coupling between nanoparticles and photonic bandgap effects.[3,12] Another important requirement for many quantum dot-based devices is the incorporation of quantum dots into a polymer matrix, where the quantum dots provides optical and electronic activity, and the polymer

provides a processable medium with desirable mechanical and optical properties. However, the controlled distribution of quantum dots in polymer systems has proven to be extremely challenging, since typical preparative methods produce nanoparticles with low-molecular weight surface ligands, which undergo uncontrolled aggregation due to their insolubility in most polymers.[9,13]

A promising route for addressing the challenges of dispersion and controlled organization of quantum dots in polymers is the production of discrete colloidal building blocks consisting of inorganic nanoparticles stabilized with a polymeric surface layer. In this "building block" approach, an appropriate polymer layer can result in excellent dispersion of nanoparticles in a polymer matrix,[14] or controlled self-assembly of QDs via steric repulsions between approaching polymer brushes, resulting in ordered nanocomposites.[15] A relatively direct and efficient route to polymer-coated quantum dots has been developed by Moffitt et al,[16] in which cadmium sulfide (CdS) nanoparticles were synthesized in the poly(cadmium acrylate) cores of a polystyrene-*b*-poly(cadmium acrylate) (PS-*b*-PACd) block ionomer micelle, resulting in colloidal CdS QDs with a polyacrylic acid (PAA) surface layer and an outer PS brush layer. In order to utilize such PS-*b*-PAA-stabilized QDs as building blocks for self-assembled functional materials and devices, a detailed knowledge of the photoluminescent properties and structure of the individual hybrid nanoparticles dispersed in dilute solutions is required. Such a study comprises the first part of this work, which demonstrates unique control of photoluminescence and structure via simple chemistry in the PAA layer of block copolymer stabilized CdS QDs. The second part of this thesis explores a new strategy for the controlled self-assembly of these hybrid building blocks on glass substrates, via

simple spin-coating of blends of PS-*b*-PAA-stabilized QDs and PMMA homopolymer; the resulting nanocomposite surface structures exhibit tunable organization on two disparate length scales, with micron-scale patterns determined by a polymer/polymer phase separation process, and nanoscale ordering of QDs determined by steric interactions between the PS brushes surrounding each nanoparticle. Finally, the third part of the thesis demonstrates an entirely different application of these polymer-stabilized QDs, showing their use as novel photoluminescent tracers for fluorescence imaging of polymer blend morphology.

The principle characterization techniques employed in this work are static and time-resolved fluorescence spectroscopy, UV-vis absorption spectroscopy (UV-vis), static and dynamic light scattering (SLS, DLS), transmission electron microscopy (TEM), atomic force microscopy (AFM) and laser scanning cofocal fluorescence microscopy (LSCFM).

The present chapter is divided into 5 sections. The reminder of section 1.1 is devoted to a general introduction of polymers and block copolymers including a discussion of the synthesis and characterization of block copolymers. Section 1.2 concerns the self-assembly of block copolymers and block ionomers in selective solvents to form micelles. Section 1.3 consists of an introduction to semiconducting nanoparticles (quantum dots) along with a description of the quantum-confinement effect. In section 1.4, the three principle imaging techniques, AFM, LSCFM, and TEM, which are employed in this thesis for characterizing the organization of QDs on multiple length scales, are described. The final section is a summary of the content of the remaining chapters of the thesis.

1.1.1. General Background

A *polymer* is a large molecule built up via the covalent linking of numerous smaller molecules which are termed *monomers*.[17] Depending on the number of bonding sites on the constituent monomers, different polymer structures such as linear, branched, or highly interconnected networks can be achieved. Once monomers are incorporated into polymer chains, they are known as *repeat units* and the number of repeat units in a polymer chain is called the *degree of polymerization.*

When only one species of monomer is used to produce a polymer, the product is called a *homopolymer*, normally referred to simply as a polymer.[18] If more than one type of monomer is used, then the product is a *copolymer*, in which a variety of arrangements of the repeat units are possible. If two distinct monomers, A and B, are considered, it is possible to describe four main categories of copolymers (Figure 1.1). In a *statistical copolymer*, also called a *random copolymer*, the distribution of A and B repeat units in the polymer chain is essentially random, although the composition will be influenced by the individual monomer reactivities. In an *alternating copolymer,* there is an alternating placement of A and B units along the chain. When strands (or sequences, or blocks) of A repeat units are connected to strands of B repeat units in a linear chain, the resulting copolymer is called a *block copolymer*. In the simplest case, when one block of A repeat units is linked by a single covalent bond to a block of B repeat units, the resulting copolymer is called a *diblock copolymer.* It is obvious that depending on the number of blocks of monomer A and B which are joined together, *triblock* and *polyblock* copolymers are also possible. Finally, *graft copolymers* are copolymers in which blocks of one repeat unit are grafted along a backbone of the other repeat unit in a branch-like

fashion. Since the work described in this thesis concerns an application of diblock copolymer self-assembly, this type of copolymer will be discussed in more detail in the following sections.

AABAAAABBBAABABABAABAA	Random copolymer
ABABABAABABABABABABABA	Alternating copolymer
AAAAAAAAAAABBBBBBBBBBB	Block copolymer
AAAAAAAAAAAAAAAAAAAAA	Graft copolymer

```
B     B
B     B
B     B
B     B
B
```

Figure 1.1. Types of copolymers synthesized from monomers A and B.

1.1.2. Synthesis of Block Copolymers: Sequential Anionic Polymerization

Anionic polymerization was first discovered by Szwarc[19] in 1956, and since then it has become the most common technique for the preparation of block copolymers, since block copolymers prepared by this method have well-defined and relatively narrow molecules weight distributions.[20] Anionic polymerization involves three steps: initiation, propagation, and termination.[21] In the initiation step, electronegative monomers are activated by a highly electropositive initiator, forming anionic reactive centers. During the propagation step, polymerization proceeds by a consecutive addition of the monomers.

Since the polymerization process has no formal termination step, a "living polymer" is said to be created and the propagation step should continue until all of the monomer is consumed. The polymerization can be resumed if more monomer is added to the system and thus the degree of polymerization can be controlled. Block copolymers of the desired composition can therefore be obtained by introducing a second monomer to the system after the complete consumption of the first monomer. In the termination step, the living polymer is "killed" by adding a small molecule with a labile proton such as methanol.

Because most of the work described in this thesis was carried out using the diblock copolymer polystyrene-*b*-poly(*tert*-butylacrylate) (PS-*b*-PtBA) as the starting material, its synthesis is of particular relevance to this thesis and will be discussed in more detail here. In anionic polymerization, the presence of water and oxygen molecules is highly undesirable as they will react with polycarbanions to terminate the living chains. Therefore, every step during the synthesis was carried out under an atmosphere of ultra-pure nitrogen, and with careful drying of all glassware.

The anionic polymerization of PS-*b*-PtBA is carried out in tetrahydrofuran (THF) solution, in the presence of α-methylstyrene and LiCl; α-methylstyrene serves both as a colour indicator and an end-capping agent, and LiCl is a stabilizer for the polymerization reaction.[22-24] In the initiation step (Scheme 1.1), a solution of α-methylstyrene and LiCl is titrated with the initiator *sec*-butyllithium (*sec*-BuLi) at room temperature until a light red colour persists, followed by the complete addition of the desired amount of initiator. During the titration step, *sec*-BuLi first reacts with any impurities (e.g. H_2O) in the system, and then activates α-methylstyrene to yield short polycarbanions of a deep red colour **(1)**. Therefore, the persistence of a light red colour during titration with *sec*-BuLi

indicates that a trace amount of α-methylstyrene has been activated and that all of the impurities have been removed.

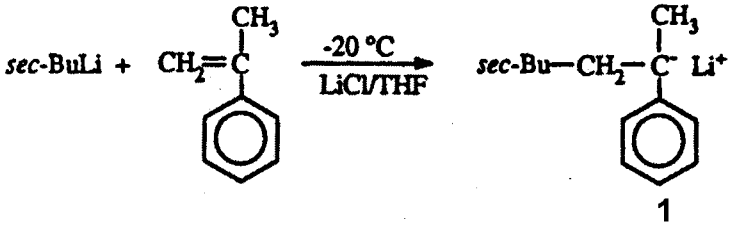

Scheme 1.1. Reaction of *sec*-butyllithium with α-methylstyrene.

In the propagation step (Scheme 1.2), the reaction mixture is first cooled to -78 °C, followed by the dropwise addition of the styrene monomer. The dark red colour of the initiator solution from **1** changed quickly to a deep orange-yellow colour, indicating the presence of "activated" styrene. The active centers are regenerated at the chains ends as the polymerization proceeds, and the process continues until all of the styrene monomer is consumed. The complete consumption of the styrene monomer is indicated by the colour change from deep orange-yellow back to dark red, as the remaining α-methylstyrene in solution "caps" the end of the living chain ends, forming **2** (Scheme 1.2).

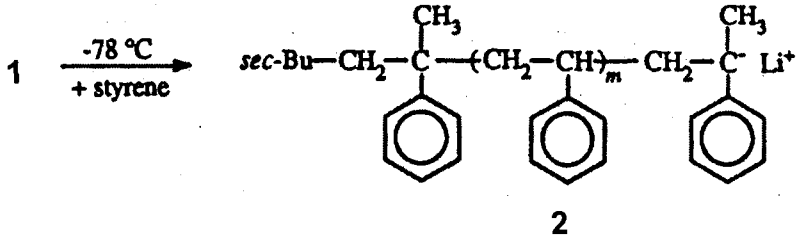

Scheme 1.2. Reaction of short polycarbanions of activated α-methylstyrene with styrene monomers.

The polymerization resumes when the second monomer, *tert*-butylacrylate, is added to the reaction mixture. The deep red colour associated with the active α-methylstyrene chain ends quickly disappears upon the addition of *tert*-butylacrylate, since activated *tert*-butylacrylate is colourless **(3)**. The presence of the α-methylstyrene end-cap serves to sterically regulate the initiation of the highly reactive *tert*-butylacrylate monomer. As well, unwanted side reactions such as reactions with the ester functional group or chain transfer reactions are prevented by the LiCl stabilizer, which associates with the living chain ends, thus lowering their reactivity.[22-24]

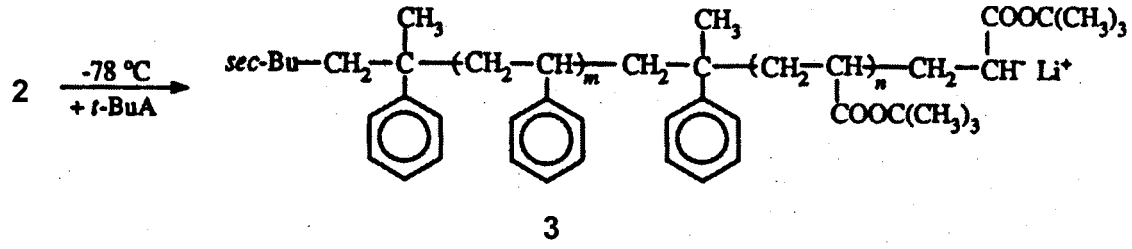

3

Scheme 1.3. Reaction of **2** with *tert*-butylacrylate monomers to give PS-*b*-PtBA diblock copolymer.

In the final step, the polymerization is terminated by the addition of a small amount of methanol. The final PS-*b*-PtBA diblock copolymer is recovered by precipitation into methanol.

1.1.3. Characterization of Block Copolymers

Once a block copolymer is synthesized, certain characteristics of the polymer must be determined before further experiments are performed. The most important

parameters that define a given block copolymer are composition, average molecular weight and polydispersity index.

The composition of a block copolymer is defined by the relative block lengths of each block and is usually expressed as a weight or mole fraction of either block. Techniques such as nuclear magnetic resonance spectroscopy (NMR) or infrared spectroscopy (IR)[23,25] can be employed for determining the composition of a block copolymer quantitatively, providing that either monomer shows a well-defined resonance or absorption mode. For example, determination of the PtBA content in the diblock copolymer PS-*b*-PtBA mentioned above is usually carried out by FTIR, since the carbonyl C=O of PtBA gives a very strong and narrow absorption band in the infrared region at 1730 cm^{-1}. The procedure consists of calibrating a KBr cell with solutions of PtBA homopolymer of various concentrations in carbon tetrachloride (CCl_4), then determining the absorbance at 1730 cm^{-1} (A_{1730}) for a solution of the copolymer PS-*b*-PtBA of known concentration in the same cell.[23] In order to obtain the extinction coefficient of the C=O, A_{1730} is plotted as a function of the concentration of PtBA homopolymer; a straight line is obtained, as expected from the Beer-Lambert law. The extinction coefficient ε is obtained from the slope and the weight fraction of poly(*tert*-butylacrylate) in the copolymer can be calculated from $f_{PtBA} = A_{1730}/(\varepsilon * C)$, where C is the copolymer concentration in g/L.

One of the most important features which distinguishes a synthetic polymer from a small molecule is the lack of a single, well-defined molecular weight. This is a consequence of the statistical nature of any polymerization process.[18,25] For example, in a polycondensation reaction, the final length of a given chain depends on the availability of

a suitable reactive group; in an addition polymerization reaction, the lifetime of the chain carrier will determine the chain length. As a result of the statistical nature of these factors, the product is a mixture of chains of differing lengths, i.e. a distribution of chain lengths. Therefore, the polymer is characterized best by a molecular weight distribution, such as that shown in Figure 1.2.[26]

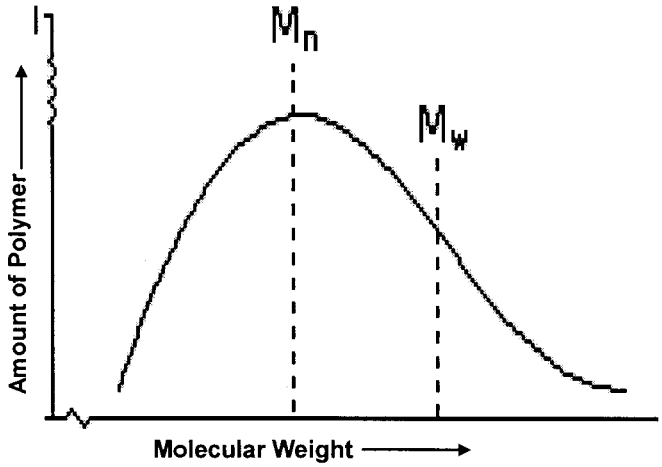

Figure 1.2. An example of a typical distribution of molecular weight for a synthetic polymer sample.[26]

For a given molecular weight distribution, one can define different types of averages as shown in Figure 1.2. The number-average molecular weight M_n is defined by:

$$M_n = \frac{\sum_i N_i M_i}{\sum_i N_i} = \frac{\sum_i W_i}{\sum_i (W_i/M_i)} \qquad (1.1)$$

Where N_i is the number of molecules of species i with molecular weight M_i, and W_i is the

weight of all molecules of species i with molecular weight M_i . As can be seen from this mathematical expression, M_n is sensitive to the number of molecules of each species present in the system, and can therefore be determined by techniques that are dependent on colligative properties such as osmotic pressure. On the other hand, the weight-average molecular weight, M_w, is generally determined from light scattering measurements, in which each molecule or chain makes a contribution to the average intensity of scattered light relative to its size. This average is more heavily weighted to the larger molecules in the distribution than is the number-average molecular weight. M_w is defined as

$$M_w = \frac{\sum_i W_i M_i}{\sum_i W_i} = \frac{\sum_i N_i M_i^2}{\sum_i N_i M_i} \qquad (1.2)$$

The breadth of the molecular weight distribution of a polymer can be gauged from the polydispersity index (PI), which is defined as:

$$PI = \frac{M_w}{M_n} \qquad (1.3)$$

A sample with a high value of PI is said to be polydisperse. The lowest possible value of PI is unity and in such a case the sample is said to be monodisperse. For many polymerizations, for example condensation polymerization, the most probable PI value is about 2. In contrast, for polymers synthesized by sequential anionic polymerization, PI

values between 1.05 and 1.10 are commonly obtained and values even as low as 1.01 have been achieved.[23,27]

For convenience, the number-average degree of polymerization (N) per chain, rather than the average molecular weight of a polymer, is commonly reported and is given by:

$$N = \frac{M_n}{M_0} \qquad (1.4)$$

Where M_n is the number-average molecular weight and M_0 is the molecular weight of the repeat unit.

1.2. Block Copolymer Micelles

Much of the increasing interest in block copolymers is due to from their unique solution properties, which arise from their tendency to self-assemble in solution forming block copolymer micelles. Along with the application of block copolymer micelles to the synthesis and stabilization of inorganic nanoparticles, such as that presented in this thesis, block copolymer micelles have received an enormous amount of attention for other potential applications, including controlled drug delivery, solubilization of insoluble substances, medical diagnostic imaging, and many others. In this section, a brief introduction to block copolymer micellization is first presented, followed by a general description of the characterization of block copolymer micelles. Some relevant theories of block copolymer micelle structure and scaling relations are then presented, followed by a discussion of block ionomer micelles.

1.2.1. Micellization of Block Copolymers

The term *selective solvent* for a block copolymer refers to a solvent that is a thermodynamically good solvent for one block, but a poor solvent for the other block. When the concentration of block copolymers in a selective solvent reaches a certain level, known as the critical micelle concentration (CMC), the copolymer chains self-assemble to form micellar aggregates. The structure of the micelles consists of a core of the insoluble blocks surrounded by a flexible fringe of soluble blocks known as the corona. The micellization of block copolymers in selective organic solvents is enthalpically driven as the insoluble blocks aggregate to minimize less favourable interactions with the solvent.

It is worth mentioning that although micellization is an equilibrium process, severe chain entanglement within the core can retard the entrance and exit of single chains, providing kinetic stability against micelle dissociation. The kinetics of chain disentanglement is stalled even more drastically when the core-forming blocks are below their glass transition temperature (T_g); in such cases, block copolymer micelles are said to be "frozen" or "dead", as no dynamic equilibrium exists on a reasonable time scale. The terms aggregate and aggregation, which generally refer to non-reversible processes, are thus often applied to the micellization of block copolymers, although micelles of this type can exhibit a dynamic equilibrium in some cases. In contrast, the terms "associate" and "association" imply complete reversibility, and are usually reserved for the micellization of small molecule surfactants.

In many cases, block copolymer micelles are spherical in shape, although a large number of examples of non-spherical block copolymer micelles have been reported

recently.[28] Depending on the length of the insoluble (core-forming) block compared to the soluble (corona-forming) block, block copolymer micelles are usually classified into two types: 1) star-like micelles and 2) crew-cut micelles.[29,30] In star-like micelles, the length of the corona-forming blocks (soluble blocks) are much larger than the length of the core-forming blocks (insoluble blocks). Therefore star-like micelles have small and compact insoluble cores surrounded by coronae of long soluble blocks that extend into the solution. Crew-cut micelles, on the other hand, have relatively short soluble blocks compared to the insoluble blocks, such that the micelles have large cores and relatively thin coronae (Figure 1.3).

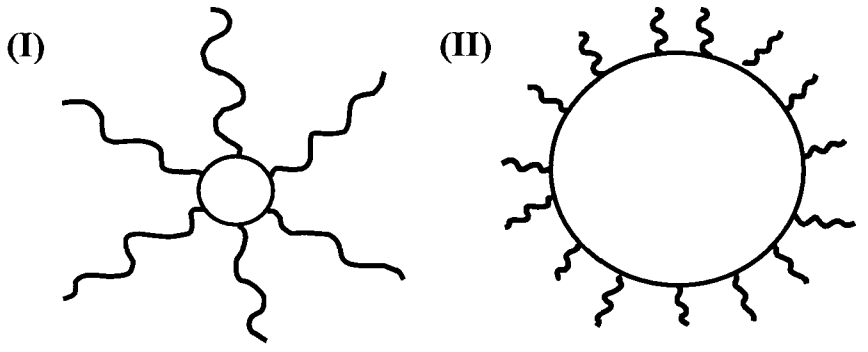

Figure 1.3. Schematic diagram of star-like (I) and crew-cut (II) micelles.

The micellization of block copolymers generally occurs via a closed association process.[29,31] Closed association is characterized by a single equilibrium between unimers (isolated molecules) and micelles of a well-defined aggregation number Z (molecules per aggregate):

$$ZM_1 \underset{C>CMC}{\longleftrightarrow} M_z \qquad (1.5)$$

In this case, the micelles have a very low polydispersity in molecular weight and size. In contrast, the association of small molecule surfactants is generally described by a so-called open association process. The characteristic feature of an open association process is that there are several equilibria between species of different sizes described by the following equations:

$$\begin{aligned} M_1 + M_1 &\leftrightarrow M_2 \\ M_2 + M_1 &\leftrightarrow M_3 \\ M_3 + M_1 &\leftrightarrow M_4 \\ &\cdots \\ M_N + M_1 &\leftrightarrow M_{N+1} \end{aligned} \qquad (1.6)$$

Therefore, depending on the relative values of the individual equilibrium constants, supramolecular species (M_2, M_3,...,M_N) with different aggregation numbers can be present simultaneously in the solution. To further illustrate the difference between a closed and open association process, the inverse apparent average molecular weight of the species in solution can be plotted versus solute concentration in each case.[31] In the closed association model, three regimes can be identified (Figure 1.4a). In regime I, only unimers exist. In region II, there is coexistence of unimers and micelles. The concentration at which micelles first appear is by definition the CMC. The micelle concentration increases as concentration increases until region III is reached where most of the unimers have been incorporated into the micelles. In this region, the properties of the solution are dictated almost entirely by the properties of the micelles. In the case of open association (Figure 1.4b), no CMC exists, and there is a continuous change in properties with concentration.

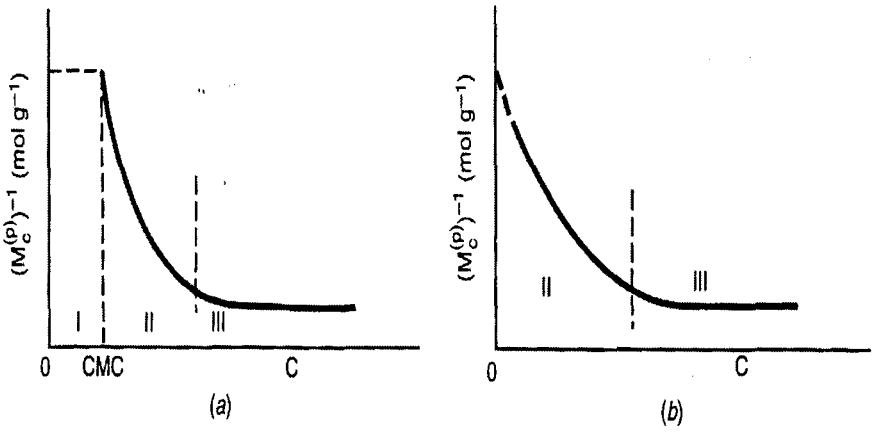

Figure 1.4. Concentration-dependence of reciprocal molecular weight in associating systems obeying the models of closed (a) and open (b) association.

1.2.2. Characterization of Block Copolymer Micelles

The characterization of block copolymer micelles is a rather challenging task because generally a combination of methods is required to obtain the desired data. Numerous physicochemical methods have been employed to characterize block copolymer micelles in terms of their CMC, aggregation number, structure, hydrodynamic properties, and size distribution. Techniques that are used to characterize various aspects of block copolymer micelles include size-exclusion chromatography (SEC), transmission electron microscopy (TEM), static and dynamic light scattering (SLS and DLS), nuclear magnetic resonance (NMR), fluorescence spectroscopy, and many others; the application of many of these methods will be discussed in this thesis. For a detailed review regarding the characterization of block copolymer micelles, the readers are recommended to see the references cited.[29,32]

1.2.3. Theories of Block Copolymer Micelles

Over the past 20 years, several studies have targeted theoretical aspects of diblock copolymer micelles in selective solvents.[33-38] The aim of these theoretical studies was to establish correlations, or "scaling laws", between the molecular characteristics of a given block copolymer, and the various structural parameters of the resulting micelles, such as the core radius, R_c, the corona thickness, L, and the aggregation number, Z. In these theories, expressions for the total Gibbs free energy of a micelle are written as a sum of several enthalpic and entropic contributions, including those pertaining to the core, the corona and the core/corona interface. Minimization of these equations with respect to parameters characterizing the micelles allows one to determine the dependence of R_c, L and Z on the number of repeat units in the insoluble and soluble blocks, N_B and N_A, respectively.

In their general form, scaling laws for the aggregation number and core radius for block copolymer micelles can be written as shown in eq.1.7

$$Z \sim N_B^{\alpha} N_A^{-\beta}$$
$$R_{core} \sim N_B^{\kappa} N_A^{-\gamma} \qquad (1.7)$$

where N_A and N_B are the number of repeat units in the soluble and insoluble blocks, respectively. The general trend of these scaling laws is that the aggregation number and core radius increase with the insoluble block length and decrease with the soluble block length; this is supported by both theory and experimental in a wide range of systems.[29] The actual values of the exponents in Equation 1.7 vary from system to system,

depending on the chemical nature of the blocks, the type of solvent, and the relative block lengths. Nevertheless, scaling laws of the type shown in Equation 1.7 generally show stronger positive N_B dependence than the negative N_A dependence.

One of the first theoretical treatments of block copolymer micelles was formulated by Noolandi and Hong,[33] who derived micellar characteristics by minimizing the Gibbs free energy of an isolated micelle. They calculated values of core radii, and aggregation numbers for micelles formed by the diblock copolymer polystyrene-*b*-polybutadiene (PS-*b*-PB) in heptane, a selective solvent for PB, using numerical values for the relevant Flory-Huggins interaction parameters χ_{AB}, χ_{AS}, χ_{BS} (where A and B are the two types of repeat units and S is the solvent), and the copolymer molecular weight and composition. Their predictions were in a good agreement (within 10%) of experimental results obtained previously by Plestil and Bladrian.[39] Following that, Whitmore and Noolandi[34] extended the Noolandi and Hong treatment of AB diblock copolymer micelles in selective solvents to blends of diblock copolymers of arbitrary composition in a homopolymer matrix. Here, the homopolymer was regarded as a high-molecular weight selective solvent; the determined exponents for the scaling of the core radius (Equation 1.7) were in the range of $0.67 \leq \kappa \leq 0.76$ and $0.1 \leq \gamma \leq 0$. According to the scaling relations, the authors pointed out that the dominant dependence of R_{core} is on the number of repeat units in the insoluble core-forming block (N_B) and that the effect of the soluble block length is relatively weak. Bluhm and Whitmore[35] refined the model of Noolandi and Hong[33] for PS-*b*-PB micelles in heptane and obtained $R_{core} \sim N_B^{0.67} N_A^{-0.01}$, again showing only a weak and negative soluble block length dependence.

Halperin[37] ,and independently Zhulina and Birshtein[40] studied a model where the

micelle has a small core and expanded shell, i.e. the star-like model (see Figure1.3), and obtained the following scaling laws:

$$R_{core} \sim N_B^{3/5} \qquad (1.8)$$

$$Z \sim N_B^{4/5}$$

The important point of this result is that the core radii and aggregation numbers of the micelles depend only on the length of the core-forming block, with no soluble block length dependence. Such behavior was attributed to the high curvature of the cores in star-like micelles, which enables the soluble blocks to occupy a larger interfacial area.[29] Therefore, the coronal chains in the star-like model remain relatively unperturbed by steric interactions with neighbouring chains, and contributions of the soluble block to a decrease in the conformational entropy of micelle growth become unimportant. It is worth mentioning that the scaling relations in Equation 1.8 are of particular relevance to the work described in this thesis, since the micelles described here have small core and expanded shell, and are therefore best described as star-like.

1.2.4. Block Ionomer Micelles

In general, ionic block copolymers or ion-containing block copolymers are materials that consist of nonionic hydrophobic blocks covalently linked to blocks containing a significant number of ionic moieties;[32,41-43] examples of ionic block copolymers include polystyrene-*b*-poly(metal acrylates), polystyrene-*b*-poly(metal methacrylates) and polystyrene-*b*-poly(4-vinylpyridinium alkyl halides). When such ionic

block copolymers self-assemble in organic solvents, which are selective for the hydrophobic block, the ionic moieties form an ion-containing core, surrounded by the soluble, nonionic corona. These type of micelles are termed block ionomer micelles, and their structure is similar to that of nonionic block copolymer micelles formed in selective organic solvents. However, the extreme incompatibility between the ionic and hydrophobic blocks results in a much stronger thermodynamic driving force for self-assembly than that of nonionic block copolymers, resulting in much lower CMCs than those of their nonionic counterparts.[41] In addition, block ionomer micelles show impressive kinetic stability over long periods of time, even at temperatures > 100 °C, which is attributed to the high T_g's of the glassy ionic cores. At room temperature, therefore, the chains are effectively locked into micelle on any reasonable time scale, i.e. the micelles are kinetically-frozen aggregates. We note that the block ionomer micelle system used to carry out the work described in this thesis, polystyrene-*b*-poly(cadmium acrylate) (PS-*b*-PACd), includes an additional factor contributing to the kinetic stability of the micelles, since divalent cadmium ions can serve as ionic cross-linkers for the core.

One of the first investigations of block ionomer micelles in solution dealt with the star-like polystyrene-*b*-poly(sodium methacrylate) (PS-*b*-PMANa) system with relatively short PMANa ionic blocks in solvents selectively good for the polystyrene blocks.[44] Using size-exclusion chromatography (SEC), it was observed that no micelle dissociation-association equilibrium was operative on the time scale of a few days, indicating that the micelles were extremely stable. As well, they used SEC coupled with viscometry to investigate the effect of varying the lengths of the polystyrene and ionic blocks on the aggregation numbers and hydrodynamic radii of the micelles. By this

method, the micellar molecular weights and aggregation numbers were determined from a universal calibration curve of log ($[\eta]M$) versus SEC elution volume, where $[\eta]$ is the intrinsic viscosity and M is the molecular weight of the eluting sample. Hydrodynamic radii were obtained using the following relationship:

$$[\eta]M = (10/3)Z\pi R_h^3 \qquad (1.9)$$

where Z is the micelle aggregation number and R_h is the hydrodynamic radius. They observed that both the aggregation numbers and hydrodynamic radii were found to increase as the number of ionic repeat units was increased for a given PS block length, in agreement with predicted scaling laws in Equation 1.8. Aggregation numbers were found to decrease when the length of the PS block increased, as expected, due to an increase in the solubility of the single chains; however, the hydrodynamic radius was found to increase. This was attributed to the increasing thickness of the corona for longer PS blocks, resulting in an overall increase in the micelle radius despite a decrease in the aggregation number. Subsequent studies on the same samples using dynamic light scattering (DLS) confirmed the results from size-exclusion chromatography.[45]

The first detailed study of scaling relations for PS-*b*-PAX block ionomer micelles with different metal ions (X = Ni^{2+}, Cs^{+}, Co^{2+}, Ba^{2+}, Cd^{2+}, Pb^{2+}) in the core was reported by Moffitt et al.[46] The scaling relations for the ionic core radius (R_{core}) as a function of the ionic block length (N_B) was determined: $R_{core} = K_R N_B^{0.58 \pm 0.03}$, where K_R is the proportionality constant and is dependent on the metal ion. The dependence of R_{core} on N_B, i.e. the scaling exponent, is in good agreement with theory for star-like block

copolymer micelles (Equation 1.8). This study is particularly relevant to use of block ionomers as nanoreactors of controlled size, as it determined scaling relations for micelle cores containing a wide variety of metal ions.

1.3. Semiconducting Nanoparticles (Quantum Dots)

Since the late 1980s, an enormous amount of research has been devoted to the synthesis and characterization of metal and semiconducting nanoparticles. Nanoparticles are generally categorized as the class of materials that fall between the molecular and bulk solid limits, with an average size between 1-10 nm.[47] Inorganic nanoparticles exhibit physical and chemical properties different from either the individual molecules or the bulk solids, hence attracting a lot of attention. The size-dependent properties of nanoparticles are determined mainly by two factors: 1) an increase in the surface-to-volume ratio compared to bulk materials and 2) changes in the electronic structure due to quantum confinement effects.[47,48] For example, while the melting point of bulk CdS is ~1600 °C, a typical 2.5 nm CdS nanocrystal melts at a temperature of ~ 400°C;[49] such a depression in the melting point is due to a higher surface energy of the nanoparticles compared to the bulk. Apart from such effects of large surface areas, semiconducting nanoparticles (QDs) undergo changes in their optical and electronic properties as a function of size; this is attributed to the quantum confinement effect, which is of particular relevance to the understanding of the optical properties of CdS nanoparticles, and so is addressed in the following section.

1.3.1. The Quantum Confinement Effect

In bulk semiconductors, the overlap of a large number of atomic orbitals leads to molecular orbitals that are closely spaced in energy and so form virtually continuous bands.[50] In effect, the molecular orbitals are delocalized over the entire crystal, and the movement of electrons in restricted only by the relatively small bandgap separating the valence and conduction bands. The energy of the first excited state, termed the exciton, is therefore virtually identical to the bandgap energy in the bulk; an exciton describes the electron-hole pair created when an electron leaves the valence band and enters the conduction band.

When the size of a semiconductor particle is smaller than or comparable to the size of the exciton in the macrocrystalline material, the delocalized bands become quantized, and the energy of the exciton increases.[47] Brus[51] has described this situation as a particle (the electron) in a spherical box (the nanoparticle), in which the movement of the electron is confined by an infinitely high potential at the surface. As a result, there is a confinement energy associated with the electron, and the exciton energy for semiconducting nanoparticles can be described by:

$$E^* \cong E_g + \frac{\hbar^2 \pi^2}{2R^2}\left[\frac{1}{m_c} + \frac{1}{m_h}\right] - \frac{1.8e^2}{\varepsilon R} + \ldots \qquad (1.10)$$

Where E^* is the energy of the exciton, E_g is the bandgap energy of the bulk semiconductor, R is the radius of the particle, m_e and m_h are the masses of electrons and holes in the lattice, e is the charge of an electron and ε is the permittivity. As can be seen from the equation above, the second term on the right hand side (the confinement term) is

inversely proportional to the square of the radius of the particle, and therefore becomes significant only when the particle size is sufficiently small. The third term on the right arises from Coulombic attraction between electrons and holes, and is a much smaller term than the confinement term. Therefore, Brus's particle-in-a-box model[51] predicts an increase in the energy of the exciton as the particle decreases in size. This quantum confinement effect is best observed from the absorption spectra of semiconducting nanoparticles of various average sizes. The absorption spectra of CdS nanoparticles of different mean sizes in aqueous solution are shown in Figure 1.5.[47] Particles larger than ~ 6 nm, larger than the size of an exciton (~ 5.8 nm) in the macrocrystalline material, start to absorb close to 515 nm (or 2.4 eV, corresponding to the bandgap of bulk CdS). With decreasing nanoparticle size, the absorption threshold shifts to shorter wavelengths, i.e. higher energy.

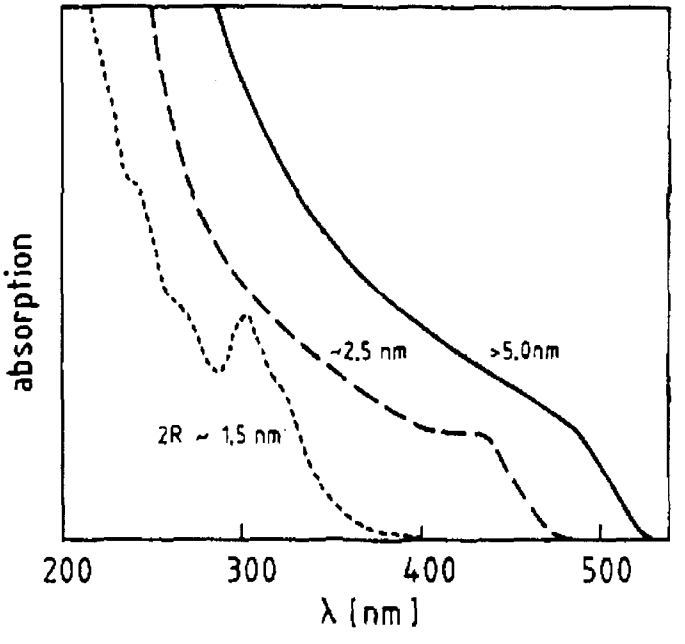

Figure 1.5. UV-vis absorption spectra of CdS nanoparticles of different mean particle sizes.[47]

1.4. Instrumentation: Imaging Techniques

Part of the work described in this thesis involves the use of atomic force microscopy (AFM), laser scanning confocal fluorescence microscopy (LSCFM), and transmission electron microscopy (TEM) as imaging techniques for characterizing the organization of QDs on various length scales in polymer environments. These three techniques are complementary to one other, since they probe structure at different depths in the polymer matrix (i.e. surface vs. bulk), and also on different length scales (i.e. nano vs. micro). A brief description of each of these imaging techniques is given below.

1.4.1. Atomic Force Microscopy (AFM)

Atomic force microscopy (AFM) is the most common technique used to image the surface topology of non-conductive samples. AFM can be divided into two primary scanning modes, contact and non-contact, which simply refers to whether or not the scanning probe actually comes into physical contact with the sample surface.[52] Since all of the AFM imaging in this thesis was carried out in contact mode, only contact mode AFM is described here. A schematic illustrating the AFM experiment is shown in Figure 1.6.

In contact mode AFM, the probe tip (which is mounted to the end of a cantilever) scans across the sample surface, coming into direct physical contact with the sample. As the probe tip scans, varying topographic features cause deflection of the tip and cantilever. A light beam from a small laser focused on the tip is bounced off the cantilever and reflected onto a four-section photodetector. The amount of deflection of the cantilever can then be calculated from the change in light intensity falling on the different sectors of

the photodetector. The resulting changes in the detector current signal is used in forming topographic images with both lateral and height information. The AFM instrument used for the imaging work described in this thesis is capable of a lateral resolution of ~ 10 nm and a vertical resolution of 1-2 nm.[52] However, the lateral resolution is highly dependent on the geometry of the AFM tip and also on the nature of the surface. In addition, in order to achieve optimum lateral and vertical resolution, substantial vibrational insulation, including both isolation tables and foam shielding to dampen air currents and sound waves is required.

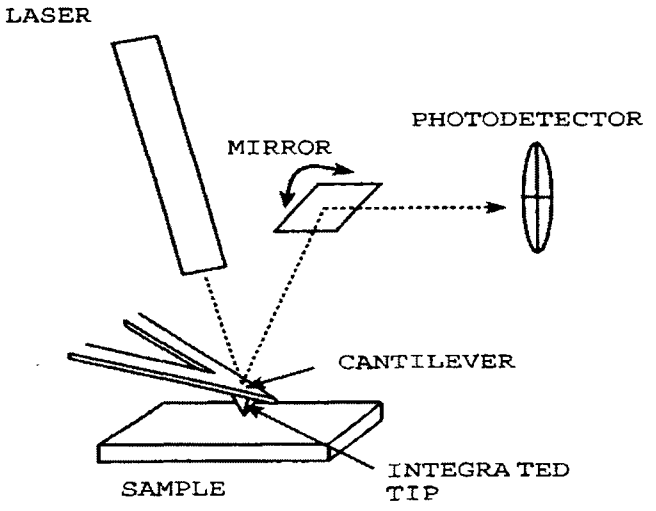

Figure 1.6. Schematic representation of atomic force microscopy (AFM).[52]

1.4.2. Laser Scanning Confocal Fluorescence Microscopy (LSCFM)

While the surface topology of materials can be probed by AFM, determination of bulk structure requires complementary techniques. Fortunately, the photoluminescent nature of QDs allows their spatial distribution within a polymer matrix to be imaged

using laser scanning confocal fluorescence microscopy (LSCFM), as long as the resulting features are on the micron scale. Therefore, in this section, the principles and advantages of LSCFM are discussed. Figure 1.7 shows a typical schematic of a LSCFM.

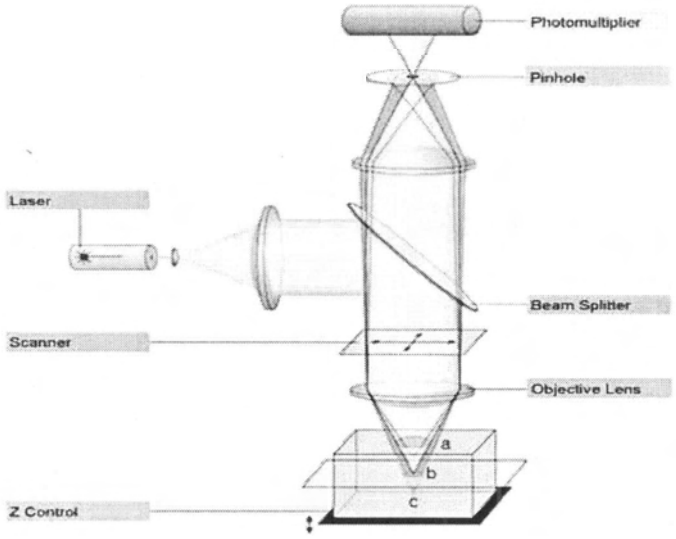

Figure 1.7. Schematic diagram of laser scanning confocal florescence microscopy (LSCFM).[53]

For LSCFM imaging, a laser is used to provide the excitation light. The laser beam passes through a beam-expanding lens and reflects off a dichroic mirror to the sample. A photoluminescent species (e.g. an organic dye or a QD) in the sample fluoresces and the emitted light is focused back through the objective lens and the dichroic mirror, then through the focusing lens and pinhole aperture to the photomultiplier detector. The complete image is collected by scanning through x and y directions and stored in the computer imaging system.

The main feature that distinguishes LSCFM from normal epifluorescence

microscopy is the presence of the adjustable pinhole in front of the photomultiplier detector; this special confocal pinhole only allows light from a thin focal plane to reach the detector at any given time. Therefore, by adjusting the focus in a stepwise fashion, optical sections at different depths can be obtained and compiled into a three-dimensional image. Such fast and *in situ* three-dimensional imaging, without the need for destructive and time-consuming physical sectioning of the sample makes LSCFM a powerful tool for 3D structural imaging.

LSCFM, like any optical microscopy technique, has a lateral spatial resolution that is governed by the diffraction limit of visible light. Additional limitations, such as refractive index mismatch between the sample and the surrounding medium, reduce the practical spatial resolution of LSCFM to feature sizes of just under 1 μm. Therefore, the direct imaging of individual QDs with sizes ~ 4 nm requires an alternative technique, such as transmission electron microscopy.

1.4.3. Transmission Electron Microscopy (TEM)

The idea that electrons can be used in microscopy imaging is attributed to De Broglie[54] (1924) who found that an accelerated electron beam has an effective wavelength of $\lambda \sim 0.005$ nm, shorter than visible light by a factor of 10^5. In principle, therefore, an electron microscope should be capable of imaging structures with atomic resolution, if one considers only the wavelength limitation. Figure 1.8 is a typical schematic of a transmission electron microscope (TEM).

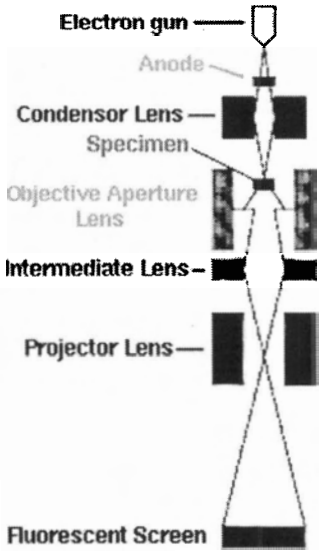

Figure 1.8. Schematic representation of transmission electron microscope (TEM).[54]

TEM forms an image by accelerating a beam of electrons that passes through the specimen. These electrons are scattered at different angles depending on the electron density they encounter in the sample.[54] When a beam of electrons pass through a specimen, electrons can either be (a) undeflected, (b) deflected without loss of energy (elastically scattered), or (c) deflected with significant loss of energy (inelastically scattered). The brightness of the image in each region will be proportional to the number of unscattered electrons which pass through the aperture, with light atoms, such as carbon, appearing bright while heavier atoms, such as iron, appear darker. The electron image is projected on a fluorescent screen where phases, fractures and other features down to ~ 2 Å can be resolved. The image is recorded by lifting the fluorescent screen, and allowing the electron image to fall directly onto a photographic plate or film.

1.5. Content of the Thesis

The remainder of this thesis consists of three chapters, each describing a distinct aspect of the characterization, patterning, and application of block copolymer-stabilized CdS QDs. The content of these three chapters is as follows:

Chapter 2 focuses on the characterization of the photoluminescence and structure of block copolymer-stabilized CdS QDs in dilute solutions. Specifically, the effect of different chemical treatments of the PAA layer at the QD surface on the static and time-resolved photoluminescence properties and solution structure of the CdS QDs is investigated. As well, the long-term stability of these polymer-stabilized CdS QDs and their dispersion in a polymer matrix is studied.

Chapter 3 describes a new and versatile method of patterning PS/QD nanocomposite features on glass substrates, via simple spin-casting of blend solutions of block copolymer-stabilized QDs with a poly(methyl methacrylate) (PMMA) homopolymer. The effects of spin-casting rotation speed and blend composition on the correlation length and morphology of the lateral PS/QD patterns is investigated. Selective removal of the PMMA phase of these films yields various nonlithographic hierarchical PS/QD features on glass substrates. AFM, LSCFM and TEM are employed in this study to image QD organization on various length scales.

Finally, Chapter 4 describes the application of block copolymer-stabilized CdS QDs as novel photoluminescent tracers for studying the morphology of PS/PMMA polymer blends. Specifically, the effects of PS/PMMA interfacial tension with varying PS molecular weight on the blend morphology is explored. As well, we investigate the

effect of the amount of added block copolymer-stabilized QDs on the observed morphologies to determine their viability as "passive" photoluminescent tracers.

1.6. References

(1) Weller, H. *Angew. Chem., Int. Ed. Engl.* **1993**, *32*, 41.

(2) Trindade, T.; O'Brien, P.; Pickett, N. L. *Chem. Mater.* **2001**, *13*, 3843.

(3) Murray, C. B.; Kagan, C. R.; Bawendi, M. G. *Annu. Rev. Mater. Sci.* **2000**, *30*, 545.

(4) Alivisatos, A. P. *J. Phys. Chem.* **1996**, *100*, 13226.

(5) Steigerwald, M. L.; Brus, L. E. *Acc. Chem. Res.* **1990**, *23*, 183.

(6) Henglein, A. *Chem. Rev.* **1989**, *89*, 1861.

(7) Kim, S.; Bawendi, M. G. *J. Am. Chem. Soc.* **2003**, *125*, 14652.

(8) Ni, T.; Nagesha, D. K.; Robles, J.; Materer, N. F.; Mussig, S.; Kotov, N. A. *J. Am. Chem. Soc.* **2002**, *124*, 3980.

(9) Murray, C. B.; Norris, D. J.; Bawendi, M. G. *J. Am. Chem. Soc.* **1993**, *115*, 8706.

(10) Herron, N.; Wang, Y.; Eckert, H. *J. Am. Chem. Soc.* **1990**, *112*, 1322.

(11) Dannhauser, T.; O'Neil, M.; Johansson, K.; Whitten, D.; McLendon, G. *J. Phys. Chem.* **1986**, *90*, 6074.

(12) Kolny, J.; Kornowski, A.; Weller, H. *Nano lett.* **2002**, *2*, 361.

(13) Lee, J.; Sundar, V. C.; Heine, J. R.; Bawendi, M. G.; Jensen, K. F. *Adv. Mater.* **2000**, *12*, 1102.

(14) Corbierre, M. K.; Cameron, N. S.; Sutton, M.; Mochrie, S. G. J.; Lurio, L. B.; Ruhm, A.; Lennox, R. B. *J. Am. Chem. Soc* **2001**, *123*, 10411.

(15) Spatz, J. P.; Herzog, T.; Moumer, S.; Ziemann, P.; Moller, M. *Adv. Mater.* **1999**, *11*, 149.

(16) Moffitt, M.; McMahon, L.; Pessel, V.; Eisenberg, A. *Chem. Mater.* **1995**, *7*, 1185.

(17) Nicholson, J. W. *The Chemistry of Polymers*, 2nd ed.; The Royal Society of Chemistry: Cambridge, 1997.

(18) Cowie, J. M. G., Ed. *Polymers: Chemistry & Physics of Modern Materials*, 2nd ed.; Chapman & Hall: New York, 1991.

(19) M. Szwarc; M. Levy; R. Milkovich. *J. Am. Chem. Soc.* **1956**, *78*, 2656.

(20) Riess, G. *Prog. Polym. Sci.* **2003**, *28*, 1107-1170.

(21) Szwarc, M. *Carbanions, Living Polymers and Electron Transfer Processes*; Interscience Publishers, Inc., 1968.

(22) Hautekeer, J.-P.; Varshney, S. K.; Fayt, R.; Jacobs, C.; Jerome, R.; Teyssie, P. *Macromolecules* **1990**, *23*, 3893.

(23) Zhong, X. F.; Varshney, S. K.; Eisenberg, A. *Macromolecules* **1992**, *25*, 7160.

(24) Gao, Z.; Zhong, X.-F.; Eisenberg, A. *Macromolecules* **1994**, *27*, 794.

(25) Sperling, L. H. *Introduction to physical polymer science*; John Wiley & Sons, Inc.: New York, 1992.

(26) Charles E. Carraher, J. *Seymour/Carraher's Polymer Chemistry*, 5th ed.; Marcel Dekker: New York, 2000.

(27) Wang, C.-W.; Moffitt, M. G. *Langmuir* **2004**, *20*, 11784.

(28) Zhang, L.; Eisenberg, A. *J. Am. Chem. Soc.* **1996**, *118*, 3168.

(29) Tuzar, Z.; Kratochvil, P. In *In Surface and Colloid Science*; Matijevic, E., Ed.; Plenum Press: New York, 1993; Vol. 15, pp 1-83.

(30) Cameron, N. S.; Corbierre, M. K.; Eisenberg, A. *Can. J. Chem.* **1999**, *77*, 1311.

(31) Hadjichristidi, N.; Pispas, S.; Floudas, G. *Block Copolymers*; John Wiley & Sons, Inc: New Jersey, 2003.

(32) Hamley, I. W. *The Physics of Block Copolymers*; Oxford University Press, Inc.: New York, 1998.

(33) Noolandi, J.; Hong, K. M. *Macromolecules* **1983**, *16*, 1443.

(34) Whitmore, M. D.; Noolandi, J. *Macromolecules* **1985**, *18*, 657.

(35) Bluhm, T. L.; Whitmore, M. D. *Can. J. Chem.* **1985**, *63*, 249.

(36) Nagarajan, R.; Ganesh, K. *J. Chem. Phys.* **1989**, *90*, 5843.

(37) Halperin, A. *Macromolecules* **1987**, *20*, 2943.

(38) Leibler, L.; Orland, H.; Wheeler, J. C. *J. Chem. Phys.* **1983**, *79*, 3550.

(39) Plestil, J.; Bladrian, J. *Makromol. Chem.* **1975**, *176*, 1009.

(40) Zhulina, E. B.; Birshtein, T. M. *Vysokomol Soedin.* **1985**, *27*, 511.

(41) Webber, S. E.; Munk, P.; Tuzar, Z., Eds. *Solvents and Self-Organization of Polymers*; Kluwer Academic Publisers: Boston, 1996.

(42) Alexandridis, P.; Lindman, B., Eds. *Amphiphilic Block Copolymers*; Elsevier: New York, 2004.

(43) Loh, W. In *Encyclopedia of Colloid and Surface Science*; Hubbard, A., Ed.; Marcel Dekker, 2002; pp 802-813.

(44) Desjardins, A.; Eisenberg, A. *Macromolecules* **1991**, *24*, 5779.

(45) Desjardins, A.; van de ven, T. G. M.; Eisenberg, A. *Macromolecules* **1992**, *25*, 2412.

(46) Moffitt, M.; Eisenberg, A. *Macromolecules* **1997**, *30*, 4363.

(47) Henglein, A. *Chem. Rev.* **1989**, *89*, 1861.

(48) Sapra, S.; Nanda, J.; Sarma, D. D. In *Proc. of the Plenary 90th Session of Indian Science Congress*: Bangalore, 2003; pp 3.4-3.30.

(49) Goldstein, A. N.; Echer, C. M.; Alivisatos, A. P. *Science* **1992**, *256*, 1425.

(50) Shriver, D.; Atkins, P. *Inorganic Chemistry*, 3 ed.; Oxford University Press: New York, 1999.

(51) Brus, L. *J. Phys. Chem.* **1986**, *90*, 2555.

(52) Marek, T. *Explorer^{TM} Instrument Operation Manual*; ThermoMicroscopes Corporation: CA, 2001.

(53) Chen, M. L.; THE NEWSLETTER OF THE UIC RESEARCH RESOURCES CENTER, 2001.

(54) Agar, A. W.; Alderson, R. H.; Chescoe, D. *Principles and Practice of Electron Microscope Operation*; American Elsevier Publishing Company, Inc.: New York, 1974.

CHAPTER 2

SURFACE-TUNABLE PHOTOLUMINESCENCE FROM BLOCK COPOLYMER-STABILIZED CADMIUM SULFIDE QUANTUM DOTS

2.1. Introduction

For future applications of colloidal QDs in thin films and three-dimensional device structures, their facile incorporation into various polymer environments will be of critical importance. Conventional synthetic methodologies for colloidal CdSe and CdS produce tri-*n*-octylphosphine oxide (TOPO)-stabilized nanoparticles that tend to undergo aggregation in common polymers such as polystyrene and poly(methylmethacrylate), resulting in a loss of optical clarity and quenching of photoluminescence.[1,2]Among the various strategies for obtaining nanocomposites of well-dispersed semiconducting QDs in a polymer matrix,[2-6] several recent studies have targeted the production of discrete colloidal building blocks with a polymeric layer coating the inorganic nanoparticle.[7-13] This "building block" concept offers an exciting degree of versatility for producing nanocomposite structures, since an appropriate polymer layer can solubilize hybrid nanoparticles in a matrix of the equivalent homopolymer,[14] or mediate the self-assembly of colloidal QDs via steric repulsions between approaching polymer brushes, resulting in ordered nanocomposites.[15]

Following earlier work by Murphy and coworkers,[16,17] Lemon et al. reported the synthesis of CdS nanoparticles in a poly(amidoamine) dendrimer nanoreactor, resulting in discrete dendrimer-coated fluorescent nanoparticles.[7] A ligand-exchange approach was used by Guo et al. to encapsulate pre-formed CdSe/CdS core-shell nanoparticles in cross-linked dendron "boxes".[8] Poly(caprolactone)-coated CdS nanoparticles have been synthesized by Carrot et al. via covalent surface attachment of thiol-functional polymer chains.[9] Other studies by Emrick and coworkers have effectively demonstrated the surface functionalization of TOPO-covered CdSe QDs with polystyrene, polyolefin, and

poly(ethylene glycol), using ligand-exchange and surface polymerization strategies.[10-12] Recently, Potapova et al. have applied electrostatic binding of poly(acrylamide) ionomers to negatively charged CdSe/ZnS colloidal QDs to the production of hybrid polymer-inorganic nanoparticles.[13]

An alternative and relatively direct route to polymer-coated semiconductor colloids utilizes templates of microphase-separated block copolymers.[15,18-30] This approach has been applied in a number of studies in which amphiphilic block copolymers undergo self-assembly to form nanoscale domains of metal ion-containing or metal ion-complexing blocks in the solid-state,[18,19,23] or block copolymer micelles in organic solvents with insoluble cores of the metal ion-containing blocks.[15,20-22,24-30] The metal ions are then chemically transformed via simple reduction or precipitation reactions into metal or semiconducting nanoparticles. Under certain conditions, single nanoparticles can be grown inside each spherical core or microdomain, providing the advantage of thermodynamic nanoparticle size control via the aggregation number or the degree of metal ion loading.[20-22] In some cases, the block copolymer template can play the role of a stabilizer following nanoparticle synthesis, yielding colloidal inorganic nanoparticles coated by two covalently-linked polymer layers: an inner layer of insoluble blocks, and an outer "brush" layer of soluble blocks.

Moffitt et al. demonstrated that single CdS QDs can be synthesized in the ionic cores of polystyrene-*b*-poly(cadmium acrylate) (PS-*b*-PACd) micelle.[20] Using polystyrene-*b*-poly(acrylic acid) (PS-*b*-PAA) block copolymers with long PS and short PAA blocks, block ionomer micelles were formed upon neutralization of the PAA blocks with cadmium acetate in organic solvents; each poly(cadmium acrylate) core then served

as a template for the synthesis of a single quantum dot by exposing the block ionomer to H_2S in the solid state (Scheme 2.1). Size control of CdS QDs was achieved by tuning the aggregation number of the block ionomer host via the length of the PAA block. The resulting block copolymer micelles could then be dispersed in organic solvents to obtain stable and optically clear colloids consisting of QDs stabilized by polystyrene-*b*-poly(acrylic acid) (PS-*b*-PAA) (Scheme 2.2).[20] The stability of the micelles to repeated precipitation into methanol was found to increase with re-neutralization of the PAA layer with NaOH or cadmium acetate dihydrate. However, the photoluminescence (PL) properties and solution structure of the polymer-coated QDs were not explored, nor was the incorporation of these building blocks into polymer films.

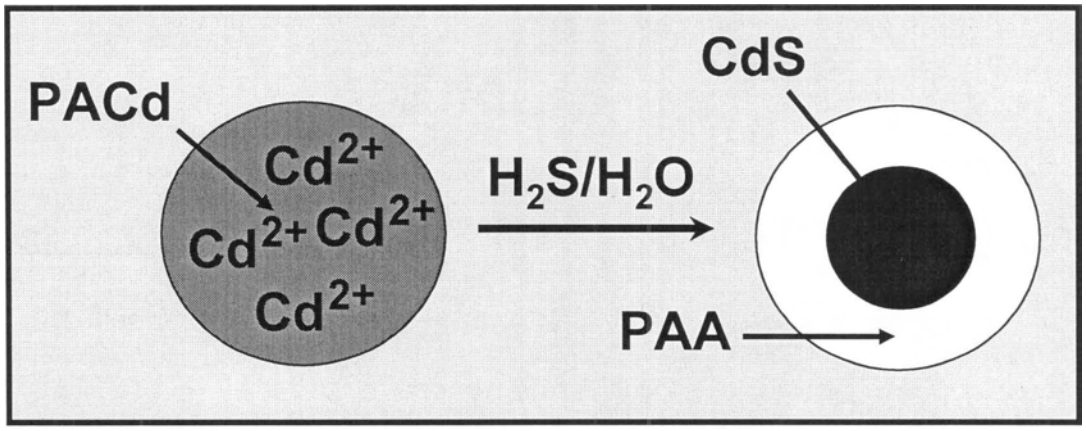

Scheme 2.1. Chemical conversion of Cd^{2+} ions into CdS QDs in a block ionomer nanoreactor.[31]

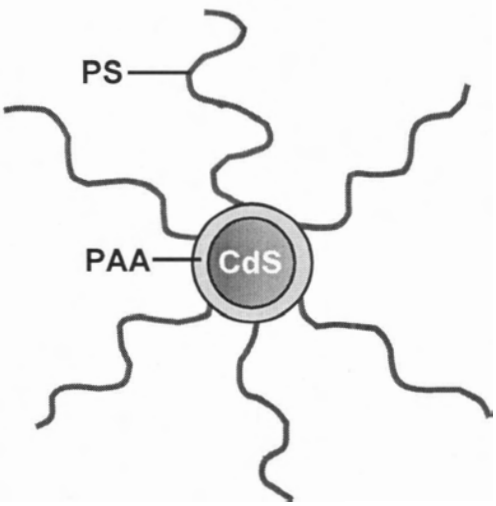

Scheme 2.2. CdS QDs stabilized by polystyrene-*b*-poly(acrylic acid) (PS-*b*-PAA) in organic solvent (e.g. tetrahydrofuran, toluene).

One intriguing aspect of these PS-*b*-PAA-stabilized colloidal QDs is the chemical reactivity of the carboxylic acid groups in the PAA layer surrounding the nanoparticle surface. It has been shown that reloading the carboxylic acid groups with metal ions and subsequent chemistry can be used to increase the nanoparticle size or, in principle, to obtain inorganic core-shell particles.[20,23] Here, we demonstrate that simple chemistry within the PAA layer can be used to tune the PL of the QDs, allowing for optimization of quantum yields as well as light emission that can be "switched" as a function of the chemical form of PAA. The observed tunable PL is attributed to changes in the surface environment of the CdS nanoparticles, which result in variations in the density and nature of surface trap states.[1,32-49] Spanhel et al.[37] showed that the addition of Cd^{2+} ions at high pH dramatically enhances the quantum yields of colloidal CdS QDs; this type of surface activation has been applied primarily to QDs dispersed in aqueous media,[37,40,44-48]

although it has also been demonstrated in QDs stabilized by surfactants or organic ligands in hydrophobic solvents.[38,39,49,50] To our knowledge, the present work demonstrates the first example of Cd^{2+} surface activation in QDs decorated by a hydrophobic polymer brush, providing new opportunities for polymeric sensors and devices. With appropriate treatment of the PAA layer, the PL of these PS-*b*-PAA-stabilized QDs is found to be remarkably stable over periods of several months. We also show that these polymer-coated quantum dots can be well-dispersed in polystyrene homopolymer by simple solution blending, yielding optically clear nanocomposites which retain the PL of the original colloidal building blocks.

2.2. Experimental

2.2.1. Synthesis of Polystyrene-b-Poly(acrylic acid) (PS-b-PAA) Diblock Copolymer

The polystyrene-*b*-poly(*tert*-butylacrylate) diblock copolymer (PS-*b*-P*t*BA) used in the present study was synthesized using well-established anionic polymerization techniques, as described in Chapter 1.[51,52] Therefore, only a brief summary will be presented here. All monomers were stirred over calcium hydride for 24 h, distilled under vacuum, and stored under nitrogen at -20 °C. Before the polymerization reaction, styrene and *tert*-butylacrylate monomers (Aldrich) were further purified by the addition of fluorenyllithium or triethylaluminum, respectively, followed by an additional vacuum distillation step. The tetrahydrofuran (THF) reaction solvent was freshly distilled following reflux over sodium/benzophenone. Solvents, monomers, and initiator were transferred using flamed stainless steel canulas and syringe needles. 10-20 drops of

α-methylstyrene (Aldrich) were added to a previously-flamed reaction flask containing LiCl (10 mol LiCl : 1 mol *sec*-butyllithium) dissolved in ca. 450 mL THF under ultra-high purity nitrogen atmosphere. The reaction mixture was then titrated with *sec*-butyllithium initiator (1.3M in hexanes, Aldrich) until a dark red color persisted, followed by the addition of the desired quantity of initiator. The reaction flask was cooled to -78 ^{o}C using a dry ice/acetone bath, followed by the addition of styrene monomer. Once the polymerization of styrene was complete, an aliquot of the reaction mixture was withdrawn for analysis of the degree of polymerization of the polystyrene block by size-exclusion chromatography (SEC). The *tert*-butylacrylate monomer was then added to the reaction medium for the polymerization of the second block, after which the polymerization reaction was terminated by the addition of degassed methanol. The *tert*-butylacrylate content of the recovered copolymer was determined using quantitative FTIR spectroscopy of the carbonyl C=O stretching mode from PtBA (1730 cm^{-1}) in CCl_4 solution, as previously described.[52]

The block copolymer in the ester form was hydrolyzed to polystyrene-*b*-poly(acrylic acid) (PS-*b*-PAA) by overnight reflux in toluene with *p*-toluenesulfonic acid as the catalyst (5 mol % relative to the *tert*-butylacrylate content) to obtain the block copolymer PS(330)-*b*-PAA(20); the numbers in parentheses indicate degrees of polymerization for each block calculated from number average molecular weights. FTIR confirmed complete hydrolysis; the sharp C=O ester mode at 1730 cm^{-1} was replaced by a broad acid doublet, which disappeared when the sample was treated with NaOH. The polydispersity of the diblock (PI = 1.02) was determined from SEC of the copolymer in the ester form.

2.2.2. Preparation of Polystyrene-b-Poly(cadmium acrylate) (PS-b-PACd) Micelles (MIC-Cd)

The block copolymer PS(330)-*b*-PAA(20) was dissolved in benzene/methanol (90/10 v/v) at a concentration of ca. 2 wt %. The formation of reverse micelles with insoluble PACd cores and soluble PS coronae was induced by the addition of excess 0.25 M cadmium acetate dihydrate (Aldrich) in methanol (1.5 mol cadmium acetate dihydrate : 1 mol acrylic acid repeat units), followed by stirring the solution for 4 h. The material was recovered by freeze-drying then dried in a vacuum oven at 70 °C for 24 h. Excess cadmium acetate was removed by washing the freeze-dried micelles repeatedly with methanol followed by drying the white powder under vacuum at 70 °C for 24 h.

SEC of the resulting PS-*b*-PACd block ionomer in THF (not shown) revealed two fractions: a high molecular weight fraction (ca. 70 wt %) attributed to micelles and a low molecular weight fraction (ca. 30 wt %) attributed to PS homopolymer resulting from chain termination during anionic polymerization. A fractionation procedure was carried out to remove the PS homopolymer impurity: the sample was dissolved in THF (5 wt %) and stirred at a medium rate while adding deionized water dropwise, until a cloudy precipitate persisted that did not redissolve with further stirring. Water addition was stopped before complete precipitation of the sample from THF occurred. The cloudy solution was allowed to settle overnight into two layers. The clear top layer was then separated from the cloudy bottom layer, which was analyzed by SEC to assess the remaining homopolymer content. This procedure was repeated several times until amount of homopolymer in the bottom layer was < 2 wt %. The purified micelle sample was then recovered by precipitation into methanol and dried under vacuum at 70 °C for 24 h.

2.2.3. Preparation of PS-b-PAA-Stabilized CdS Quantum Dots (MIC-CdS) and Subsequent Surface Chemistry

Following fractionation, the white powder consisting of PS(330)-*b*-PACd(20) block ionomer micelles was exposed to an atmosphere of 100 % humidity for a period of 1 week. The ionomer powder was subsequently exposed to H_2S (bubbled through H_2O at room temperature). After about 45 min, the white powder turned a light yellow colour, which intensified with further exposure to H_2S. After 9 h exposure time, the yellow powder was stored under active vacuum for 12 h to remove excess H_2S. The resulting sample of PS-*b*-PAA-stabilized CdS quantum dots was designated MIC-CdS1.

Various steps of subsequent chemistry in the PAA layer of MIC-CdS1 were carried out to prepare the samples MIC-CdS2, MIC-CdS3 and MIC-CdS4. First, MIC-CdS1 was dispersed in THF (2 wt %) and excess cadmium acetate dihydrate in methanol (2 mol cadmium acetate dihydrate : 1 mol acrylic acid repeat units) was added with overnight stirring. A yellow powder was recovered by precipitation into methanol, then washed repeatedly with methanol to remove excess cadmium acetate and dried in a vacuum oven at 70 °C for 24 h. This re-neutralized sample was designated MIC-CdS2. Second, the yellow powder MIC-CdS2 was exposed to "wet" H_2S (bubbled through H_2O) for 8 h to produce the protonated sample MIC-CdS3. Finally, the PAA layer of MIC-CdS3 was re-neutralized with cadmium acetate dihydrate in THF solution and recovered as a yellow powder (MIC-CdS4) as described above for the re-neutralization of MIC-CdS1.

The samples MIC-CdS1 and MIC-CdS2 were also treated by titrating with NaOH and cadmium acetate, following aging of each sample dispersed in toluene. For these

experiments, colloids of MIC-CdS1 and MIC-CdS2 dispersed in spectroscopic toluene were first aged for various periods by storing the solutions in a dark cupboard under ambient conditions and monitoring the PL and quantum yields at various times as described in the text. After a given period of aging, the solutions were treated with excess NaOH in methanol (4 NaOH : 1 acrylic acid repeat unit) and then treated with successively increasing quantities of cadmium acetate dihydrate in methanol until the PL intensity reached a maximum value.

In addition to the samples MIC-CdS1 – MIC-CdS4, an additional QD sample was prepared in a manner identical to that described for MIC-CdS1, but using a different block copolymer, PS(140)-b-PAA(17) (Polymer Source, Montreal). This sample was designated MIC-CdS5, and was used for titration experiments comparing the effects of adding cadmium acetate and magnesium acetate on PL intensity in the band-edge region.

2.2.4. Preparation of QD Blend Films

Blends of MIC-CdS4 and PS homopolymer were prepared by dissolving appropriate quantities of each component in spectroscopic grade toluene to a total polymer concentration of 4 wt % Two PS homopolymer samples were prepared by anionic polymerization for these blending experiments: PS(1250), PI = 1.01 and PS(100), *PI* = 1.04, where the numbers in parentheses indicate degrees of polymerization. Blend solutions were stirred for ~2 h and left to stand overnight in the dark to equilibrate. Solutions were then deposited on 18x18 mm glass cover slides, placed in Petri dishes covered with aluminum foil, and left in a fumehood to evaporate for 1 week. The

resulting CdS QD blend films were then dried overnight in a vacuum oven at 70 °C to remove residual solvent.

2.2.5. Size-Exclusion Chromatography (SEC)

All SEC measurements were performed using a Viscotek Model 302 liquid chromatography system equipped with refractive index (RI), low-angle light scattering (LALS, $\theta = 7°$) , right-angle light scattering (RALS, $\theta = 90°$), and UV detectors. THF was used as the eluent at a flow rate of 1 mL/min and the column temperature was set at 35 °C. All polymer solutions were filtered through membrane filters with a nominal pore size of 0.45 μm before injection into the SEC column. The data were collected and analyzed on a Del Dimension 2300 computer with appropriate SEC software from Viscotek. Two ViscoGEL HR High Resolution Columns (styrene-divinyl benzene columns) in series were used: G3000 HR 60 k GMHHR-M Mixed Bed 4 M columns.

Molecular weights for PS homopolymer and micelle samples were calculated from SEC data using an algorithm from Viscotek, which relies on low-angle light scattering detection from a 670 nm diode laser source. This utilizes the fundamental Zimm equation for light scattering from polymer solutions:

$$\frac{KC}{R_\theta} = \frac{1}{M_w P(\theta)} + 2A_2 C \qquad (2.1)$$

where R_θ is the excess Rayleigh scattering ratio, $P(\theta)$ is the particle scattering factor, M_w is the weight-average molecular weight of the sample, A_2 is the second virial coefficient, C is the polymer concentration and K is a composite of optical and fundamental constants.

The excess Rayleigh ratio is the ratio of light scattered from the solution in excess of solvent scattering at an angle of detection θ, I_θ, with respect to the incident beam intensity, I_0: $R_\theta = kI_\theta/I_0$, where k is an instrumental constant. In the typical Zimm plot approach, M_w is analyzed by detecting scattered light for each concentration at a series of angles, followed by extrapolation to $\theta = 0$, where the scattering factor $P(\theta) = 1$. By contrast, the present Viscotek LALS monitors light scattered at a single low-angle as the sample is eluted; irrespective of particle shape, $P(\theta)$ is very close to 1 for an angle of detection of $\theta = 7°$, so that M_w can be calculated without multi-angle extrapolation. For the CdS-containing samples, A_2 was estimated from multiple injections of the sample MIC-CdS4 at different concentrations.

2.2.6. Absorption and Photoluminescence Measurements

Absorption spectra were recorded on a Cary 50-scan UV-vis spectrophotometer. Static fluorescence measurements were recorded on an Edinburgh Instruments FLS 920 instrument equipped with a Xe 450W arc lamp and a red sensitive PMT (R928-P). For typical measurements of optical properties, the MIC-CdS samples were dispersed in spectroscopic grade toluene at concentrations such that the measured absorbance at 400 nm was less than 0.1.

PL quantum yields (Φ) of the MIC-CdS colloids in toluene were determined using perylene (Aldrich) in deoxygenated absolute ethanol as a reference, which has a fluorescence quantum yield close to 1.0.[40,53] The following equation was applied:

$$\Phi_s = (A_r/A_s)(n_s^2/n_r^2)(D_s/D_r) \qquad (2.2)$$

where A_r and A_s are the absorbance values of the perylene solution and MIC-CdS colloids at 400 nm, respectively, n_s and n_r are the refractive index values of the sample and reference solvents, and D_s and D_r are the corrected integrated PL intensities for 400 nm excitation. Before calculating integrated PL intensities, a solvent background was subtracted and a correction for the detector response was applied to each sample and reference measurement. However, for simplicity, only the technical spectra are presented in the figure and all spectra were record at 1nm spectra resolution.

PL lifetime measurements were performed using an Edinburgh Instruments nF900 nanosecond flashlamp with pulse width 1.0-1.6 ns. All decay profiles were collected until a maximum intensity of 1000 photon counts had been reached. Decay profiles were fitted over two decades of intensity starting at channels after the flashlamp pulse, using a tail-fit algorithm. For band-edge emission, two separate measurements of decay profiles were obtained to determine the error on average lifetimes, and reported fit parameters are averages of the two fits. From repeat measurements, the errors on reported average band-edge lifetimes were between 2 and 10 %. For trap emission, the average lifetimes were determined from a single decay profile.

2.2.7. Laser Scanning Confocal Fluorescence Microscopy (LSCFM)

Laser scanning confocal fluorescence microscopy measurements of CdS QD blend films were done on a Zeiss LSM 410 equipped with an Ar/Kr laser. All films were excited at ~488 nm, using a bandpass 485 ± 20 nm line selection filter and a FT 510 dichroic beam splitter. A longpass 515 emission filter was used such that only light

above 515 nm reached the PMT. A pinhole diameter 0.984 Airy Units was used for all measurements, resulting in an optical section thickness of 0.615 μm FWHM.

2.2.8. Transmission Electron Microscopy (TEM)

Transmission electron microscopy was performed on a Hitachi H-700 electron microscope, operating at an accelerating voltage of 70 kV. CdS QD blend films were first embedded in an Epon resin, and then 30-60 nm thick sections were produced with a diamond knife on Reichert UltraCut E ultra-microtone. The thin sections were then placed on carbon/formvar-coated 300 mesh copper grids for imaging.

2.2.9. Dynamic Light Scattering (DLS)

Dynamic light scattering (DLS) experiments were carried out on a Brookhaven Instruments photon correlation spectrometer equipped with a BI-200SM goniometer, a BI-9000AT digital autocorrelator, and a Melles Griot He-Ne Laser (632.8 nm) with maximum power output of 75 mW. To ensure the accuracy of DLS measurements, great care was taken to eliminate dust from the samples. Spectroscopic grade toluene was filtered through two membrane filters with 0.20 μm nominal pore size connected in series, and stock solutions of MIC-CdS colloids dispersed in toluene with concentrations of ca. 5 mg/mL were filtered through two membrane filters with 0.45 μm nominal pore size connected in series. All scintillation vials were thoroughly cleaned with filtered toluene, and stock solutions of the MIC-CdS colloids were filtered into the dust-free scintillation vials. Successive dilutions of the colloids were carried out by adding known quantities of filtered toluene. DLS measurements were conducted at 5 different angles: 35°, 50°, 70°,

90° and 120°, and at five different concentrations in the range of 0.05-0.01 mg/mL. For each angle and concentration, three repeat measurements of the autocorrelation function were obtained. All DLS measurements were conducted at 23 °C.

2.2.10. Static Light Scattering

Static light scattering (SLS) experiments were carried out on a Brookhaven Instruments multi-angle system equipped with a BI-200SM goniometer, a BI-9000AT digital autocorrelator, and a Melles Griot He-Ne Laser (632.8 nm) with maximum power output of 75 mW. To ensure the accuracy of SLS measurements, great care was taken to eliminate dust from the samples. Spectroscopic grade THF was filtered through two membrane filters with 0.20 μm nominal pore size connected in series, and stock solutions of MIC-CdS4 colloid dispersed in THF was filtered through two membrane filters with 0.45 μm nominal pore size connected in series. All scintillation vials were thoroughly cleaned with filtered THF, and stock solutions of the MIC-CdS4 were filtered into the dust-free scintillation vials. Successive dilutions of the colloids were carried out by adding known quantities of filtered toluene.

The stock solutions of MIC-CdS4 with concentrations of ca. 10 mg/mL were prepared the night before SLS measurements to ensure equilibration. SLS measurements were carried out in a concentration range from 1-0.2 mg/mL and the angles of detection ranged from 15-155° with 5 degree increments between measurements. 10 repeat measurements of scattered light intensity were taken at each angle and concentration. The reported aggregation number and radius of gyration were determined from the average results of two separate Zimm plots obtained from different stock solutions. All SLS measurements were conducted at 23 °C.

2.3. Results and Discussion

2.3.1. Absorption and FTIR Spectra of PS-b-PAA-Stabilized CdS QDs: Effect of Surface Chemistry

H_2S treatment of the freeze-dried PS(330)-*b*-PACd(20) micelles (MIC-Cd) yielded a yellow powder (MIC-CdS1) that could be easily dispersed in various organic solvents (e.g. toluene, chloroform, THF) to obtain clear yellow solutions. The structured absorption spectrum of MIC-CdS1 in toluene (Figure 2.1) allows optical transitions at 428 nm and 378 nm to be distinguished, indicating low-polydispersity quantum-confined CdS. From the position of the absorption edge (474 nm), a CdS nanoparticle diameter of 4.4 nm is calculated, using Henglein's empirical curve relating the absorption threshold and CdS QD size.[33]

Previous work on CdS QD synthesis in block ionomers suggested the formation of a single QD in each block ionomer microdomain, pointing to a mechanism of nanoparticle size control via the aggregation number of the original block ionomer template.[20] In the present case, we determined the micelle aggregation number of MIC-Cd dispersed in THF to be ~100, using SEC with LALS detection. Considering that each PAA block contains 20 units of acrylic acid, the number of Cd^{2+} ions in the micelle core is therefore ~1000, assuming bridged Cd^{2+} counterions following neutralization with cadmium acetate. We point out that actual aggregation numbers following freeze-drying from benzene/methanol may be somewhat different from values determined in THF, dueto differences in solvent polarity, although based on earlier small-angle x-ray scattering results[54] this effect is not expected to be large. Assuming the bulk CdS density

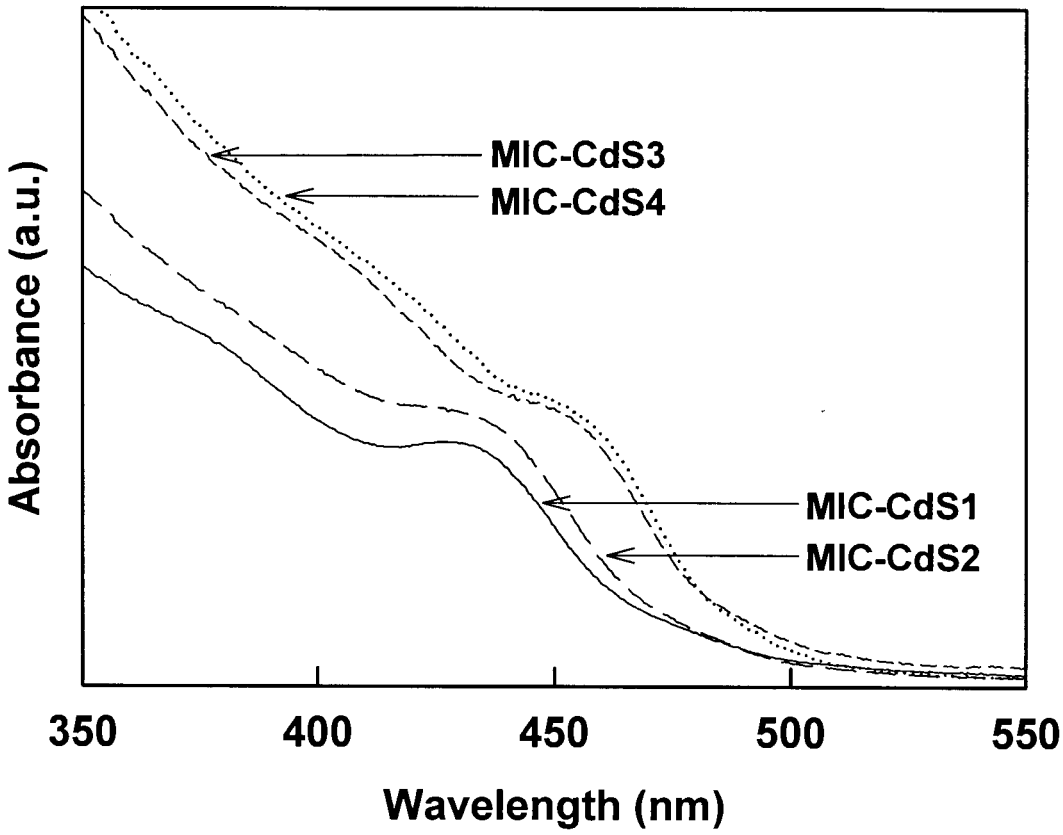

Figure 2.1. Absorption spectra of PS-*b*-PAA-stabilized CdS QDs in toluene with various treatments of the PAA layer.

value (d = 4.82 g/mL), the number of Cd^{2+} ions in each 4.4 nm-nanoparticle of MIC-CdS1 is ~ 900, in good agreement the original number of Cd^{2+} ions in the ionomer template; this indicates that a single CdS QD is formed in each micelle core. The proposed structure for the MIC-CdS1 particles is shown in Scheme 2.2, indicating a single CdS QD coated by a layer of PS-*b*-PAA chains. The PS blocks provide solubility in organic solvents and the reactive PAA layer at the polymer-inorganic interface provides a route to further chemistry at the QD surface.

The PAA interface layer of MIC-CdS1 was subsequently treated with successive re-neuralization/re-protonation steps to yield MIC-CdS2 - MIC-CdS4 as shown in Figure 2.2A. All four samples were isolated as bright yellow powders that could be dispersed in various organic solvents to yield optically clear yellow solutions. Following each step of chemical treatment at the QD surface (Figure 2.2A), an FTIR spectrum was obtained to characterize the PAA layer (Figure 2.2B). For MIC-CdS1, the C=O stretching vibration results in a broad band at 1710 cm^{-1} with a shoulder at ~1738 cm^{-1}. This doublet absorption band is characteristic of carboxylic acid groups, and confirms that H_2S treatment of the original block ionomer template resulted in re-protonation the PAA blocks, forming COOH groups in the interface layer of MIC-CdS1. Treatment of MIC-CdS1 by stirring in THF with an excess of cadmium acetate, followed by washing to remove residual cadmium acetate, results in a disappearance of the C=O carboxylic acid doublet and appearance of a band at ~1550 cm^{-1}, attributed to asymmetric stretch of COO^- in PACd; this suggests that the carboxylate groups in the interface layer are neutralized with Cd^{2+} counterions in MIC-CdS2. Subsequent treatment of MIC-CdS2 with H_2S results in a return of the carboxylic acid doublet, and nearly complete

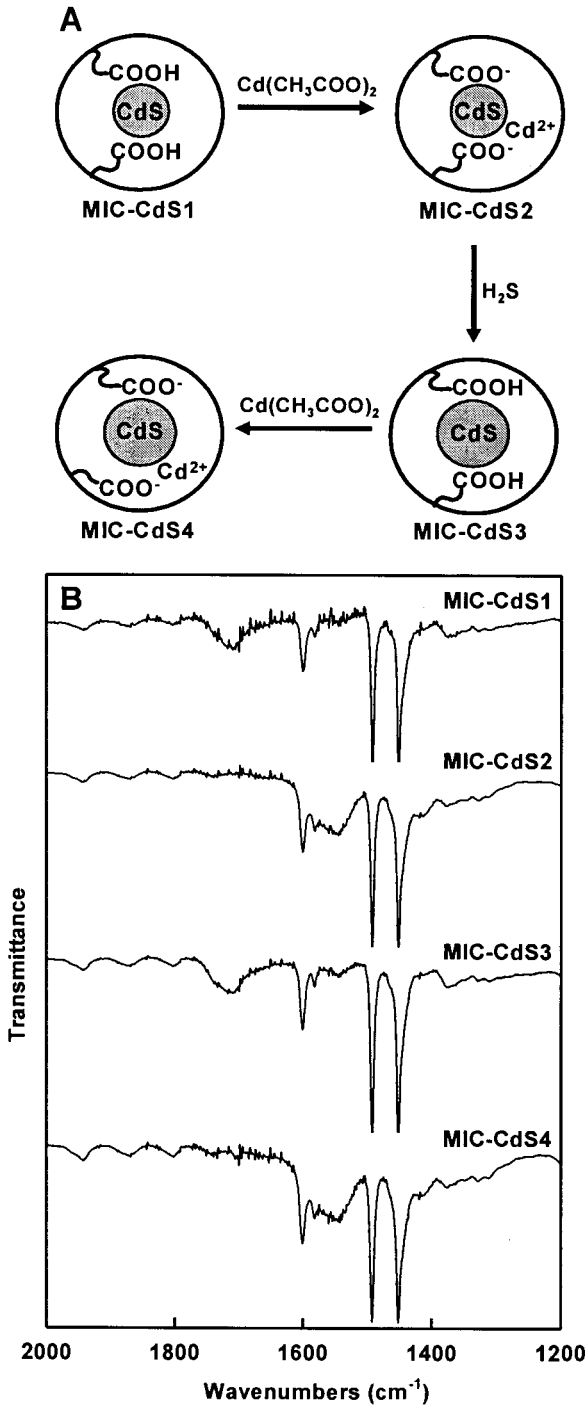

Figure 2.2. Schematic demonstrating various treatments of PS-*b*-PAA-stabilized CdS QDs, and effect on QD size and PAA layer (A), and FTIR spectra of the resulting four samples (B).

disappearance of the 1550 cm^{-1} band, indicating re-protonation of the PAA layer in MIC-CdS3. Finally, another treatment with excess cadmium acetate re-neutralizes the acid layer at the QD surface, as shown by a return of the 1550 cm^{-1} band and nearly complete disappearance of the acid doublet in MIC-CdS4.

Comparison of absorption spectra of MIC-CdS1 - MIC-CdS4 in toluene reveals the effect of chemical treatment of the PAA interfacial layer on the QD size (Figure 2.1). The CdS spectrum of MIC-CdS2 shows a marginal red-shift relative to MIC-CdS1, indicating a slight increase in QD diameter from 4.4 nm to 4.7 nm, which is attributed to ripening during cadmium acetate treatment in THF solution. A more marked change in the absorption spectrum is observed for MIC-CdS3 following H_2S treatment of MIC-CdS2, with a redshift in the absorption edge to 492 nm, corresponding to an increase in the CdS nanoparticle size to 5.4 nm. This size increase is explained by secondary growth of the QDs by deposition of CdS on the surface of the original nanoparticles. Subsequent re-neutralization of the PAA layer does not result in a significant change in the QD size, as indicated by the nearly overlapping absorption spectra of MIC-CdS3 and MIC-CdS4.

2.3.2. Surface-Tunable Photoluminescence of PS-b-PAA-Stabilized CdS QDs

Along with the well-established effects of quantum confinement, the PL of semiconducting QDs is strongly dependent on the presence of surface states, due to the large percentage of surface atoms in these systems. The presence of these surface states allows the PL to be modified by chemical interactions between semiconductor surface sites and an organic or inorganic passivating layer.[1,33,37,38,55-58] In the present case of block copolymer-encapsulated QDs, the interfacial PAA layer can be varied between

protonated and Cd^{2+}-neutralized forms following synthesis of the QD, providing a convenient handle on post-synthesis tuning of QD PL without affecting the external PS functionality, via the nature of interactions between PAA and the CdS surface.

The effect of chemical treatment of the PAA layer on QD PL is clearly demonstrated in Figure 2.3, which compares the PL emission spectra of the four samples MIC-CdS1 - MIC-CdS4 dispersed in toluene solutions. All QD solutions were prepared with optical densities < 0.1 at 400 nm, to ensure that auto-absorption effects were negligible. MIC-CdS1 shows a broad red-shifted emission band centered at 613 nm, which is attributed to recombination from a distribution of deep trap states localized at the QD surface.[37,38,48] A very weak band-edge emission (455 nm) is also visible, attributed to recombination from band-edge or near band-edge states. The low intensity of band-edge emission compared to trap state emission suggests a high density of surface trap states in MIC-CdS1 and a correspondingly high probability of crossover to these traps once an exciton is created by light absorption.

A dramatic increase in the relative intensity of band-edge emission is seen following conversion of the PAA layer to its cadmium carboxylate form in MIC-CdS2, suggesting a decrease in the density of trap states via changes in interactions between the PAA layer and the QD surface (Figure 2.3). From Figure 2.4 A, it is evident that the position and shape of the narrow and broad bands were unchanged when emission spectra of MIC-CdS2 were obtained at different excitation wavelengths from 350 to 425 nm, a further indication of a narrow QD size distribution. Normalized excitation spectra of MIC-CdS2 obtained for emission wavelengths corresponding to the maxima of the

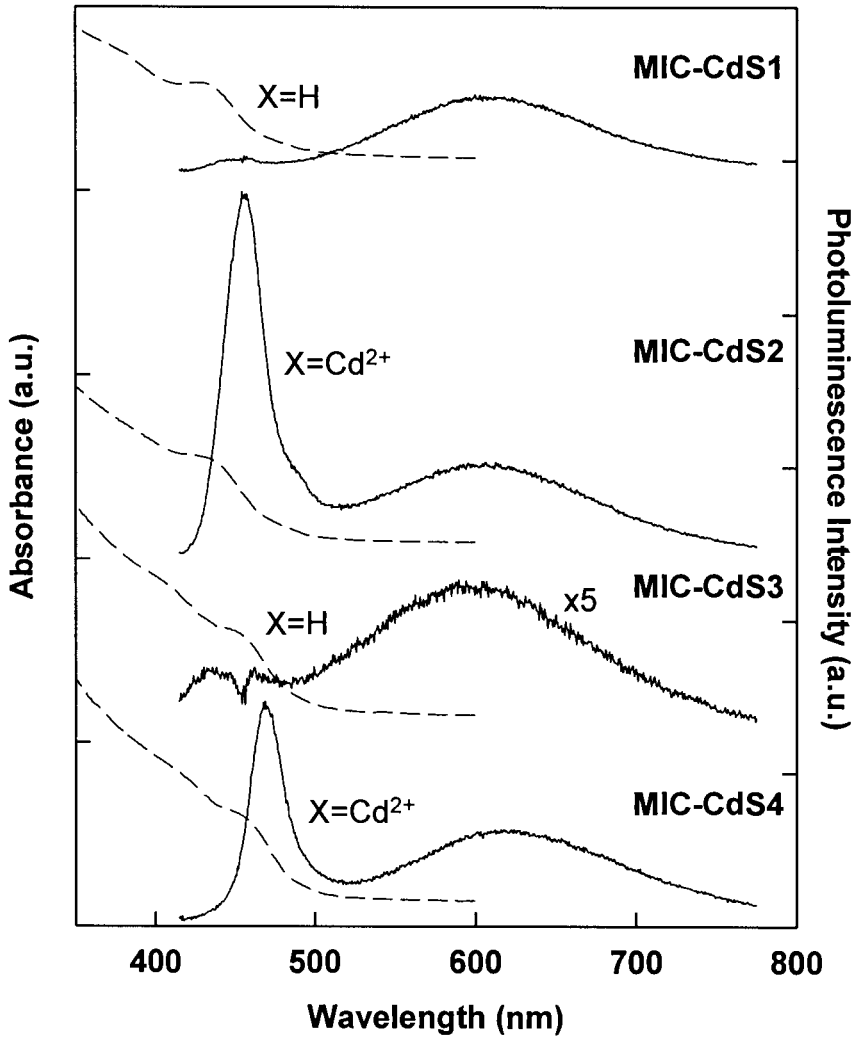

Figure 2.3. Absorption and photoluminescence emission spectra (λ_{ex} = 400 nm) for the four PS-*b*-PAA-stabilized CdS QDs samples in toluene. The chemical form of the PAA layer is denoted COOX, where X = H or Cd^{2+}.

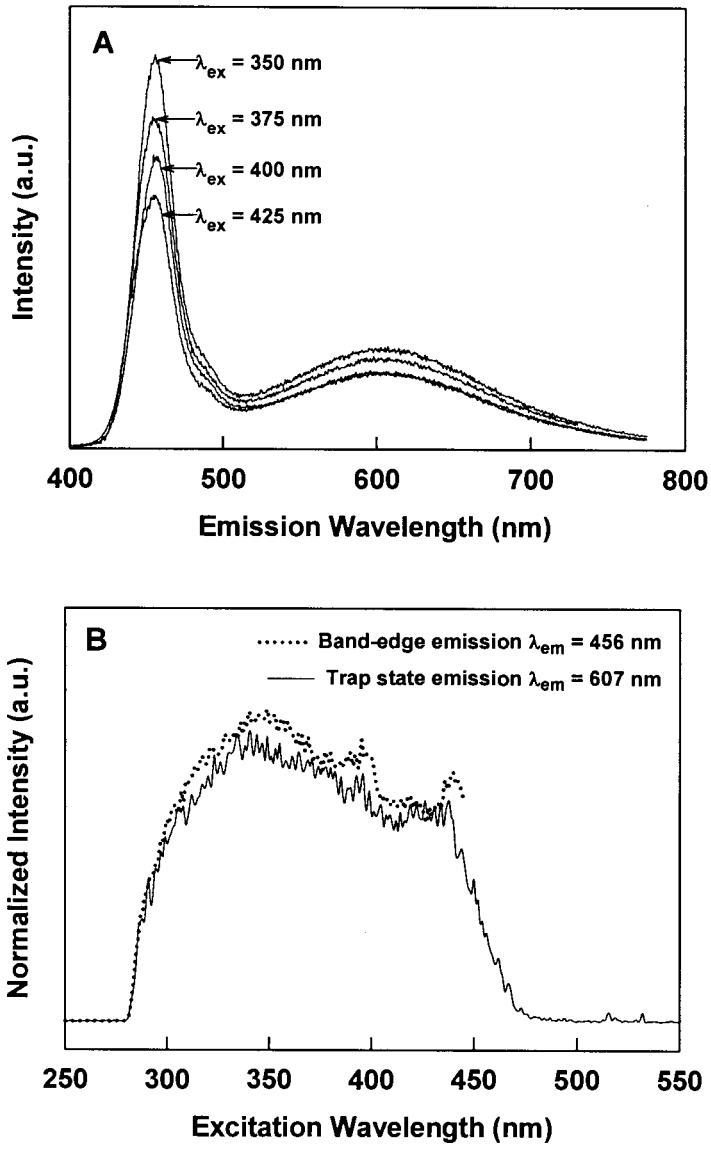

Figure 2.4. Photoluminescence emission spectra of MIC-CdS2 in toluene with various excitation wavelengths (A), and excitation spectra of MIC-CdS2 in toluene with emission wavelengths corresponding to the band-edge and trap state emission maxima (B).

narrow and broad bands show excellent overlap (Figure 2.4B), confirming that band-edge and trap state emission originate from equivalent initial excited states. Comparison of PL quantum yields (Table 2.1), shows that the conversion of the PAA layer to its cadmium carboxylate form resulted in an overall 50 % enhancement in the quantum yield of MIC-CdS2 compared to MIC-CdS1, consistent with a decrease in the density of deep trap states, from which nonradiative processes are dominant.

Table 2.1. Relative Quantum Yields for Block Copolymer-Stabilized CdS Quantum Dots in Toluene with Various Treatments of the PAA Layer

Sample	QD Diameter (nm)[a]	PAA layer: COOX, X = H, Cd^{2+}	ϕ[b]
MIC-CdS1	4.4	H	0.019
MIC-CdS2	4.7	Cd^{2+}	0.030
MIC-CdS3	5.4	H	0.006
MIC-CdS4	5.4	Cd^{2+}	0.018

[a] Determined from UV-vis absorption edge
[b] Quantum yield values determined at λ_{ex} = 400 nm using perylene in ethanol as a reference

H_2S treatment of MIC-CdS2, along with increasing the QD size, was found to reverse the effects of Cd^{2+}-neutralization on the PL, resulting in a sharp drop in the band-edge emission for MIC-CdS3 (Figure 2.3) and an overall decrease in the quantum yield (Table 2.1). The band-edge emission was shown to be re-activated by again neutralizing the PAA layer with cadmium acetate, increasing the quantum yield of MIC-CdS4 by a factor of 2 relative to MIC-CdS3. Both band-edge (469 nm) and trap state (622 nm) emission bands in MIC-CdS4 are red-shifted relative to the corresponding bands in MIC-CdS2, consistent with the increase in QD size by CdS deposition on the surface of the original nanoparticle. We note that the quantum yield of MIC-CdS3 (0.006) is lower than

the quantum yield of MIC-CdS1 (0.019), despite the fact that the PAA layer is in the acid form in both of these samples; as well, activation of MIC-CdS3 by cadmium acetate treatment results in a quantum yield for MIC-CdS4 (0.018) that is lower than the value for Cd^{2+}-neutralized MIC-CdS2 (0.030). The lower quantum yields of MIC-CdS3 and MIC-CdS4 compared with MIC-CdS1 and MIC-CdS2, respectively, suggest the formation of new surface traps states during deposition of the outer CdS layer, as well as the possible formation of defect-related traps localized below the nanoparticle surface.

Spanhel et al. proposed that surface activation of colloidal QD PL with Cd^{2+} addition at high pH is due to the passivation of hole traps localized at anionic sulfide groups at the nanoparticle surface.[37] A similar argument can be applied to the present case, where surface activation is facilitated by the chemical reactivity of the hydrophilic PAA layer. When the PAA is in its protonated form, only H-bonding interactions are possible between COOH groups in the PAA layer and SH^- anions at the CdS nanoparticle surface; these interactions are not effective in passivating the SH^- surface traps,[38,48] resulting in a high percentage of trap state emission in MIC-CdS1 and MIC-CdS3. When the PAA layer is treated with cadmium acetate, the COOH groups in the PAA layer are deprotonated, along with some of the SH^- sites at the nanoparticle surface, creating $S^{2-}\cdots Cd^{2+}\cdots{}^-OOC$ structures between the QD and PAA layer. These are similar to the $S^{2-}\cdots Cd^{2+}\cdots OH^-$ surface structures proposed by Spanhel et al.,[37] which lower the density of trap states through passivation of the anionic sulfide sites, decreasing the probability of exciton localization at the surface traps. Cadmium acetate treatment therefore results in activated QDs (MIC-CdS2 and MIC-CdS4) with enhanced band-edge emission and higher quantum yields. The maximum quantum yield we have measured in our activated

samples thus far is $\phi \sim 0.04$, lower than the $\phi > 0.50$ values that have been observed in systems of CdS activated in aqueous colloids,[37] although significantly higher than values for typical unpassivated CdS and CdSe nanoparticles in which trap emission dominates ($\phi < 0.001$).[40,59]

The demonstrated "switching" between activated and non-activated QD PL by alternating the interfacial PAA layer between acid and cadmium carboxylate forms points to possible sensor applications for these polymer-coated QDs. The sensitivity of QD PL to surface states has led to proposed applications of QDs as luminescent sensors for specific analytes, including H^+, Cd^{2+}, Zn^{2+}, Cu^{2+}, I^-, oxygen, and DNA, via activating or quenching interactions with the QD surface.[44,45,60] To our knowledge, this is the first example of Cd^{2+}-activation in a system of hydrophobic, polymer-brush coated QDs, made possible by the reactive and hydrophilic PAA layer which both concentrates Cd^{2+} at the QD surface and contributes to the resulting passivating surface structures. We note that the PS-exterior of these particles allows for easy processing via organic solvent casting to obtain optically clear and mechanically stable thin films.[20] In light of the present observations, such fluorescent polymer-QD films should have interesting potential as sensitive probes for Cd^{2+} and other analytes that activate or quench QD PL.

Further insight into the nature of the emitting states in these QD samples was obtained from decays of the emission intensity, measured at emission wavelengths corresponding to the maxima of the narrow and broad bands. As previously observed for other QD lifetime measurements,[40,44,45,49,50,61,62] none of the emission profiles could be fit to single-exponential decays, reflective of a distribution of states and QD sizes within both bands. Decay profiles were therefore fit to a multiexponential model:

$$I(t) = \sum_i \alpha_i \exp(-t/\tau_i), \qquad (2.3)$$

where two and three exponentials were used to fit band-edge and trap state emission, respectively, obtaining $\chi^2 \leq 1.2$ for all fits. It is important to note that the lifetimes of individual exponential components for these fits do not correspond to the lifetimes of actual states, but rather are used to represent average lifetimes for a broad distribution of states. We therefore report intensity-average lifetimes $\bar{\tau}$ [63] in Table 2.2, determined from the results of two- or three-exponential models using:

$$\bar{\tau} = \frac{\sum_i \alpha_i \tau_i^2}{\sum_i \alpha_i \tau_i} \qquad (2.4)$$

Table 2.2. Results of Two- and Three-Exponential Fits of Photoluminescence Intensity Decay Profiles for Band-Edge and Trap State Emission

Sample	λ_{em} (nm)[a]	Number of Exponential Terms	$\bar{\tau}$ (ns)[b]	χ^2
MIC-CdS1	613	3	244	1.01
MIC-CdS2	456	2	49	1.17
	607	3	360	1.11
MIC-CdS3	461	2	61	1.02
	610	3	324	1.15
MIC-CdS4	469	2	40	1.10
	622	3	272	1.06

[a] For all decay profiles, λ_{ex} = 400 nm

[b] Intensity-average lifetimes calculated from two- or three-exponential fits (see text)

Representative intensity decay profiles for band-edge and trap state emission are compared in Figure 2.5, showing that the broad red-shifted emission decays with a significantly longer lifetime than the band-edge emission, as has been found in other examples of Cd^{2+}-activated CdS.[44,45] The relatively long lifetimes for the red-shifted emission band (244-360 ns) supports the assumption that this band originates from localized deep trap states. The measured band-edge lifetimes (40-61 ns), though shorter than those for the red-shifted emission band, are much longer than the picosecond lifetimes which have been measured for direct band-edge recombination of an exciton.[37,40] This suggests that a significant amount of band-edge emission in this system is actually due to recombination from shallow trap states located close to the band edge, as has been observed for other systems.[37,40] We note that picosecond processes may also contribute to the band-edge emission, though these cannot be resolved due to limitations in the instrument response time.

The long-term solution stability of the PL properties was investigated for both non-activated (MIC-CdS1) and activated (MIC-CdS2) samples stored under ambient conditions. The PL spectra and quantum yields for the two samples were monitored over time following dispersion of the yellow powders in toluene (Figure 2.6). To better compare the relative intensities of band-edge and trap state emission, the emission spectra collected at various times are normalized, with the respective quantum yields shown in the insert. For MIC-CdS1, the shape of the dominant broad trap emission does not change considerably over 56 days, indicating that the nature of the surface states remain constant. However, the quantum yield decreases by a factor of 3 over this same time period, suggesting an increase in nonradiative recombination pathways for the surface traps

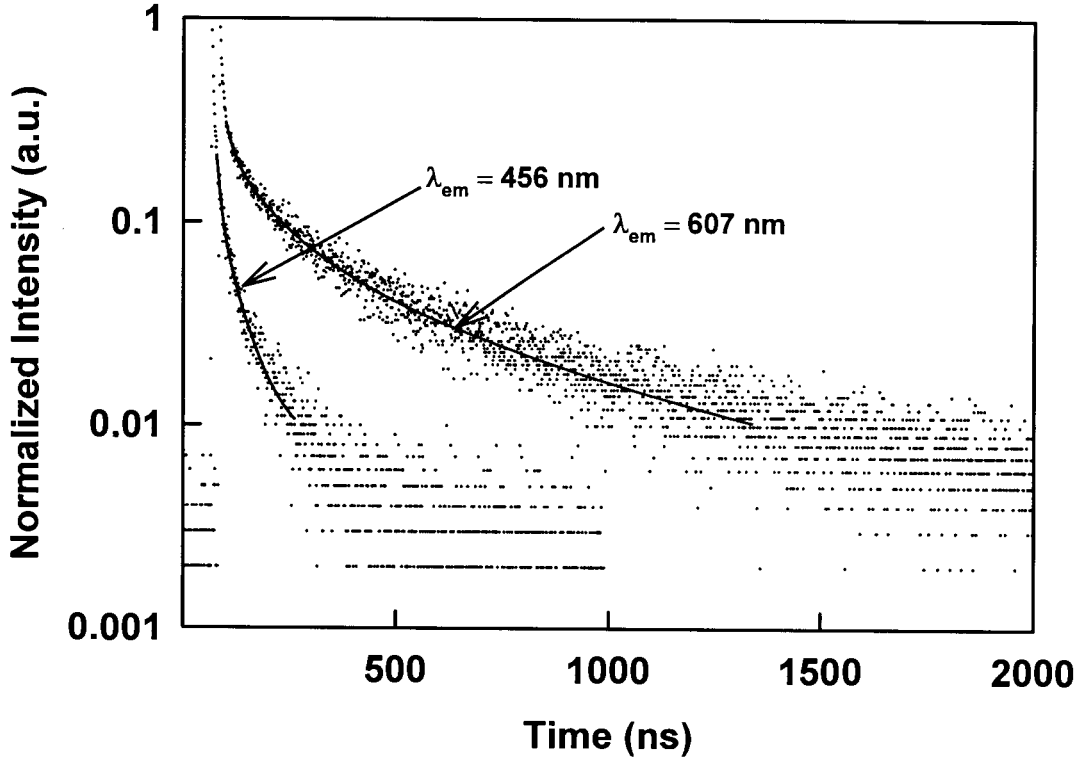

Figure 2.5. Comparison of band-edge (λ_{em} = 456 nm) and trap state (λ_{em} = 607 nm) emission decay profiles for MIC-CdS2 in toluene and resulting two- and three-exponential fits, respectively.

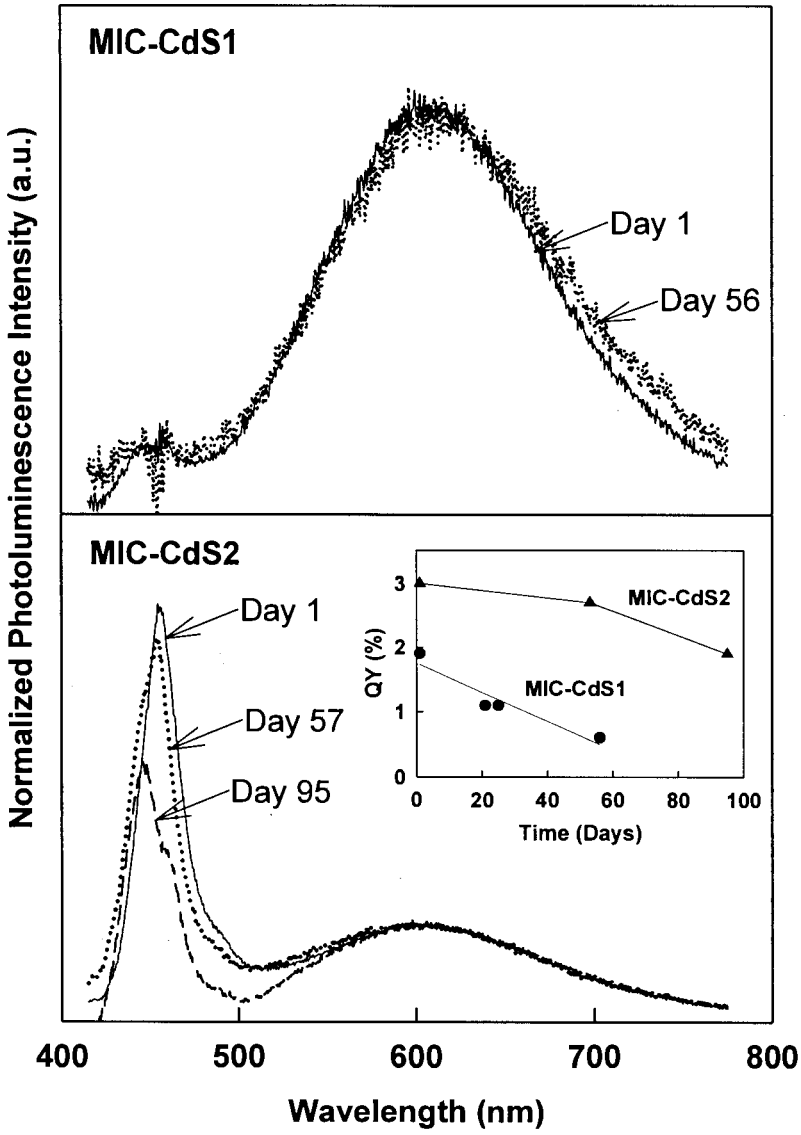

Figure 2.6. Photoluminescence emission spectra (λ_{ex} = 400 nm) of MIC-CdS1 and MIC-CdS2 in toluene after various periods of aging under ambient conditions. The emission spectra have been normalized to allow comparison of relative intensities of band-edge and trap state emission. The measured quantum yields at various times are shown in the insert.

as the particles age in toluene. The activated sample, MIC-CdS2, along with having a higher initial quantum yield, shows a much greater stability than MIC-CdS1, maintaining 90 % of its PL after 57 days in toluene solution. Over this time period, the shape of the broad trap state emission remains constant, although the band-edge emission shows a slight blue-shift and decrease in intensity relative to the trap state emission. After 95 days in toluene, the band-edge emission of MIC-CdS2 decreases more significantly, with a concomitant decrease in the quantum yield. These observations are consistent with the slow oxidation of the activated QD surface of MIC-CdS2 over long periods of time in toluene solution. Surface oxidation of QDs is a well-established mechanism of nanoparticle degradation, and has been found to result in a decrease in QD size and increase in the density of surface traps by the formation of new anionic sulfide sites.[56,64] For typical TOPO-stabilized QDs exposed to air, the dramatic loss of PL intensity due to nanoparticle degradation is extremely rapid process, occurring over the course of several minutes.[64] The impressive degree of stability for MIC-CdS2 over several months of aging in toluene is therefore very encouraging, pointing to the protective nature of the polymer layer.

After MIC-CdS1 and MIC-CdS2 were aged in toluene, we found that the original PL properties of the QDs could be restored, and even enhanced, by direct activation of the aged toluene solutions. For these experiments, the aged QD solutions in toluene were first titrated with an excess of 4x NaOH in methanol (relative to the number of acrylic acid units), followed by titration with cadmium acetate in methanol until the quantum yield of the solution reached a maximum value (Figure 2.7). The aged non-activated sample MIC-CdS1 showed only weak broad trap emission before NaOH addition, with

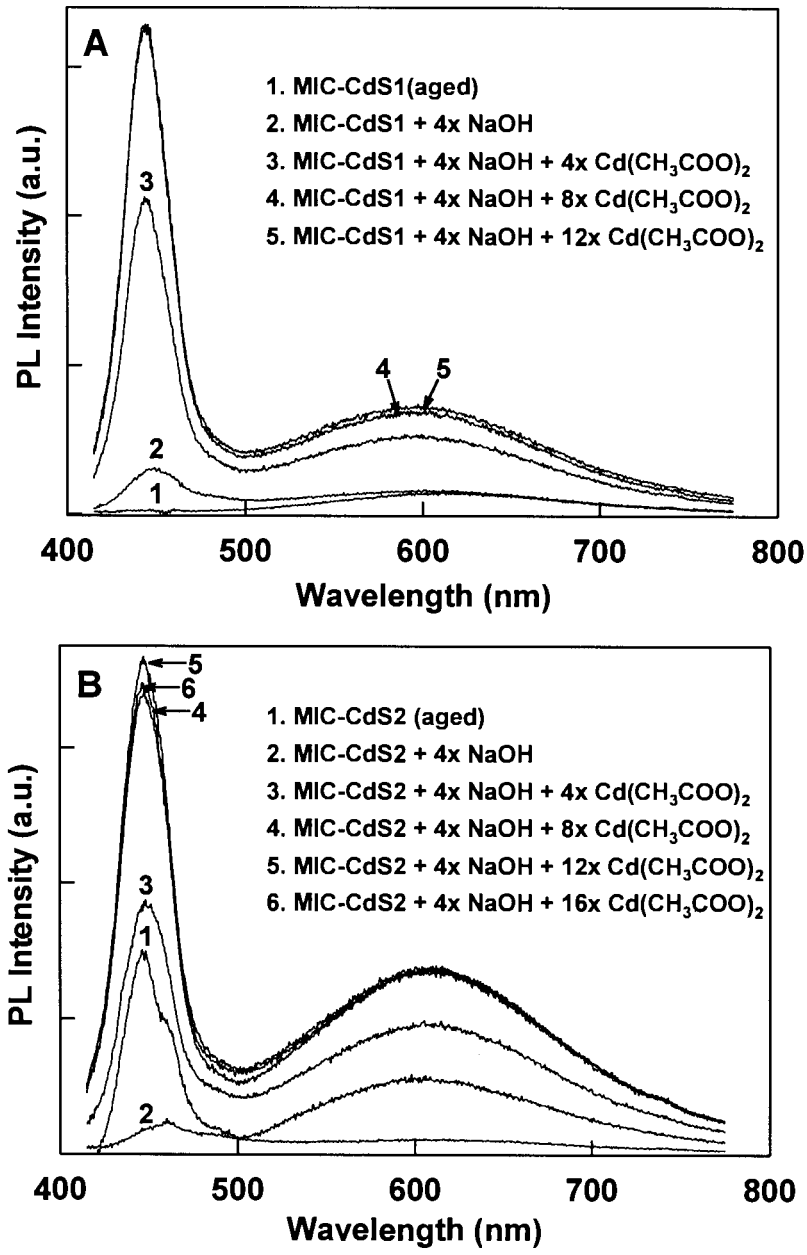

Figure 2.7. Photoluminescence emission spectra (λ_{ex} = 400 nm) of aged MIC-CdS1 (A) and MIC-CdS2 (B) in toluene with various subsequent treatments of added NaOH and $Cd(CH_3COO)_2$ in methanol.

even weaker band-edge emission (ϕ = 0.06) (Figure 2.7A). Addition of excess NaOH resulted in a small increase in band-edge emission. This small activation effect is not attributed to Na_2S deposition on the QD surface, which has been found to quench, rather than activate PL;[50]rather, we believe that a small number of SH^- sites were passivated by deprotonation with NaOH, followed by reaction with Cd^{2+} ions that had been released into the PAA layer during QD surface oxidation.[64] Subsequent addition of Cd^{2+} ions resulted in a steady increase in both band-edge and trap state emission, until a maximum quantum yield of 0.037 was obtained for the originally non-activated MIC-CdS1. The increase in trap state emission suggests that the formation of an increasing number of passivating groups on the QD surface, along with lowering the density of trap states, also increases the amount of radiative recombination from the remaining traps, as was found in the activation experiments of Spanhel et al.[37]

A similar effect was found for the aged activated sample MIC-CdS2, which had lost much of its original PL intensity due to surface oxidation during 95 days in toluene (ϕ = 0.019). In this case, the initial addition of NaOH was found to quench the PL (Figure 2.7B), though subsequent titration with Cd^{2+} resulted in an increase in activation until the quantum yield reached 0.036. The observed quenching with NaOH addition is explained in terms of the large excess of Na^+ ions, which can displace Cd^{2+} ions from passivating $S^{2-}\cdots Cd^{2+}\cdots {}^-OOC$ structures at the QD surface.[50] As well, we note that after the maximum quantum yield was obtained, subsequent addition of cadmium acetate resulted in a slight decrease in the band-edge emission. This was probably due to a competing quenching effect associated with the added methanol, since hydrogen bonding is known to compete with passivating interactions with trap sites on the surface of CdS.[38,47]

To explore the selectivity of PS-*b*-PAA-stabilized QDs as chemical sensors for Cd^{2+} ions, we compared the effects of adding increasing quantities of cadmium or magnesium acetate to toluene QD solutions on the PL activation of the band-edge emission region. The results in Figure 2.8 were obtained from two separate solutions of identical concentration of the sample MIC-CdS5; in both the cadmium and magnesium acetate titration experiments, curve 1 represents the original untreated sample in the protonated form, and curve 2 represents the sample after the addition of 4x NaOH in methanol. Curves 3-6 clearly show the effects on each QD solution of the further addition of identical quantities of methanolic solutions of cadmium (above) or magnesium (below) acetate. Whereas cadmium acetate addition results in a progressive increase in the intensity of band-edge emission, magnesium acetate shows no such effect, suggesting that this is an ion-selective activation effect, in agreement with the mechanism proposed above.

2.3.3. Effect of Surface Chemistry on the Solution Structure of PS-b-PAA-Stabilized QDs

We found that all four samples MIC-CdS1-MIC-CdS4 could be dispersed in various organic solvents, including toluene, tetrathydrofuran (THF), and chloroform, to yield stable clear yellow solutions that showed no precipitation over a time period of up to several months. This indicated that all PS-*b*-PAA-stabilized QD samples were solubilized and well stabilized by the PS brush layer, irrespective of the chemical form of the PAA layer. However, we were interested in determining more precisely the structure of our polymer-coated QDs in organic solvents, and how their solution structure was

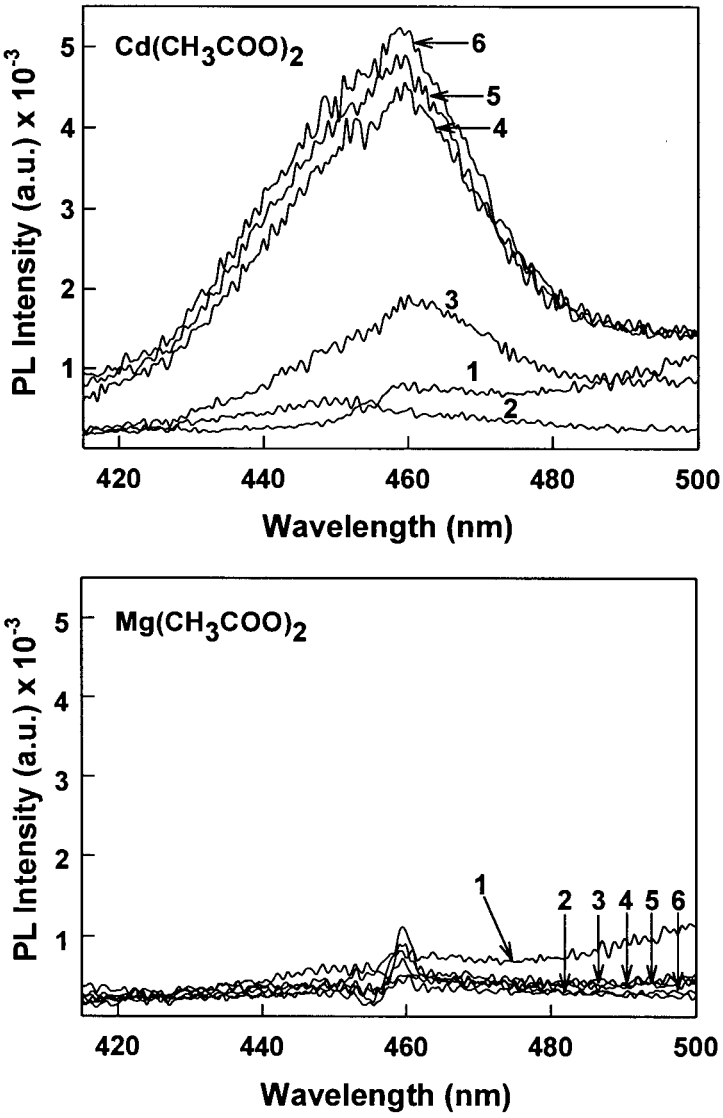

Figure 2.8. Comparision of photoluminescence emission (λ_{ex} = 400 nm) in the band-edge region for MIC-CdS5 in toluene with the addition of increasing amounts of cadmium or magnesium acetate. 1: untreated MIC-CdS5; 2: MIC-CdS5 + 4x NaOH; 3: MIC-CdS5 + 4x NaOH + 4x $M(CH_3COO)_2$; 4: MIC-CdS5 + 4x NaOH + 8x $M(CH_3COO)_2$; 5: MIC-CdS5 + 4x NaOH + 12x $M(CH_3COO)_2$; 6: MIC-CdS5 + 4x NaOH + 16x $M(CH_3COO)_2$; M = Cd^{2+} (above) or Mg^{2+} (below).

influenced by the nature of the PAA layer. It has previously been found for polystyrene-*b*-poly(methacrylic acid) (PS-*b*-PMMA) block ionomers that micelle aggregation numbers are significantly higher when the PMMA block is in its neutralized form, due to a greater difference in the solubilities of the two blocks.[65] Moreover, a combination of SEC and dynamic light scattering results suggest that protonated PS-*b*-PMMA[65] and PS-*b*-PAA[52] diblocks exist as molecularly solubilized single chains in hydrogen-bonding solvents such as THF, due to favourable interactions between the solvent and the acid block and a correspondingly low driving force for micellization. In light of the latter observation, it is perhaps surprising that our acid-form QD samples (MIC-CdS1 and MIC-CdS3) are stable in THF, since solubility differences alone may not be sufficient to maintain the encapsulating micelle structure.

Further insight into this question is obtained from size-exclusion chromatography (SEC) of the four samples, in which low-angle light scattering (LALS) detection allows the apparent molecular weight of the samples to be determined without reference to standard calibration, by measuring the scattered light intensity at a single low angle ($\theta = 7°$) as the sample is eluted from the column. For these calculations, we used the *dn/dc* value for polystyrene in THF, 0.185, since the effects of chemical heterogeneity will be small considering the low weight fraction of the PAA and CdS components (< 10 wt %). The RI-SEC traces for the four samples in THF solution are shown in Figure 2.9. All four samples show a relatively broad peak, attributed to the polymer-coated QDs, along with a low-molecular weight shoulder. This shoulder was not sufficiently resolved to determine its molecular weight independently, although its elution volume matched perfectly with the original unmicellized ester form of the

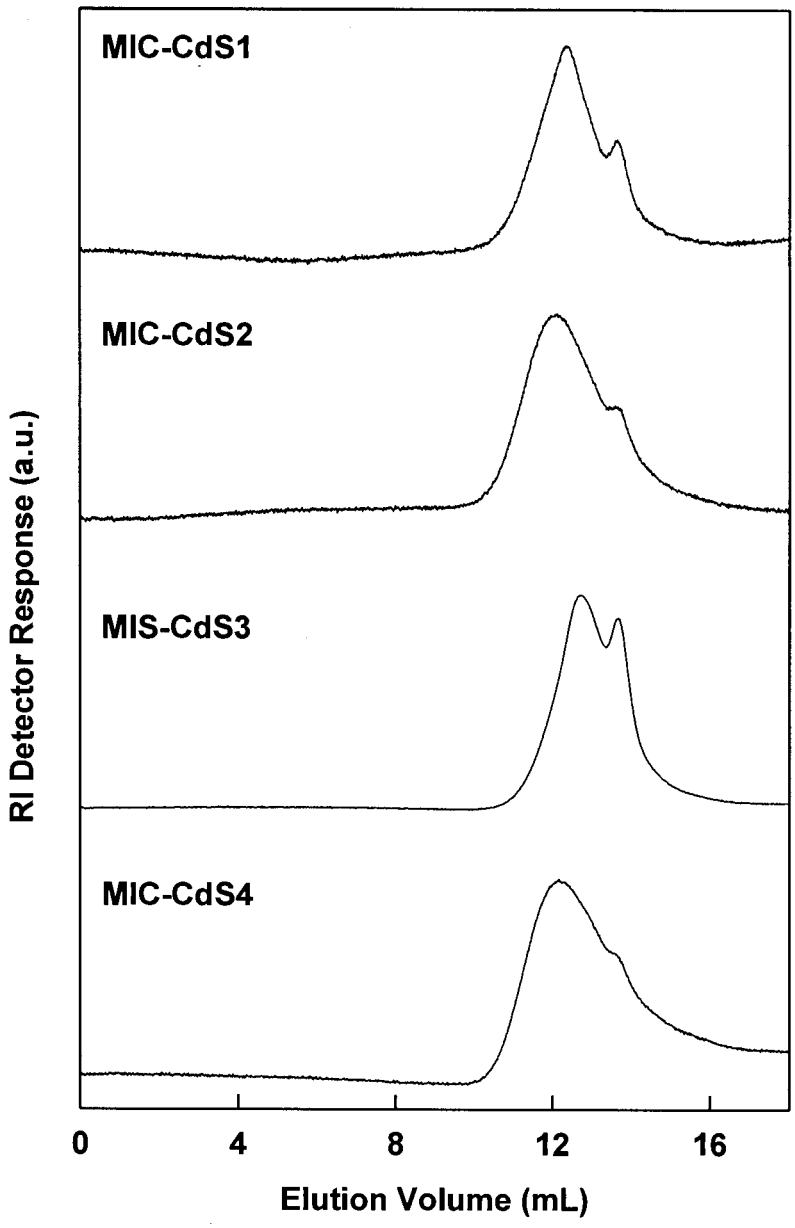

Figure 2.9. Size-Exclusion chromatograms (refractive index detector response) for the four samples of PS-*b*-PAA-stabilized CdS QDs in THF.

PS(330)-*b*-PtBA(20) copolymer; it was therefore attributed to a "single chain" fraction within each sample. We note that the single chain shoulder is significantly sharper in MIC-CdS1 and MIC-CdS3, compared to MIC-CdS2 and MIC-CdS4, suggesting a larger fraction of unassociated single chains when the PAA layer is in its acid form. More compelling evidence came from the determination of the weight-average molecular weights for each sample, by integrating the RI and LALS traces for each of the broad peaks. Table 2.3 shows the resulting M_w and average block copolymer aggregation numbers Z for MIC-CdS1 - MIC-CdS4, as well as values for the original cadmium-neutralized micelles. For all of the cadmium-neutralized samples, including the original block ionomer micelles, Z values are in the range of 96-105, while for the two QD samples in which the PAA layer is in its acid form (MIC-CdS1 and MIC-CdS3), Z values

Table 2.3. Weight-Average Molecular Weights and Block Copolymer Aggregation Numbers Z of PS-*b*-PAA-Stabilized CdS Quantum Dots in THF

Sample	M_w (g/mol) x 10^{-6} [a]	Z
MIC-Cd	3.49	96
MIC-CdS1	0.90	24
MIC-CdS2	3.84	105
MIC-CdS3	0.75	20
MIC-CdS4	3.81	104

[a] Determined using GPC from RI and LALS detector signals as described in the text

are about a factor of five lower, in the range of 20-24, consistent with the observed larger fraction of single chains in these samples. For one of our samples, MIC-CdS4, we have also carried out multi-angle static light scattering measurements in THF to compare the

more typical Zimm plot method by static light scattering (SLS) with the LALS-SEC results. The basic of SLS theory is that when colloidal particles are of sufficient size ($> \lambda /20$), they are found to scatter light according to the following Zimm Plot Equation:

$$\frac{KC}{R(\theta)} = \frac{1}{M_w P(\theta)} + 2A_2 C \qquad (2.5)$$

where $R(\theta)$ is the Rayleigh ratio at the angle of measurement, $P(\theta)$ is the particle scattering function, M_w is the weight-average molecular weight of the particle, and A_2 is the second virial coefficient. K is an optical parameter and defined as:

$$K = 4\pi^2 n^2 (dn/dc)^2 / (\lambda_o^4 N_A) \qquad (2.6)$$

where n is the refractive index of the particle and dn/dc is the specific refractive index increment at constant chemical potential, N_A is Avogadro's number, and λ_o is the wavelength of scattered light in a vacuum. In addition, $1/P(\theta)$ can be expanded to give:

$$1/P(\theta) = 1 + (16\pi^2/3\lambda^2) R_g^2 . \sin^2(\theta/2) \qquad (2.7)$$

where R_g is the radius of gyration and θ is the angle of measurement. A plot of $KC/R(\theta)$ vs. $\sin^2(\theta/2)$ yields a so-called Zimm plot where M_w, R_g and A_2 can be obtained. The Zimm plot method gives an aggregation number of ~320 in THF, which is about a factor of three greater than the value obtained by LALS-SEC. The reason for this discrepancy is

unclear at present, although one explanation is that a fraction of large supermicellar aggregates in THF contribute to the average molecular weight as determined by the Zimm plot method; these aggregates may by retained by the column and so are not detected by the SEC method.

Considering the similar aggregation numbers determined by LALS-SEC for all of the cadmium-neutralized samples, it is reasonable to propose that chain aggregation in these cases is driven by the low solubility of the PACd blocks in THF. The lower aggregation numbers for MIC-CdS1 and MIC-CdS3 could then be explained by a greater solubility of the single chains in their acid form, and a correspondingly lower tendency to form micelles. However, in previous studies of PS-*b*-PMAA[65] and PS-*b*-PAA[52] with relatively short acid blocks, reverse micelles were not observed in THF for the copolymers in the acid form. It is therefore possible that chain aggregation about the CdS QDs in MIC-CdS1 and MIC-CdS3 is not driven by solubility differences between blocks, but by H-bonding interactions between the PAA blocks and SH^- groups at the QD surface. Compelling support for this model comes from a calculation of the number of sulfur atoms on the surface of a 4.4 nm QD in MIC-CdS1, determined to be 364, assuming bulk CdS density and 0.35 nm for a CdS monolayer.[66] This agrees very well with chain aggregation numbers (Z~20) determined from LALS-SEC for these structures, which for a 20 unit PAA block would result in ~400 COOH groups at the QD surface. Comparison of the proposed structures for MIC-CdS1 and MIC-CdS2 in THF is shown in Scheme 2.3. In this cartoon, all of the chains in the PAA layer of MIC-CdS1 interact directly with the QD surface through H-bonding. In contrast, when the PAA layer is in its neutralized form, a thicker PACd layer forms around the QD, driven by microphase-separation of the

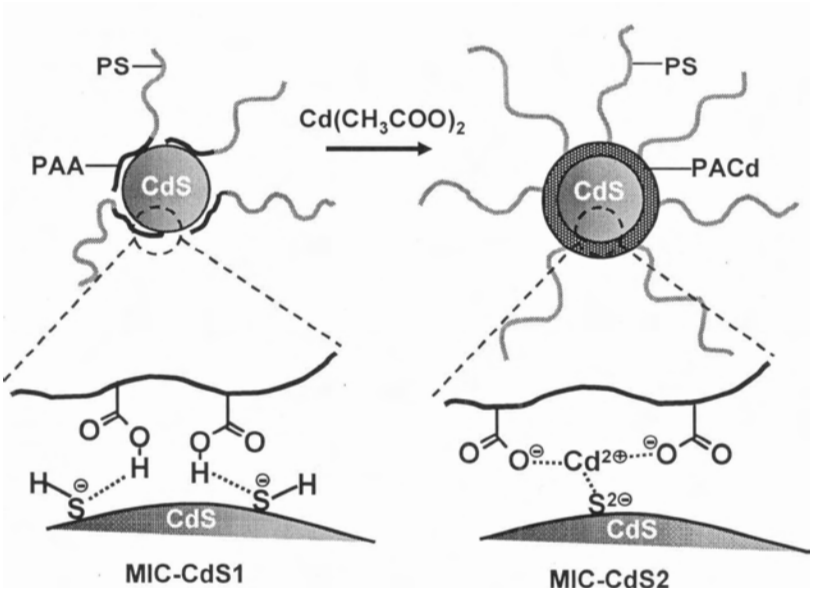

Scheme 2.3. Proposed structures for MIC-CdS1 and MIC-CdS2 in THF

insoluble ionic blocks. In the latter case, the QDs can be said to be embedded in the core of an ionomer micelle, the structure of which is maintained by interfacial tension between PACd and solvent. Similar differences in aggregation numbers should exist in other organic solvents, although aggregation numbers may be somewhat higher in less polar solvents.[65] The thicker PACd layer surrounding the QDs in MIC-CdS2, compared to the H-bonded PAA layer in MIC-CdS1 (Scheme 2.3), may in part explain the greater long-term PL stability in the former sample, due to protection of the QD surface with a stable and continuous polymer layer which is kinetically "locked in" by the high T_g of PACd and by ionic Cd^{2+} cross-links.

To obtain further structural information on the polymer-coated QDs in organic solvents, we carried out dynamic light scattering (DLS) measurements for all four samples in toluene solutions over a range of scattering angles and concentrations. For all measurements, the normalized time correlation function of the electric field was analyzed

using a cumulant expansion:

$$|g(\tau)| = \exp(-\overline{\Gamma}\tau)\cdot[1+(\mu_2/2!)\tau^2+...] \qquad (2.8)$$

where $\overline{\Gamma}$ is the mean relaxation rate and μ_2 is the second moment. Mean relaxation rates were determined for various scattering angles between 35° and 120°, and the effective translational diffusion coefficient D_T was determined using the following relation for diffusive motion of particles:

$$\overline{\Gamma} = D_T q^2 \qquad (2.9)$$

where q is the scattering vector, which is related to the refractive index of the scattering medium, n, the wavelength of incident light, λ, and the scattering angle θ by the following relation:

$$q = (4\pi n/\lambda)\sin(\theta/2). \qquad (2.10)$$

To correct for interparticle interactions, the effective diffusion coefficient at various concentrations was extrapolated to infinite dilution to obtain D_0:

$$D_T = D_o(1+k_d C), \qquad (2.11)$$

where k_d is the concentration coefficient and C is the concentration. From D_0, the

hydrodynamic radius R_h of the particles could then be determined from the Stokes-Einstein relation:

$$R_h = kT / 6\pi\eta D_0 \qquad (2.12)$$

where k is the Boltzmann constant, T is the temperature, and η is the solvent viscosity. We note that R_h determined by DLS is an inverse reciprocal z-average of the distribution of particle sizes, which follows from the scattering intensity-weighting of the diffusion coefficient.

For each cumulant fit, the ratio $\mu_2 / \overline{\Gamma}^2$ is a measure of the polydispersity of particle sizes, which ranged from 0.10 to 0.30, indicating a significant size distribution. Average polydispersity values (Table 2.4) for MIC-CdS1 and MIC-CdS3 (0.29 and 0.28, respectively) were higher than those for MIC-CdS2 and MIC-CdS4 (0.20 and 0.15, respectively). This is consistent with the greater percentage of single chains in MIC-CdS1 and MIC-CdS3 observed by SEC, and suggests a lower driving force for chain aggregation for the two samples with protonated PAA layers.

Table 2.4. Summary of Dynamic Light Scattering Results for Various Block Copolymer-Stabilized CdS Quantum Dots in Toluene

Sample	D_0 (nm^2s^{-1}) x 10^{-7}	R_h (nm)	$\mu_2 / \overline{\Gamma}^{2\,a}$	k_d (cm^3g^{-1})
MIC-CdS1	2.13	18	0.29	-0.00118
MIC-CdS2	1.65	23	0.20	-0.00054
MIC-CdS3	1.32	29	0.28	-0.00006
MIC-CdS4	1.03	37	0.15	-0.00014

[a] Polydispersity values averaged over all concentrations and angles for each sample

For all samples and at all concentrations, $\overline{\Gamma}$ was found to scale linearly with q^2, indicating a diffusive relaxation mode from the free translational diffusion of particles. Representative plots of $\overline{\Gamma}$ vs. q^2 for MIC-CdS2 at various concentrations in toluene are shown in Figure 2.10A. Figure 2.10B shows plots of effective diffusion coefficients D_T as a function of concentration for each sample, and the resulting linear extrapolations to infinite dilution; all of these plots show small negative values of k_d (Table 2.4), consistent with previous studies of PS-based block ionomer micelles in organic solvents.[65,67] The hydrodynamic radii R_h of the four samples in toluene (Table 2.4) range from 18 nm for MIC-CdS1 to 37 nm for MIC-CdS4, increasing with each subsequent treatment of the PAA layer. This range of sizes agrees with previous DLS measurements of block ionomer micelles with PS coronal blocks ~300 units in length,[67] suggesting that these polymer-coated QDs exist as non-aggregated "brush-like" particles in toluene. The hydrodynamic radius of a spherical polymer brush in a good solvent is known to increase with Z, due to steric-induced chain stretching within the brush. The increases in R_h from MIC-CdS1 to MIC-CdS2, and from MIC-CdS3 to MIC-CdS4 (Table 2.4), can therefore be understood in terms of increases in aggregation number with Cd^{2+}-neutralization of the PAA layer, as observed by SEC in THF solution. The increase in R_h from MIC-CdS2 to MIC-CdS3, however, requires more speculation, since SEC results show that the aggregation number of MIC-CdS3 is a factor of five lower in THF solution than MIC-CdS2. Part of this apparent discrepancy in R_h may be related to the increase in size of the encapsulated CdS QD between MIC-CdS2 and MIC-CdS3: subsequent rearrangement of chains with dispersion in toluene may result in non-uniform packing of copolymer on the

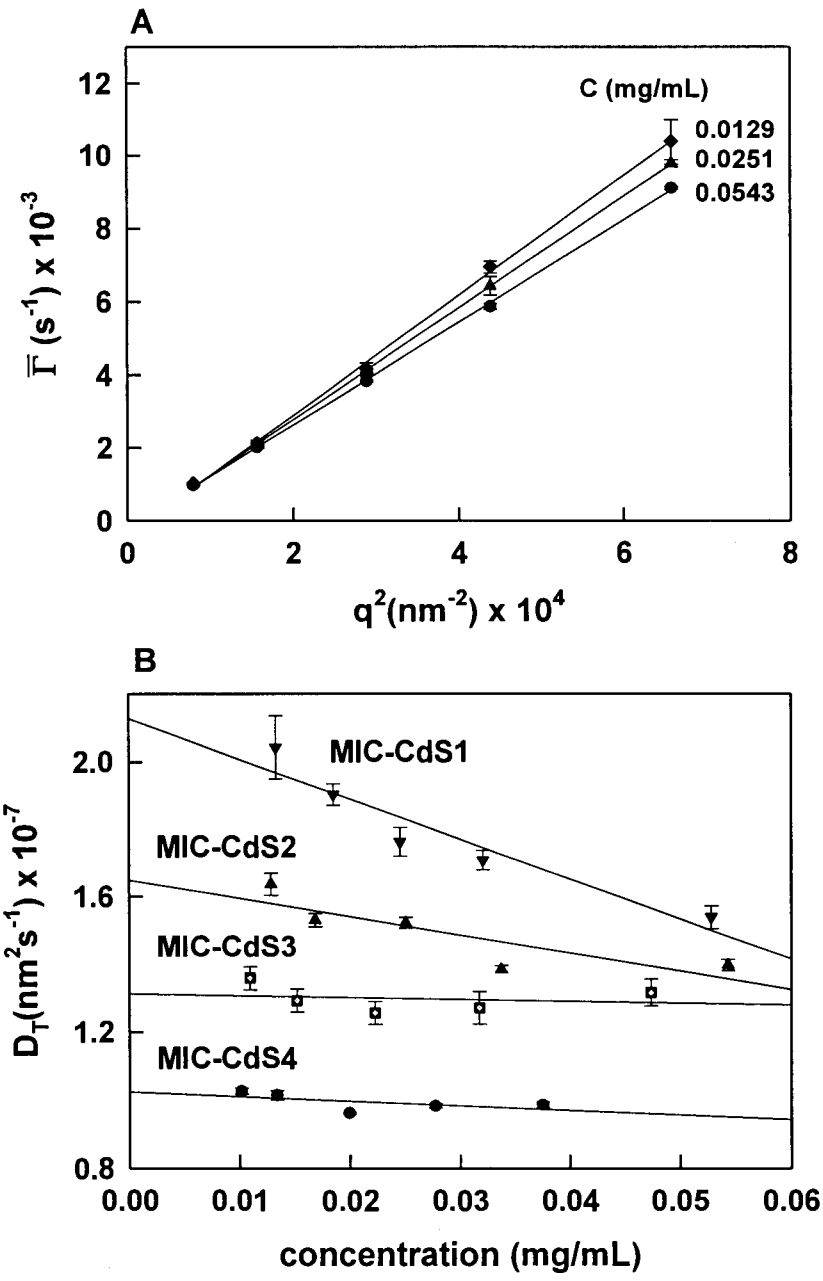

Figure 2.10. Dynamic light scattering data for the four samples of PS-*b*-PAA-stabilized CdS QDs in toluene. Representative plots of $\overline{\Gamma}$ vs. q^2 for various concentrations of MIC-CdS2 in toluene (A), and plots of effective diffusion coefficient D_T vs. concentration for the four samples (B).

surface of the larger QD, such that chain stretching increases despite a lowering of the aggregation number.

2.3.4. QD/PS Homopolymer Blend Films

In order to demonstrate their effectiveness as dispersible building blocks in polymeric environments, the PS-*b*-PAA-stabilized QDs were solution-blended with PS homopolymer, then cast onto glass substrates to obtain optically transparent photoluminescent films. 20 wt % of the polymer-coated QDs MIC-CdS4 was blended with 80 wt % of either a high- or low-molecular weight PS homopolymer (PS(1250) and PS(100), respectively). Both of the resulting blend films had good mechanical properties, although the film containing the low-molecular weight PS showed a number of cracks following evaporation of solvent. Both blends could be peeled from the glass substrates to produce free-standing films.

Laser scanning confocal fluorescence microscopy (LSCFM) images of the QD blend films prepared using PS(100) (Figure 2.11A) and PS(1250) (Figure 2.11B) both showed uniform PL throughout the ca. 25 μm-thick films with 488 nm excitation, indicating that the CdS QDs showed no discernible phase separation from PS(100) or PS(1250) on optical length scales. The dark lines observed in Figure 11A are cracks in the film formed during solvent evaporation. No such cracks were observed in the QD blend film containing the higher molecular weight homopolymer PS(1250). Transmission electron microscopy images (Figure 2.11C and D) provide a higher resolution picture of the structure of these films, revealing excellent dispersion of CdS

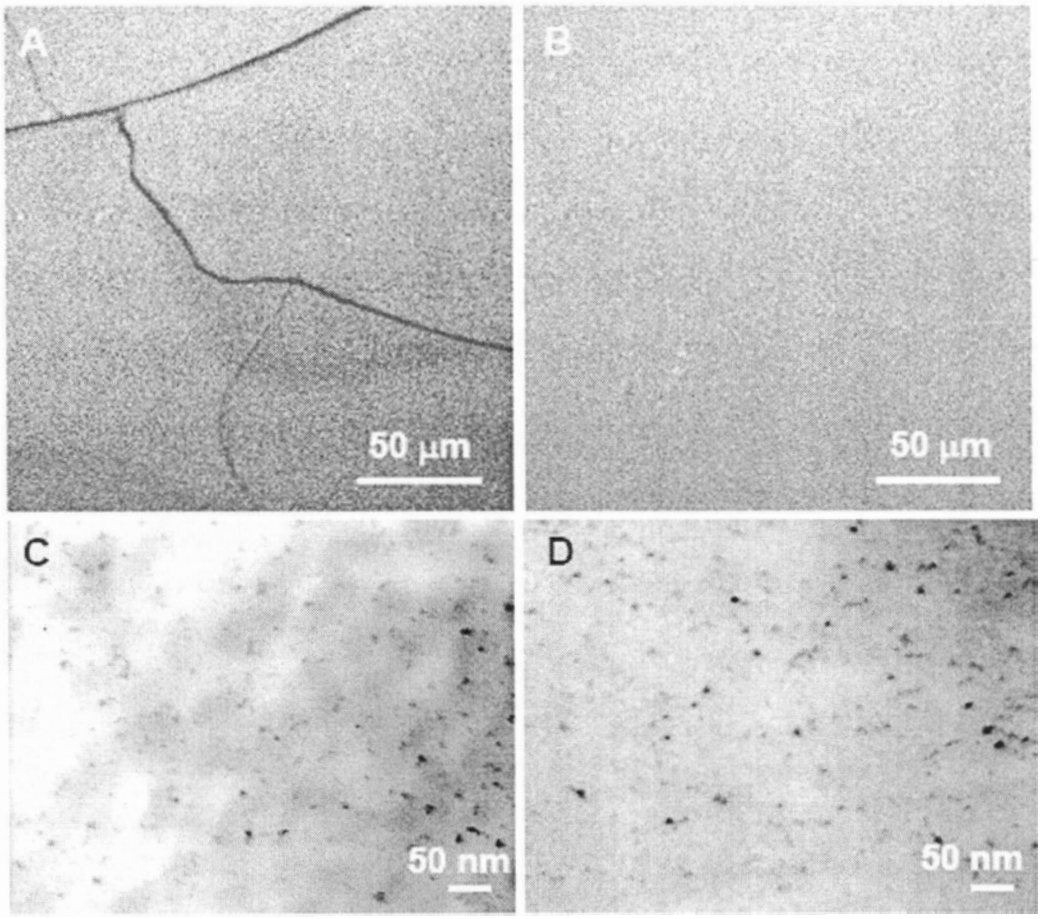

Figure 2.11. Laser scanning confocal fluorescence microscopy (LSCFM) images of films of 20/80 w/w MIC-CdS4/PS(100) (A) and 20/80 w/w MIC-CdS4/PS(1250) (B); Transmission electron microscopy (TEM) images of films of 20/80 w/w MIC-CdS4/PS(100) (C) and 20/80 w/w MIC-CdS4/PS(1250) (D).

QDs throughout the PS matrix in both cases, with no observed agglomeration of nanoparticles. LSCFM and TEM images were also obtained after annealing the films at 115°C, above the T_g of PS, for 8 days: the results in both cases were identical to those before annealing. Clearly the PS brush layer of the PS-*b*-PAA-stabilized QDs provides favourable interactions with both PS(100) and PS(1250) homopolymer, such that the films are thermodynamically stable "solid solutions" of QDs in a polymer "solvent".

PL emission spectra obtained for the QD blend films were nearly identical to that of the MIC-CdS4 colloidal building blocks dispersed in toluene. Figure 2.12 compares the emission spectra of the MIC-CdS4/PS(1250) film with that of a dilute toluene solution of MIC-CdS4, revealing that the position and shape of the QD band-edge and trap state emission are the same in both environments. The nearly identical emission spectra in Figure 2.12 indicate that no significant increase in particle size has occurred through solution casting and film formation. As well, these results demonstrate that the PAA layer of the block copolymer, along with providing a route to chemically tuning the QD PL, also maintains a constant surface environment for the QDs while the PS brush layer is dispersed in different environments, such that the nature of surface trap states are the same both in dilute toluene solutions and in polymer blend films. We note that the constant QD surface environment is a function of the high interfacial tension between the PACd layer and the nonpolar external environment of the PS brush layer, which will exclude solvent molecules from interacting with the QD surface, even as the PS brush is solubilized in different media

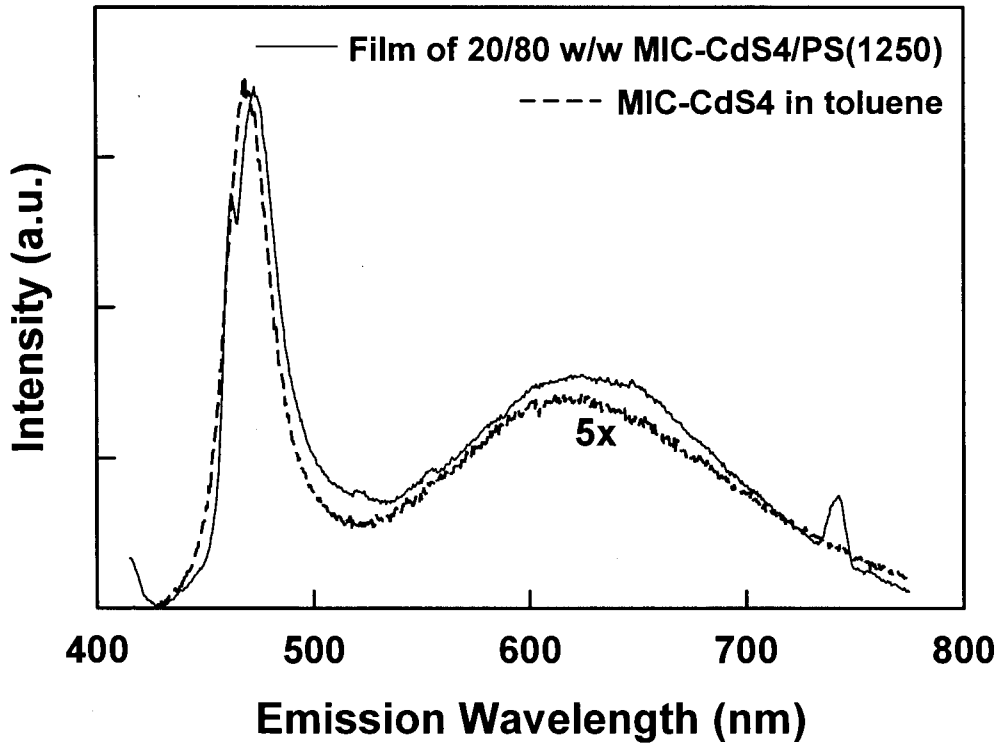

Figure 2.12. Comparison of photoluminescence emission (λ_{ex} = 400 nm) from MIC-CdS4 dispersed in toluene and a film of 20/80 w/w MIC-CdS4/PS(1250).

2.4. Conclusions

This chapter describes the first study of static and time-resolved PL from PS-*b*-PAA-stabilized CdS QDs, demonstrating surface tunable PL via chemical treatment of the PAA layer at the surface of the quantum dot. When the PAA layer is in its protonated form, only broad trap state emission was observed, while neutralization of the PAA layer with cadmium acetate resulted in a reversible sharp increase in the band-edge emission and quantum yield. The "switchable" PL properties are attributed to passivation of SH^- trap states at the surface of the QDs by cadmium carboxylate groups in the neutralized PAA layer, which can be reversed by re-protonation of the acid groups. It was also shown that Cd^{2+} activation of PL does not occur when Mg^{2+} ions are added to similar QD solutions, indicating potential of these block copolymer-stabilized QDs as Cd^{2+}-selective sensors. Excellent long-term stability of the PL was found for PS-*b*-PAA-stabilized QDs dispersed in toluene, with only a 10 % loss in PL for the dispersion MIC-CdS2 over 57 days under ambient conditions. Dynamic light scattering and SEC measurements with LALS detection revealed significant changes in the aggregation numbers and hydrodynamic radii of the colloidal QDs for different treatments of the PAA layer, with higher block copolymer aggregation numbers for QD samples with a Cd^{2+}-neutralized PAA layer, attributed to a lower solubility of the PACd blocks compared to the acid-form PAA blocks. Finally, it was demonstrated that the PS-*b*-PAA-stabilized QDs could be well dispersed in a matrix of PS homopolymer, producing photoluminescent films which retained the emission features of the constituent colloidal QDs.

This combination of surface-tunable optical properties, provided by the PAA layer, and solubility and stability in polymer and organic media, provided by the PS layer,

make PS-*b*-PAA-stabilized QDs ideal candidates as building blocks for higher-order hierarchical structures with potential applications in sensors, biological imaging, and photonic devices.

One aspect of this system that remains to be explored is the further optimization of PL quantum yields, which will be critical for many photonic and bio-labeling applications requiring brightly emitting functional components. This could be achieved by taking advantage of the PAA layer at the CdS nanoparticles surface, in order to coat the CdS core with a shell of higher-bandgap material such as ZnS, to minimize "trapped" electron-hole pairs. In addition, our preliminary work on these QDs as Cd^{2+}-selective sensors has shown that the activation effect is not indiscriminate; nonetheless, a more detailed systematic study is required to determine which metal ions are capable of inducing PL surface activation in the present system, and whether activation effects can be used to identify the presence of specific ions (e.g. Cd^{2+}). It is also important to note that the present block copolymer template method for nanoparticle synthesis is by no means limited to CdS, which has been explored in this thesis as an appropriate model system. The versatility of this method should allow a wide range of metal and semiconducting nanoparticles, with interesting optical, electronic and magnetic properties, to be incorporated and combined into polymeric nanocomposites in a controlled manner.

In the next chapter, we extend this work to the self-assembly of these well-characterized CdS QDs, in order to obtain various surface patterns with structural hierarchy on glass via spontaneous polymer/polymer phase separation.

2.5. References

(1) Murray, C. B.; Norris, D. J.; Bawendi, M. G. *J. Am. Chem. Soc.* **1993**, *115*, 8706.

(2) Lee, J.; Sundar, V. C.; Heine, J. R.; Bawendi, M. G.; Jensen, K. F. *Adv. Mater.* **2000**, *12*, 1102.

(3) Hirai, T.; Watanabe, T.; Komasawa, I. *J. Phys. Chem B* **2000**, *104*, 8962.

(4) Pavel, F. M.; Mackay, R. A. *Langmuir* **2000**, *16*, 8568.

(5) Zhang, H.; Cui, Z.; Wang, Y.; Zhang, K.; Ji, X.; Lu, C.; Yang, B.; Gao, M. *Adv. Mater.* **2003**, *15*, 777.

(6) Petruska, M. A.; Bartko, A. P.; Klimov, V. I. *J. Am. Chem. Soc.* **2004**, *126*, 714.

(7) Lemon, B. I.; Crooks, R. M. *J. Am. Chem. Soc.* **2000**, *122*, 12886.

(8) Guo, W.; Li, J. J.; Wang, A.; Peng, X. *J. Am. Chem. Soc.* **2003**, *125*, 3901.

(9) Carrot, G.; Scholz, S. M.; Plummer, C. J. G.; Hilborn, J. G.; Hendrick, J. L. C. M., 11, 3571. *Chem. Mater.* **1999**, *11*, 3571.

(10) Erskine, L. L.; Emrick, T.; A.P., A.; J.M.J., F. In *Abstr. Pap. Am. Chem. Soc.*, Mar 26, 2000; pp 219:387-POLY Part 212.

(11) Skaff, H.; Ilker, M. F.; Coughlin, E. B.; Emrick, T. *J. Am. Chem. Soc.* **2002**, *124*, 5729.

(12) Skaff, H.; Emrick, T. *Chem. Comm.* **2003**, *52*.

(13) Potapova, I.; Mruk, R.; Prehl, S.; Zentel, R.; Basche, T.; Mews, A. J. *J. Am. Chem. Soc.* **2003**, *125*, 320.

(14) Corbierre, M. K.; Cameron, N. S.; Sutton, M.; Mochrie, S. G. J.; Lurio, L. B.; Ruhm, A.; Lennox, R. B. *J. Am. Chem. Soc.* **2001**, *123*, 10411.

(15) Spatz, J. P.; Herzog, T.; Mossmer, S.; Ziemann, P.; Moller, M. *Adv. Mater.* **1999**, *11*, 149.

(16) Sooklal, K.; Hanus, L. H.; Ploehn, H. J.; Murphy, C. J. *Adv. Mater.* **1998**, *10*, 1083.

(17) Huang, J.; Sooklal, K.; Murphy, C. J.; Ploehn, H. J. *Chem. Mater.* **1999**, *11*, 3595.

(18) Moller, M.; Kunstle, H.; Kunz, M. *Synth. Met.* **1991**, *41-43*, 1159.

(19) Cummins, C. C.; Schrock, R. R.; Cohen, R. E. *Chem. Mater.* **1992**, *4*, 27.

(20) Moffitt, M.; McMahon, L.; Pessel, V.; Eisenberg, A. *Chem. Mater.* **1995**, *7*, 1185.

(21) Moller, M.; Spatz, J. P. *Curr. Opin. Coll. Interfac. Sci.* **1997**, *2*, 177.

(22) Forster, S.; Antonietti, M. *Adv. Mater.* **1998**, *10*, 195.

(23) Cohen, R. E. *Curr. Opin. Solid State Mater. Sci.* **1999**, *4*, 587.

(24) Wang, D.; Cao, Y.; Zhang, X.; Liu, Z.; Qian, X.; Ai, X.; Liu, F.; Wang, D.; Bai, Y.; Li, T.; Tang, X. *Chem. Mater.* **1999**, *11*, 392.

(25) Underhill, R. S.; Liu, G. *Chem. Mater.* **2000**, *12*, 2082.

(26) Qi, L.; Colfen, H.; Antonietti, M. *Nano lett.* **2001**, *1*, 61.

(27) Zhao, H.; Douglas, E. P.; Harrison, B. S.; Schanze, K. S. *Langmuir* **2001**, *17*, 8428.

(28) Zhao, H.; Douglas, E. P. *Chem. Mater.* **2002**, *14*, 1418.

(29) Yang, C.-S.; Awschalom, D. D.; Stucky, G. D. *Chem. Mater.* **2002**, *14*, 1277.

(30) Zhang, M.; Drechsler, M.; Muller, A. H. E. *Chem. Mater.* **2004**, *16*, 537.

(31) Moffitt, M. *Ph.D. Thesis*; McGill University, 1997.

(32) Kim, S.; Bawendi, M. G. *J. Am. Chem. Soc.* **2003**, *125*, 14652.

(33) Henglein, A. *Chem. Rev.* **1989**, *89*, 1861.

(34) Ni, T.; Nagesha, D. K.; Robles, J.; Materer, N. F.; Mussig, S.; Kotov, N. A. *J. Am. Chem. Soc.* **2002**, *124*, 3980.

(35) Herron, N.; Wang, Y.; Eckert, H. *J. Am. Chem. Soc.* **1990**, *112*, 1322.

(36) Dannhauser, T.; O'Neil, M.; Johansson, K.; Whitten, D.; McLendon, G. *J. Phys. Chem.* **1986**, *90*, 6074.

(37) Spanhel, L.; Haase, M.; Weller, H.; Henglein, A. *J. Am. Chem. Soc.* **1987**, *109*, 5649.

(38) Resch, U.; Eychmuller, A.; Haase, M.; Weller, H. *Langmuir* **1992**, *8*, 2215.

(39) Hao, E.; Sun, H.; Zhou, Z.; Liu, J.; Yang, B.; Shen, J. *Chem. Mater.* **1999**, *11*, 3096.

(40) Wu, F.; Zhang, J. Z.; Kho, R.; Mehra, R. K. *Chem. Phys. Lett.* **2000**, *330*, 237.

(41) Zhang, J.; Sun, L.; Liao, C.; Yan, C. *Solid State Comm.* **2002**, *124*, 45.

(42) Myung, N.; Bae, Y.; Bard, A. J. *Nano lett.* **2003**, *3*, 747.

(43) Wankhede, M. E.; Haram, S. K. *Chem. Mater.* **2003**, *15*, 1296.

(44) Mahtab, R.; Rogers, J., P.; Murphy, C. J. *J. Am. Chem. Soc.* **1995**, *117*, 9099.

(45) Lakowicz, J. R.; Gryczynski, I.; Gryczynski, Z.; Nowaczyk, K.; Murphy, C. J. *Anal. Biochem.* **2000**, *280*, 128.

(46) Tian, Y.; Fendler, J. H. *Chem. Mater.* **1996**, *8*, 969.

(47) Moore, D. E.; Patel, K. *Langmuir* **2001**, *17*, 2541.

(48) Li, X.; Coffer, J. L. *Chem. Mater.* **1999**, *11*, 2326.

(49) Hamity, M.; Lema, R. H.; Suchetti, C. A. *J. Photochem, Photobio. A* **2000**, *133*, 205.

(50) Hamity, M.; Lema, R. H.; Suchetti, C. A. *J. Photochem, Photobio. A* **1998**, *115*, 163.

(51) Hautekeer, J. P.; Varshney, S. K.; Fayt, R.; Jacobs, C.; Jerome, R.; Teyssie, P. *Macromolecules* **1990**, *23*, 3893.

(52) Zhong, X. F.; Varshney, S. K.; Eisenberg, A. *Macromolecules* **1992**, *25*, 7160.

(53) Dawson, W. R.; Windsor, M. W. *J. Phys. Chem.* **1968**, *72*, 3251.

(54) Nguyen, D. *Ph.D. Thesis*; McGill University, 1994.

(55) Murray, C. B.; Kagan, C. R.; Bawendi, M. G. *Annu. Rev. Mater. Sci.* **2000**, *30*, 545.

(56) Alivisatos, A. P. *J. Phys. Chem.* **1996**, *100*, 13226.

(57) Weller, H. *Angew. Chem., Int. Ed. Engl.* **1993**, *32*, 41.

(58) Steigerwald, M. L.; Brus, L. E. *Acc. Chem. Res.* **1990**, *23*, 183.

(59) Joo, J.; Na, H. B.; Yu, T.; Yu, J. H.; Kim, Y. W.; Wu, F.; Zhang, J. Z.; Hyeon, T. *J. Am. Chem. Soc.* **2003**, *125*, 11100.

(60) Chen, Y.; Rosenzweig, Z. *Anal. Chem.* **2002**, *74*, 5132.

(61) Wang, X.; Qu, L. Z., J.; Peng, X.; Xiao, M. *Nano lett.* **2003**, *3*, 1103.

(62) Wuister, S. F.; Swart, I.; van Driel, F.; Hickey, S. G.; de Mello Donega, C. *Nano lett.* **2003**, *3*, 503.

(63) We point out that these average lifetimes were obtained using a total of 1000 counts; we acknowledge that this is not ideal, although unfortunately, extremely long collection times (up to 8 hours for 1000 counts) made collecting 10000 counts prohibitive for these samples. We point out that we are only fitting our data over two decades of time, and from Table 2.2 it is clear that good fits are

obtained in this region. As well, we are only reporting average lifetimes from the fits and these values are quite reproducible for repeat measurements, with errors of ~2 % for most samples, despite somewhat non-ideal total counts.

(64) Derfus, A. M.; Chan, W. C. W.; Bhatia, S. N. *Nano lett.* **2004**, *4*, 11.

(65) Desjardins, A.; van de Ven, T. G. M.; Eisenberg, A. *Macromolecules* **1992**, *25*, 2412.

(66) Peng, X.; Schlamp, M. C.; Kadavanich, A. V.; Alivisatos, A. P. *J. Am. Chem. Soc.* **1997**, *119*, 7019.

(67) Moffitt, M.; Eisenberg, A. *Macromolecules* **1997**, *30*, 4363.

CHAPTER 3

NONLITHOGRAPHIC HIERARCHICAL PATTERNING OF SEMICONDUCTING NANOPARTICLES VIA POLYMER/POLYMER PHASE SEPARATION

3.1. Introduction

Colloidal semiconducting nanoparticles, or quantum dots (QDs), have been recognized as promising building blocks for a new generation of photonic and electronic devices, due to their unique and size-dependent properties arising from quantum confinement and surface effects. Essential to the production of devices and materials with specific function will be the organization of QDs on solid substrates into ordered patterns with well-defined length scales. Lithographic approaches to patterning QDs require the initial pattern to be generated from the top down using, for example, photolithography or electron beam lithography.[1-4] In contrast, nonlithographic techniques harnessing spontaneous processes such as dewetting and phase separation offer immense promise for the fast and efficient self-assembly of QDs into regular patterns over large areas. The drying-mediated self-assembly of colloidal nanoparticles deposited from volatile solvents onto various substrates has been found to yield a wide range of surface patterns, including cellular and bicontinuous networks, and arrays of nanoparticle aggregates with strong spatial correlation.[5-12]

Many future materials and devices based on QDs will require their incorporation and organization in polymer environments. Microphase separated block copolymers have been used to template the organization of QDs, demonstrating excellent control over the spatial distribution of QDs on the length scale of tens of nanometers.[13-17] However, an essential feature of patterning using block copolymers is the inherent connectivity of the phase-separating blocks, which restricts feature sizes to the dimensions of the polymer chains. With the growing need for photonic materials and devices, self-assembly

strategies resulting in hierarchical polymer/QD structures with features on micron or just under micron length scales, on the order of optical wavelengths, will be required.[18,19]

Phase separation of immiscible homopolymer mixtures by casting from a common solvent is a well-established method of forming micrometer surface patterns of two or more polymers on a solid substrate.[20-24] As the solvent evaporates, composition waves develop by spinodal decomposition, giving rise to various patterns of phase separated polymer domains, with characteristic correlation lengths that depend on the extent of coarsening.[25-27] Lateral patterns formed in this way tend to be isotropic, although non-isotropic structures can be replicated by a combination of polymer/polymer phase separation and selective wetting on a pre-patterned substrate.[28,29]

To our knowledge, only one previous study has used polymer/polymer phase separation to direct the assembly of inorganic nanoparticles on a solid substrate.[30] In that work, Amis and co-workers employed a two-step process in which a poly(DL-lactide)/poly(ε-caprolactone) blend was first spin-cast onto silicon, after which dendrimer-coated cadmium sulfide (CdS) QDs were exposed to the phase-separated film, resulting in selective adhesion of QDs to the surface of the more hydrophilic poly(DL-lactide) domains.[30] Here, we present a new, one-step strategy for the patterning of semiconducting nanoparticles in polymer films, in which QD self-assembly occurs as a result of concurrent phase separation between a polymer joined to the QD surface and an immiscible homopolymer component (Figure 3.1), resulting in hierarchical structures with QD organization on two length scales.

CdS QDs stabilized by a polystyrene-*b*-poly(cadmium acrylate) (PS-*b*-PACd) block copolymer layer have been synthesized and extensively characterized as described

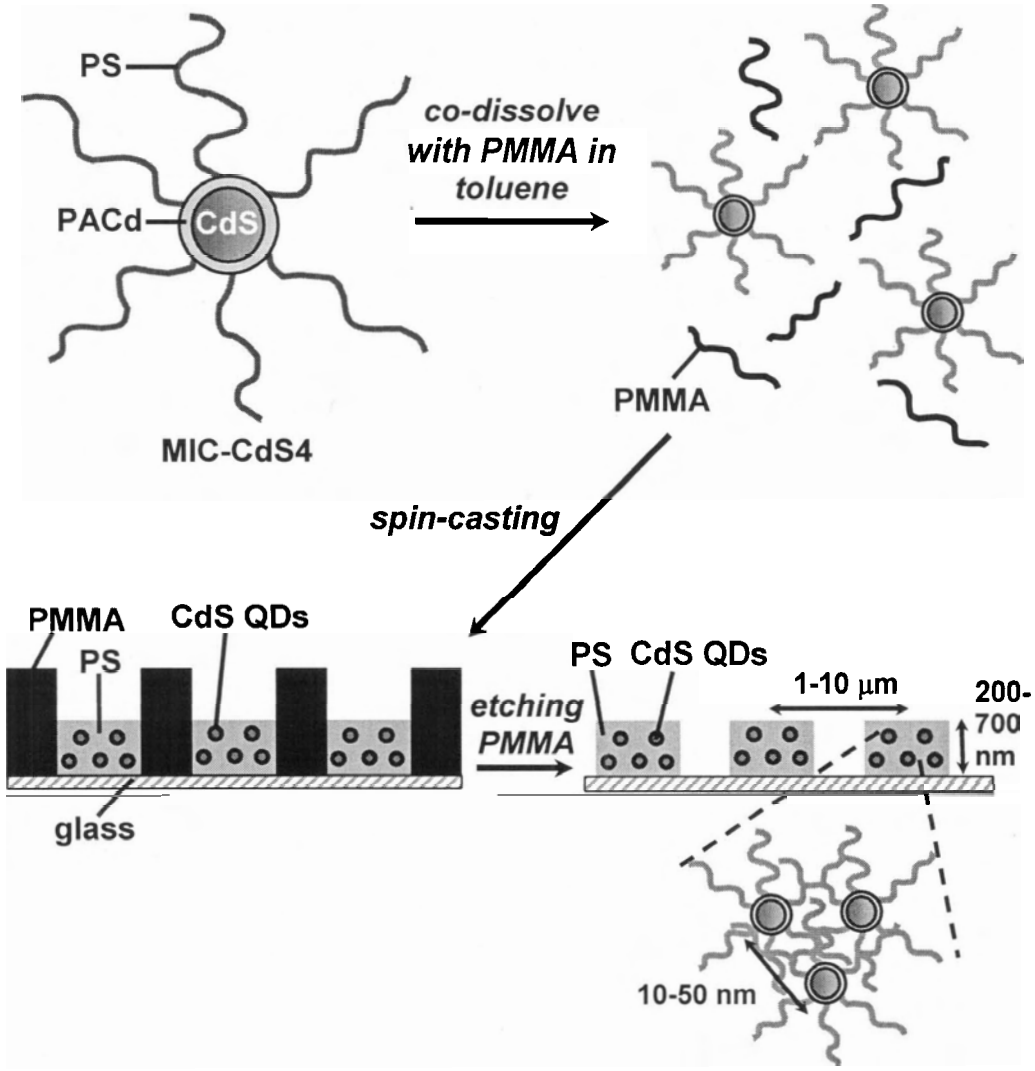

Figure 3.1. Schematic showing block copolymer-stabilized CdS QD (MIC-CdS4), and method of patterning by spin-casting MIC-CdS4/PMMA blends from toluene solutions followed by selective etching of the PMMA domains. The final MIC-CdS4 features show organization on two disparate length scales, as described in the text.

in the previous chapter.[31,32] These stable building blocks are protected by an outer PS brush layer, which governs the interactions of QDs with the surrounding medium, making them soluble in good solvents for PS and completely miscible in PS homopolymer; strong ionic interactions in the PACd layer serve as cross-links, locking the block copolymer chains into the brush at the QD surface, even with the removal of solvent.[31,32] In this work, we take advantage of the "PS-like" behaviour of these stabilized nanoparticles to induce QD self-assembly via phase separation from an immiscible poly(methyl methacrylate) (PMMA) homopolymer, using simple spin-casting of blend components onto glass substrates. A unique feature of this strategy is the use of a single, fast spin-casting step to effect controllable organization of QDs on two disparate length scales in a polymer film: 1) micron-scale ordering governed by polymer/polymer phase separation and 2) nano-scale ordering governed by steric interactions between polymer brush-coated QDs.

3.2. Experimental

3.2.1. Preparation of QD Blend Films

The block copolymer-stabilized CdS QD sample used in this work is MIC-CdS4, which is described in the previous chapter. Blends of MIC-CdS4 and PMMA homopolymer (Aldrich, M_w = 120,000 g/mol) were prepared by dissolving appropriate quantities of each component individually in spectroscopic grade toluene to a polymer concentration of 6 wt %. The stock solutions were stirred for ~4h and allowed to equilibrate overnight in the dark. 6 wt % blend solutions of the desired composition were prepared by filtering measured amounts of each solution through two membrane filters

(0.45 μm nominal pore size) connected in series into a glass sample vial. Three compositions of the polymer blend solutions were made in this manner: MIC-CdS4/PMMA (w/w) = 50/50, 30/70 and 10/90.

The blend films were made by spin-casting one drop of the blend solution onto clean 18 x 18 mm glass coverslips at different rotation speeds (3000, 6000 and 9000 rpm) for one minute. Before spin-casting, the glass substrates were cleaned by 10 min sonication in chloroform, followed by 10 min sonication in methanol, then overnight drying under vaccum. To test reproducibility, several films were prepared for each composition and speed of rotation. Before imaging, all films were placed in a vacuum oven and dried overnight under active vacuum at room temperature to remove any residual solvent.

Selective removal of the PMMA phase (etching) was carried out by placing the films in a Petri dish containing acetone and a stir bar and stirring for 4-5 min. The films were then removed and further rinsed with acetone, before air drying for 3-4 hours followed by drying under active vacuum at RT overnight. Spin-cast MIC-CdS4/PMMA films were mainly transparent in appearance before etching, but became markedly turbid after etching.

3.2.2. Atomic Force Microscopy (AFM)

All AFM images were obtained using a Veeco (ThermoMicroscopes Explore) Instrument equipped with a Veeco tip (Nanoprobe-MLCT-EXMT-A) and operating in contact mode. To minimize the effect of vibrations, the AFM probe was covered with a vibration-resistant case on a vibration isolation platform maintained at 80 psi. Each

sample was imaged several times at different locations on the substrate to determine the regularity of patterning. In some cases, brightness, contrast, and contour levels of AFM were adjusted to improve clarity for presentation.

3.2.3. Laser Scanning Confocal Fluorescence Microscopy (LSCFM)

Laser scanning confocal fluorescence microscopy measurements were carried out on a Zeiss LSM 410 equipped with an Ar/Kr laser. All films were excited at ~488 nm, using a bandpass 485 ± 20 nm line selection filter and a FT 510 dichroic beam splitter. A longpass 515 emission filter was used such that only light above 515 nm reached the PMT. A pinhole diameter 1.31 Airy Units was used for all measurements, resulting in an optical section thickness of 0.75 μm FWHM.

3.2.4. Transmission Electron Microscopy (TEM)

Transmission electron microscopy was performed on a Hitachi H-700 electron microscope, operating at an accelerating voltage of 70 kV. Selected spin-cast CdS/PMMA films, before and after etching, were embedded in an Epon resin, and then ~60 nm thick sections were produced with a diamond knife on Reichert UltraCut E ultra-microtone. The thin sections were placed on carbon/formvar-coated 300 mesh copper grids for imaging.

3.3. Results and Discussion

3.3.1. Micron-Scale PS/QD Patterns on Glass Substrates

The synthesis and characterization of the block copolymer-stabilized QD sample

employed in this work was described in the previous chapter.[31,32] The sample used was MIC-CdS4 (Figure 3.1), and consists of CdS QDs with average diameter 5.4 nm (determined from the UV-vis absorption onset), protected by an ionically-crosslinked surface layer of PACd blocks and an outer brush layer of hydrophobic PS blocks with an average length of 330 styrene repeat units. From light scattering measurements and assuming that no QD aggregates formed in solution, it was estimated that each MIC-CdS4 particle is decorated with an average of 430 PS chains, giving a brush density of ~ 1 PS chain/nm^2 on the surface of the particles.[32] The photoluminescence (PL) spectrum of MIC-CdS4 in toluene solution revealed two emission bands, a sharp band-edge emission at 469 nm and a broad trap-state emission centered at 622 nm.[31]

To produce patterned polymer/QD films, various blend solutions of MIC-CdS4 and PMMA homopolymer in toluene (total concentration = 6 wt %) were spin-cast onto glass substrates (Figure 3.1). MIC-CdS4 and PMMA are both completely soluble in toluene and form a single transparent phase in solution; however, as the solvent evaporates during spin-casting, the immiscibility of the outer PS layer surrounding MIC-CdS4 and the PMMA homopolymer leads to phase separation, resulting in self-assembly of polymer-coated QDs. For 50/50 (w/w) MIC-CdS4/PMMA blends, spin-casting was carried out at rotation speeds of 3000, 6000 and 9000 rpm, giving films ranging from 250 to 650 nm in thickness, with thicker films resulting from slower rotation speeds. The surface morphologies of the resulting films were determined by atomic force microscopy (AFM) in contact mode, revealing spontaneous patterning arising from spin-casting. The AFM image of the 3000 rpm film (Figure 3.2a) shows a clear bicontinuous structure of raised (light) and lower (dark) domains, while the 9000 rpm film shows a similar lateral

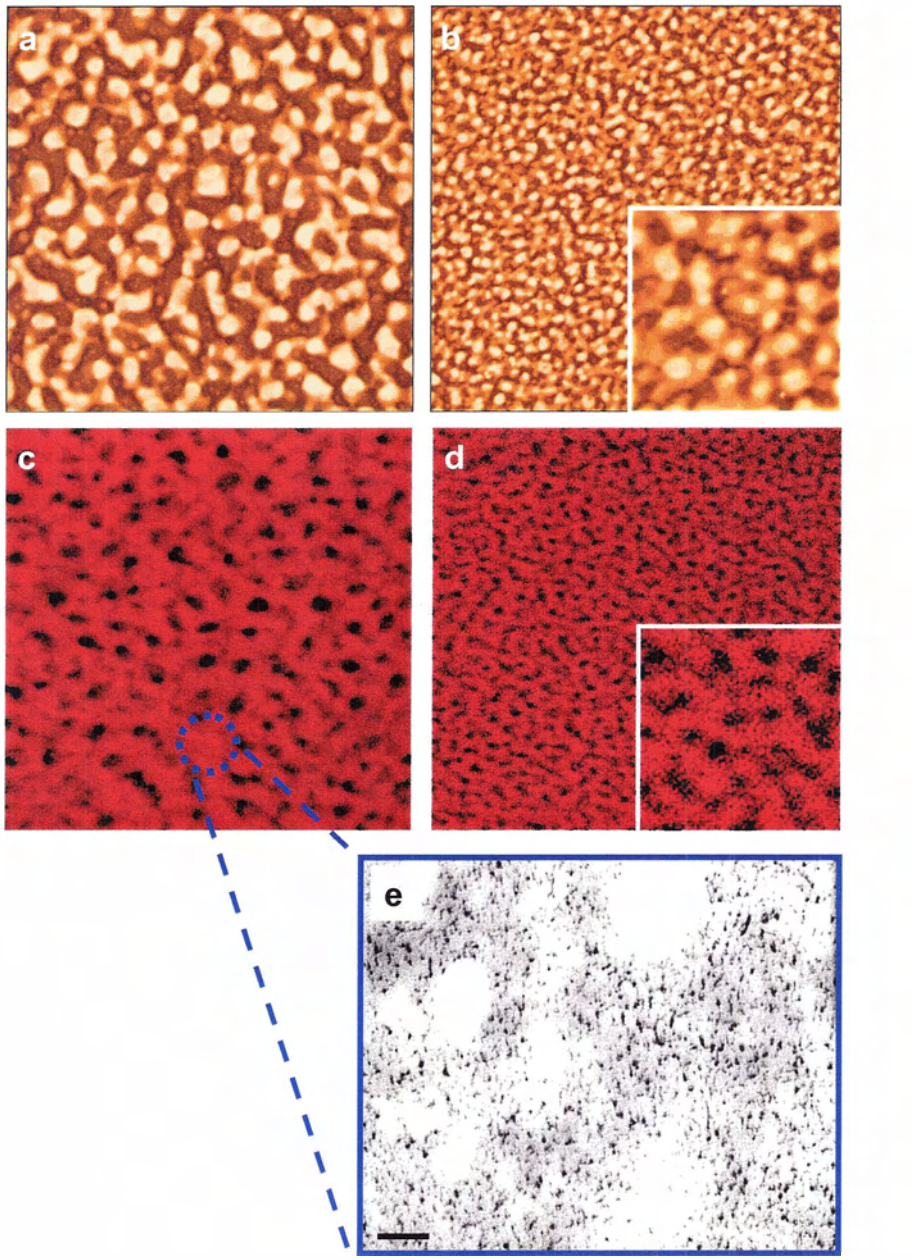

Figure 3.2. AFM (a, b) and LSCFM (c,d) images of spin-cast 50/50 (w/w) MIC-CdS4/PMMA blend films, prepared using rotation speeds of 3000 rpm (a,c) and 9000 rpm (b,d). All AFM and LSCFM images have edge lengths of 50 μm; the insets have edge lengths of 10 μm, and show enlarged regions of the 9000 rpm film from images in b and d. TEM image (e) of the 3000 rpm blend, showing the nano-scale organization of QDs within the MIC-CdS4 domains; the scale bar in the TEM image represents 100 nm.

pattern (Figure 3.2b, inset) but on a smaller length scale; the 6000 rpm film (not shown) revealed the same bicontinuous domain structure, with feature sizes between those of the 3000 and 9000 rpm films. Smaller lateral feature sizes for faster rotation speeds can be explained by a faster rate of solvent evaporation, which results in the blend films being kinetically trapped at earlier stages of domain coarsening. The combination of bicontinuous domain structure and structural self-similarity for different stages of phase coarsening strongly suggests that lateral patterning occurs by a mechanism of spinodal decomposition between immiscible MIC-CdS4 and PMMA components.[27] Along with the observed lateral features, AFM indicates that the blend films exhibit a topology coinciding with the domain structure, in which one phase protrudes above the other at the film surface; a similar phenomenon has been observed previously in more conventional blends of PS and PMMA homopolymers spin-cast from toluene,[20,21] and was attributed to the preferential solubility of PS in toluene relative to PMMA.[21] In the present case, the MIC-CdS4 phase will be more highly swollen with toluene than the PMMA phase as the lateral domain structure develops, eventually collapsing below the level of the PMMA domains when the last of the solvent evaporates (Figure 3.1). From AFM surface morphologies in Figures 3.2a and 3.2b, therefore, we infer that the raised features are comprised of PMMA, and the lower features consist of self-assembled MIC-CdS4 QDs, as portrayed in Figure 3.1.

More direct evidence of lateral QD patterning comes from laser scanning confocal fluorescence microscopy (LSCFM) of the blend films, in which contrast is provided by PL from the CdS QDs; all LSCFM images were obtained by excitation of the CdS QDs at 488 nm and collection of light from the red-shifted trap-state emission (> 515 nm).

LSCFM images of the 3000 and 9000 rpm films (Figures 3.2c and 3.2d, respectively) show regular patterns of photoluminescent PS/QD domains (red regions) with feature sizes corresponding to the AFM images, along with analogous self-similarity at different rotation speeds (Figure 3.2d, inset); this suggests that the self-assembly and patterning of MIC-CdS4 is a result of the same polymer/polymer spinodal decomposition process responsible for the surface morphologies observed by AFM. Despite similarities in the structural information obtained by AFM and LSCFM, we note that AFM probes the topology of the films, whereas LSCFM images the films below the surface. An apparent consequence of this difference in the two imaging techniques is that AFM shows a laterally continuous PMMA phase (light regions, Figures 3.2a and 3.2b), whereas the PMMA domain structure is non-continuous in the LSCFM images (dark regions, Figures 3.2c and 3.2d); this suggests that the protruding PMMA features at the film surface occupy a larger fraction of the in-place area than the non-protruding PMMA domains underneath.

Due to the effects of fast solvent evaporation, PS/QD patterns obtained by spin-casting are not in thermodynamic equilibrium, although they are stable, kinetically "frozen" structures, well below the glass transition temperatures of both polymer components in the absence of solvent. We have seen that the kinetic nature of these patterns allows the length scale of QD organization to be easily tuned via the spin-casting speed of rotation. To better characterize the order and characteristic correlation lengths of PS/QDs patterns obtained at different rotation speeds, two-dimensional fast Fourier transforms (2D-FFT) of binarized LSCFM images of the various films were obtained. Radial averages of 2D-FFT images yield plots of intensity $I(q)$ vs. scattering vector q,

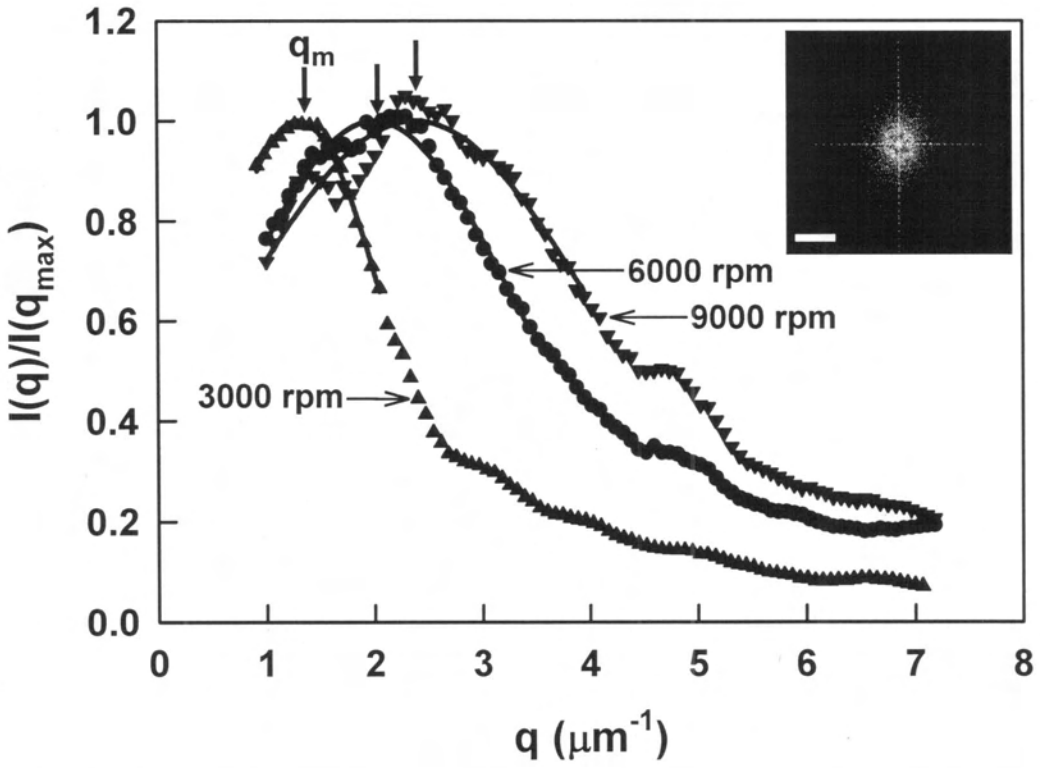

Figure 3.3. Plots of normalized intensity $I(q)/I(q_m)$ vs. scattering vector q, from radially-averaged 2D-FFT of LSCFM images of 50/50 (w/w) MIC-CdS4/PMMA blends, prepared using rotation speeds of 3000, 6000, and 9000 rpm. The solid lines show a simple Gaussian fit of the resulting peaks and arrows indicate the peak maxima q_m; the peak positions are found to shift to higher q values with increasing rotation speed, demonstrating tunability of the correlation lengths of the patterns. The inset shows a sample 2D-FFT of the LSCFM image in Figure 3.2c (3000 rpm film); the scale bar represents 5 μm^{-1}.

which are equivalent to 2D structure factors. 2D-FFT of LSCFM images of 50/50 MIC-CdS4/PMMA films obtained at 3000, 6000, and 9000 rpm each show a ring (e.g. Figure 3.3, inset), or a peak in the resulting radial average, indicating MIC-CdS4 organization with well-defined correlation lengths. From the normalized radial averages, $I(q)/I(q_m)$ vs. q (Figure 3.3), it is clear that the peak position shifts to higher q values with increasing speed of rotation. Simple Gaussian fits of each of these plots were used to determine the peak positions q_m, from which a characteristic correlation length, $\Lambda_m = 2\pi/q_m$, was obtained for each lateral pattern, giving $\Lambda_m = 4.8$, 3.1, and 2.6 μm for the 3000, 6000, and 9000 rpm films, respectively. These values agree well with estimated average feature spacings from LSCFM images of the patterned films (Figures 3.2c and 3.2d).

3.3.2. Nano-scale Spatial Distribution of QDs Within PS/QD Features

To determine the specific organization of QDs within the PS/QD domains, microtomed sections of the spin-cast films were obtained and mounted on grids for transmission electron microscopy (TEM). For the 50/50 MIC-CdS4/PMMA film (3000 rpm), TEM (Figure 3.2e) clearly shows the nano-scale spatial distribution of QDs within the PS matrix of the MIC-CdS4 phase, highlighting the structural hierarchy in these films. No long-range order of QDs is discernable, though the inorganic nanoparticles are well dispersed and quite evenly spaced, suggesting that QDs are spatially distributed in a liquid-like fashion. While the micron-scale ordering observed by AFM and LSCFM is a result of polymer/polymer spinodal decomposition, the nano-scale liquid-like ordering of QDs can be attributed to interactions between PS brush-stabilized nanoparticles within

the solvent-swollen MIC-CdS4 phase as the toluene evaporates. Importantly, both levels of organization arise from a single process of solvent evaporation. The ordering of block copolymer micelles at increasing concentrations has been characterized by McConnell and Gast,[33] who found that micelles formed long-range cubic crystals above a critical ordering concentration, but then melted to a less ordered liquid-like state at even higher concentrations; this melting transition was explained by overlap between the brush layers of neighboring micelles, which resulted in a loss of the osmotic pressure gradient within the brushes and a consequential loss of the repulsive interparticle force. A similar evolution of nanoparticle organization in the MIC-CdS4 phase is envisioned in the present case, where the PS brush layers surrounding self-assembling QDs eventually form the PS matrix observed in Figure 3.2e upon evaporation of solvent. From the measured MIC-CdS4 aggregation number in toluene and the bulk PS density, the average spacing between CdS QDs is calculated to be 30 nm; this value seems reasonable based on Figure 3.2e, but is unfortunately difficult to confirm from the obtained microtomed sections, which are not monolayers and therefore represent a superposition of several layers of nanoparticles in the plane of the image. Along with the spatial distribution of QDs, TEM also shows a second population of smaller (100-200 nm) PMMA domains (white regions in Figure 3.2e), dispersed throughout the MIC-CdS4 phase, which was not visible by LSCFM. These smaller PMMA droplets may be related to the presence of a small amount of free polystyrene-*b*-polyacrylic acid (PS-*b*-PAA) from the MIC-CdS4 sample, which could localize at the droplet interface resulting in interfacial stabilization and a slower rate of coarsening compared to the larger PMMA features.

3.3.3. Effect of Blend Composition on PS/QD Pattern Morphology

While variation in the spin-casting speed of rotation allowed pattern feature sizes to be easily tuned, different types of PS/QD patterns could be obtained by varying the blend composition. Figure 3.4 shows AFM and LSCFM images of films obtained at 3000 rpm with the following MIC-CdS4/PMMA (w/w) ratios: 50/50 (Figures 3.4a and 3.4b), 30/70 (Figures 3.4c and 3.4d), and 10/90 (Figures 3.4e and 3.4f), revealing a range of nanoparticle patterns, each extending over large areas. As seen previously, AFM reveals a raised PMMA surface layer which approximately coincides with the sub-surface MIC-CdS4/PMMA morphology determined by LSCFM. 2D-FFT of LSCFM images for the three compositions each resulted in a ring (not shown), indicating well-defined correlation lengths for all of the micron-scale patterns. With decreasing MIC-CdS4 content, the resulting patterns vary from a cellular or foam-like network (50/50, Figure 3.4b), to a network of MIC-CdS4 wires (Figure 3.4d), to an array of MIC-CdS4 islands (Figure 3.4f). The strong spatial correlation of the islands is indicated by their organization into strings (Figures 3.4e and 3.4f, insets), attributed to a spinodal decomposition pathway for pattern formation, in which a continuous network breaks into discrete domains during coarsening.[26]

3.3.4. Selective Removal of PMMA: PS/QDs Features With Structural Hierarchy

Finally, we demonstrated that the PMMA component of these films could be selectively removed by etching with acetone, a good solvent for PMMA but a poor solvent for PS, leaving behind MIC-CdS4 features with structural hierarchy patterned on

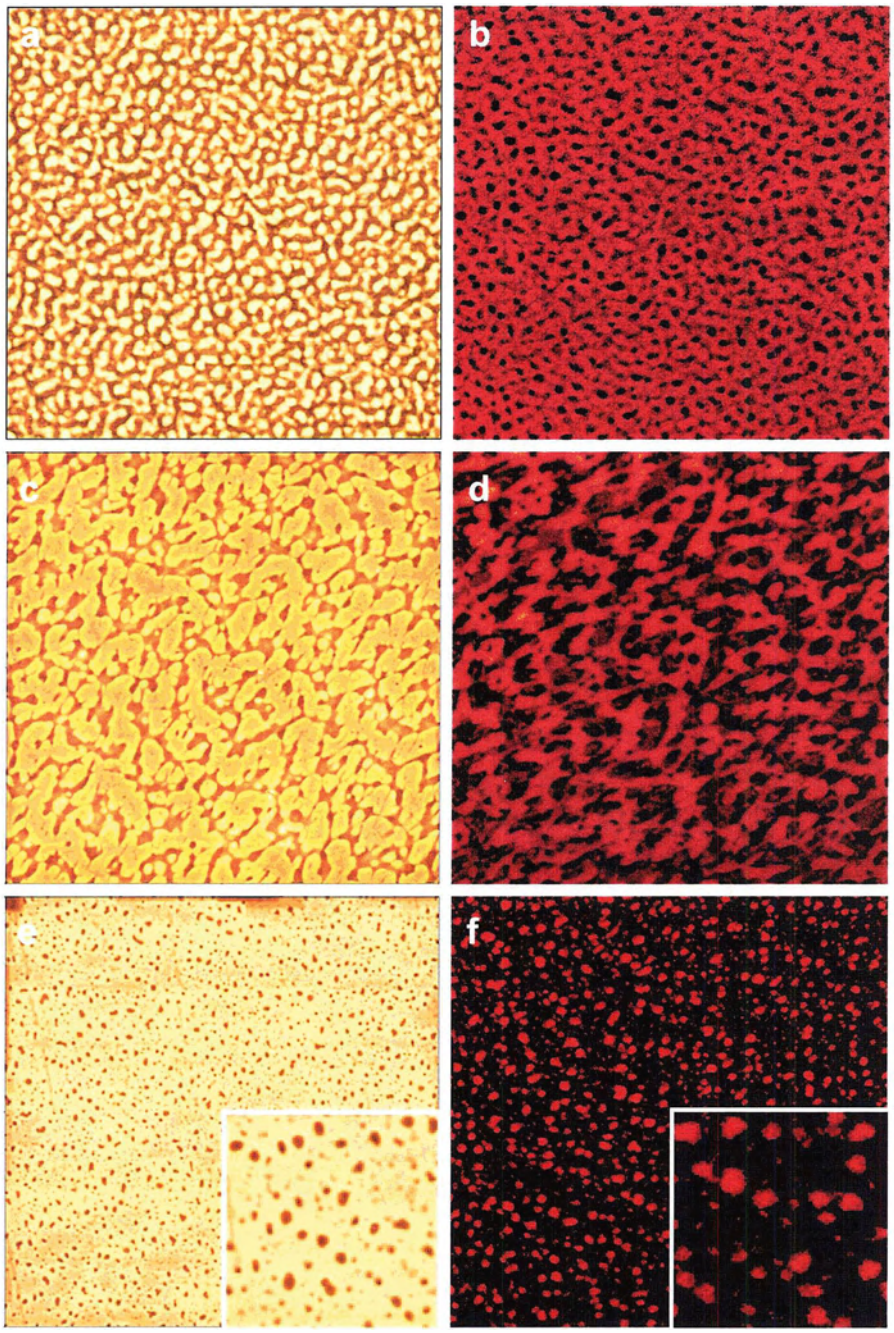

Figure 3.4. AFM (a,c,e) and LSCFM (b,d,f) images of spin-cast films for various blend compositions: MIC-CdS4/PMMA (w/w) = 50/50 (a,b); MIC-CdS4/PMMA (w/w) = 30/70 (c,d); and MIC-CdS4/PMMA (w/w) = 10/90 (e,f); the edge length of all images is 100 μm. For all blend compositions, the rotation speed for spin-casting was 3000 rpm. Insets (edge length = 20 μm) show enlarged regions of the 10/90 sample from images in e and f.

glass, as depicted in Figure 3.1. Figure 3.5 shows two-dimensional (2D) and three-dimensional (3D) representations of AFM images for the 3000 rpm films obtained from different blend compositions, following selective dissolution of the PMMA phase. Compared with the same films before etching (Figure 3.4), AFM shows the lateral MIC-CdS4 domain morphologies to be well preserved, although the film topologies are completely changed by removal of PMMA, with raised regions representing the laterally patterned MIC-CdS4 features and low regions representing the glass substrate in the etched films (Figure 3.5). Some of the resulting surface structures are particularly interesting, including a continuous network of MIC-CdS4 wires on glass (Figures 3.5c and 3.5d) with average wire thickness of 1.5 ± 0.5 μm and average height of 370 ± 60 nm, and an array of spatially-correlated MIC-CdS4 islands (Figures 3.5e and 3.5f), with average island diameter of 2.0 ± 0.4 μm and average height of 410 ± 70 nm. Along with the lateral organization visible by AFM, all of the surface features in Figure 3.5 possess an internal structure of QDs dispersed in a liquid-like fashion, similar to that shown in Figure 3.2e; from the measured average dimensions of the islands in Figure 3.5f, and assuming cylindrical geometry, we calculate that each PS/QD island contains an average of 5.1×10^4 QDs. Importantly, both the lateral dimensions and heights of these features can be tuned via the speed of rotation, choice of solvent, or concentration of the blend solution, offering the potential for making a range of structures with dimensions commensurate with specific applications (e.g. optical wavelengths). For example, by varying the rotation speed from 3000 to 9000 rpm, the average feature height in the etched 50/50 blend films was reduced from 500 ± 90 nm to 200 ± 40 nm. In addition, by

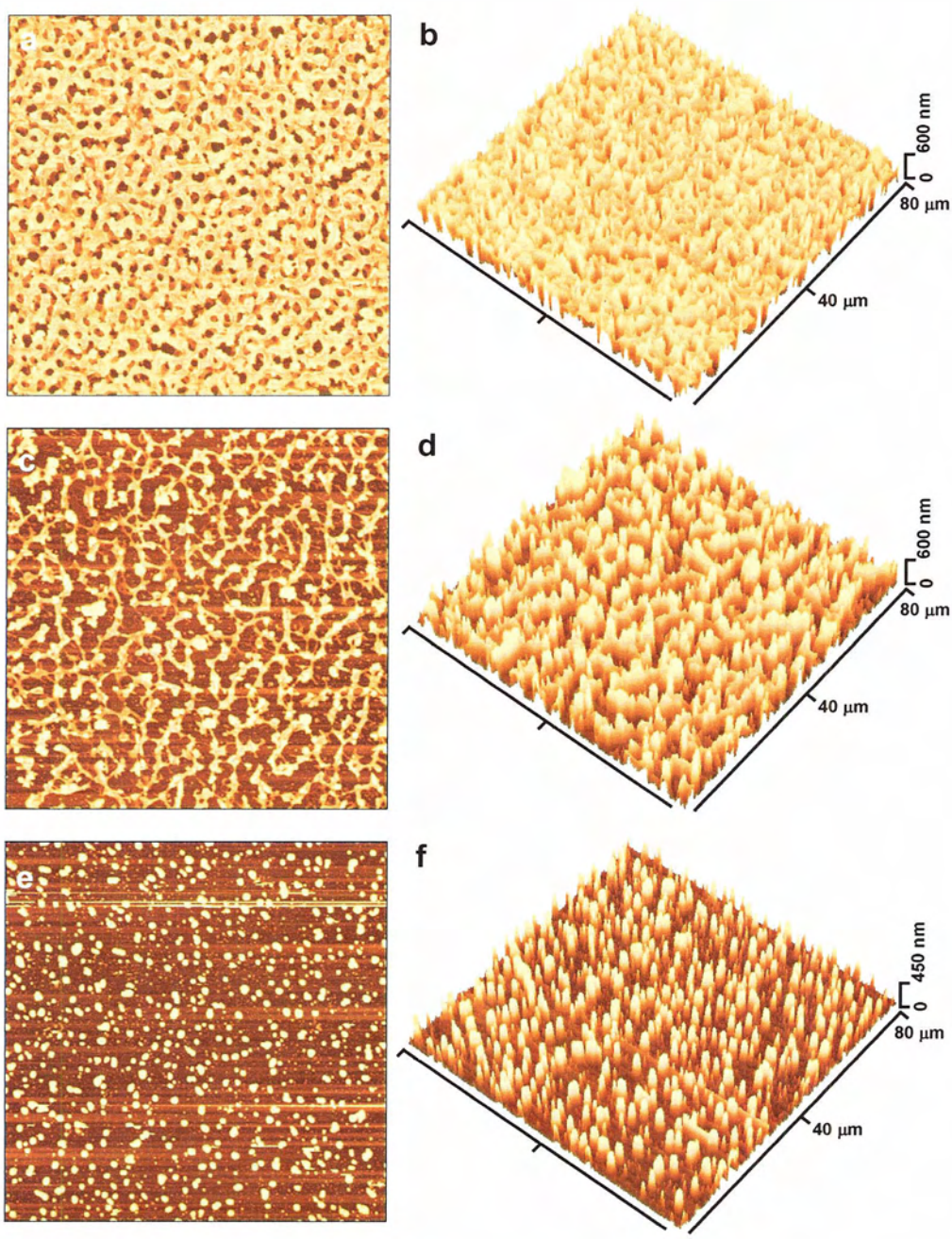

Figure 3.5. 2D (a, c, e) and 3D (b, d, f) AFM images of the spin-cast films shown in Figure 3.4 after selective removal of the PMMA phase by etching with acetone: MIC-CdS4/PMMA (w/w) = 50/50 (a,b); MIC-CdS4/PMMA (w/w) = 30/70 (c,d); and MIC-CdS4/PMMA (w/w) = 10/90 (e,f). For the 2D images, the edge length is 100 μm; the 3D representations clearly show the topology of the various raised PS/QD features patterned on the glass substrate.

varying the length of PS chains on the colloidal MIC-CdS4 building blocks, this strategy offers the possibility of tuning the average spacing of QDs and the number of QDs per unit volume within the various features, independent of the morphology and correlation length of the surface pattern.

The main PL features of MIC-CdS4 quantum dots, characterized previously in dilute toluene solution,[31] are retained in the patterned films, both before and after etching with acetone. Figure 3.6 shows the PL spectra of spin-cast MIC-CdS4/PMMA films before and after removal of the PMMA phase, revealing in both cases a sharp band-edge emission at ~470 nm and a broad trap-state emission centered at ~625 nm, very close to the peak positions obtained for MIC-CdS4 in toluene;[31] a slight broadening and blue shift in the band-edge emission is found following etching, which may be due to increased light scattering from the etched films due to a higher refractive index contrast between MIC-CdS4 and air compared to MIC-CdS4 and PMMA. LSCFM of the various films following removal of PMMA also confirmed that the self-assembled QD patterns retain their PL following etching, as shown by the LSCFM image for the etched 10/90 MIC-CdS4/PMMA film (Figure 3.6, inset).

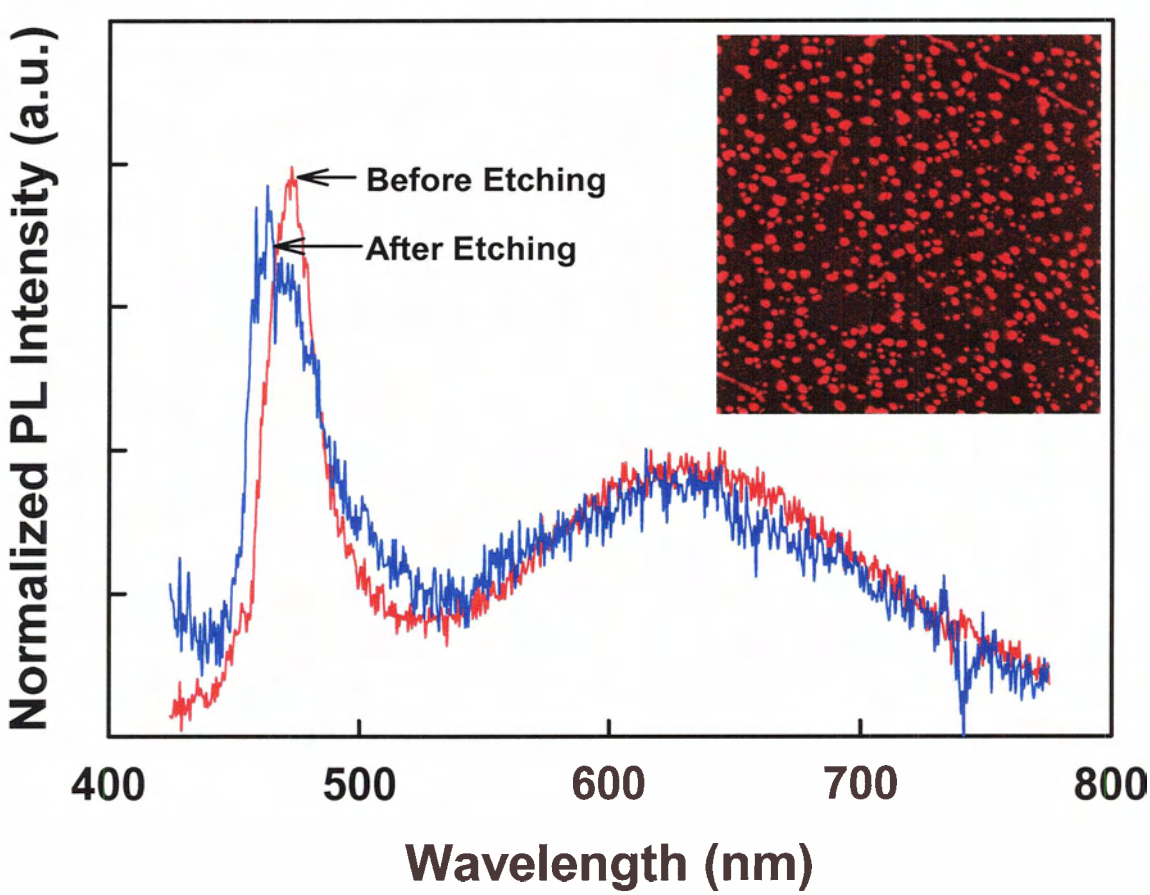

Figure 3.6. PL spectra (λ_{ex} = 400 nm) of the spin-cast 50/50 MIC-CdS4/PMMA film obtained at 9000 rpm, before and after removal of PMMA by etching with acetone. The PL peak positions are similar to those obtained previously for MIC-CdS4 in toluene (ref. 25). The inset shows the LSCFM image of the MIC-CdS4/PMMA (w/w) = 10/90 (3000 rpm) film after etching, showing that the PL of the PS/QD features is retained; the edge length of the inset is 100 μm.

3.4. Conclusions

In this chapter, we have demonstrated a novel and versatile strategy for the fast and efficient lateral patterning of semiconducting QDs in thin polymer films via spinodal decomposition between two polymer blend components, one of which is attached as a polymer brush layer to the QD surface. Simple spin-casting and solvent evaporation induces simultaneous organization of QDs on two disparate length scales, with polymer/polymer phase separation giving rise to tunable microscopic lateral patterning (with mesoscopic feature heights), and steric interactions between the polymer brush layers of neighboring QDs giving rise to a liquid-like distribution of QDs on the nano-scale. Subsequent selective removal of the PMMA component allows the production of various photoluminescent PS/QD patterns with structural hierarchy on glass substrates.

We note that despite the control over size and morphology that has been demonstrated in this chapter, the obtained patterns are isotropic, with no long-range order. However, our bottom-up approach to patterning semiconducting QDs via polymer-polymer phase separation could be combined with top-down methods of surface patterning (e.g. microcontact printing), in order to precisely guide the self-organization of QDs into well-defined and ordered patterns on the micron and sub-micron scale. This strategy has been previously used to replicate surface patterns of monolayers via phase separation of immiscible homopolymers[28], but has yet to be applied to nanoparticle self-assembly in polymer films. We have therefore begun to pattern octadecyltrichlorosilane (OTS) monolayers onto glass substrates via microcontact printing, followed by spin-casting our MIC-CdS nanoparticle/PMMA solutions onto the patterned substrate. Due to hydrophobic-hydrophobic interactions coupled to polymer/polymer phase separation,

preferential wetting of the MIC-CdS brushes onto the OTS patterned areas should occur, providing a tool for precisely fabricating many desirable patterns for specific function.

3.5. References

(1) Hua, F.; Shi, J.; Lvov, Y.; Cui, T. *Nano lett.* **2002**, *2*, 1219.

(2) Cui, Y.; T, M.; Liddle, J. A.; Sonnichsen, C.; Boussert, B.; Alivisatos, A. P. *Nano lett.* **2004**, *4*, 1093.

(3) Hess, H.; Matzke, C. M.; Doot, R. K.; Clemmens, J.; Bachand, G. D.; Bunker, B. C.; Vogel, V. *Nano lett.* **2003**, *3*, 1651.

(4) Porter, L. A.; Jr; Choi, H. C.; J. M. Schmeltzer; Ribbe, A. E.; Elliott, L. C. C.; Buriak, J. M. *Nano lett.* **2002**, *2*, 1369.

(5) Ge, G.; Brus, L. *J. Phys. Chem. B* **2000**, *104*, 9573.

(6) Maillard, M.; Motte, L.; Ngo, A. T.; Pileni, M. P. *J. Phys. Chem. B* **2000**, *104*, 11871.

(7) Rabani, E.; Reichman, D. R.; Geissler, P. L.; Brus, L. E. *Nature* **2003**, *426*, 271.

(8) Taylor, M. D. R.; Moriarty, P.; Brust, M. *Chem. Phys. Lett.* **2001**, *348*, 27.

(9) Mougin, K.; Haidara, H. *Langmuir* **2002**, *18*, 9566.

(10) Martin, C. P.; Blunt, M. O.; Moriarty, P. *Nano lett.* **2004**, *4*, 2389.

(11) Boker, A.; Lin, Y.; Chiapperini, K.; Horowitz, R.; Thompson, M.; Carreon, V.; Xu, T.; Abetz, C.; Skaff, H.; Dinsmore, A. D.; Emrick, T.; Russell, T. P. *Nature Materials* **2004**, *3*, 302.

(12) Saunders, A. E.; Shah, P. S.; Sigman, M. B.; Hanrath, T.; Hwang, H. S.; Lim, K. T.; Johnston, K. P.; Korgel, B. A. *Nano lett.* **2003**, *4*, 1943.

(13) Lopes, W. A.; Jaeger, H. M. *Nature* **2001**, *414*, 735.

(14) Bockstaller, M. R.; Lapetnikov, Y.; Margel, S.; Thomas, E. L. *J. Am. Chem. Soc.* **2003**, *125*, 5276.

(15) Sohn, B.-H.; Choi, J.-M.; Yoo, S. I.; Yun, S.-H.; Zin, W.-C.; Jung, J. C.; Kanehara, M.; Hirata, T.; Teranishi, T. *J. Am. Chem. Soc.* **2003**, *125*, 6368.

(16) Misner, M. J.; Skaff, H.; Emrick, T.; Russell, T. P. *Adv. Mater.* **2003**, *15*, 221.

(17) Yeh, S.-W.; Wei, K.-H.; Sun, Y.-S.; Jeng, U.-S.; Liang, K. S. *Macromolecules* **2003**, *36*, 7903.

(18) Chung, S.-W.; Markovich, G.; Heath, J. R. *J. Phys. Chem. B* **1998**, *102*, 6685.

(19) Sear, R. P.; Chung, S.-W.; Markovich, G.; Gelbart, W. M.; Heath, J. R. *PRE* **1999**, *59*, 6255.

(20) Tanaka, K.; Takahara, A.; Kajiyama, T. *Macromolecules* **1996**, *29*, 3232.

(21) Walhein, S.; Boltau, M.; Mlynek, J.; Krausch, G.; Steiner, U. *Macromolecules* **1997**, *30*, 4995.

(22) Ton-That, C.; Shard, A. G.; Daley, R.; Bradley, R. H. *Macromolecules* **2000**, *33*, 8453.

(23) Harris, M.; Appel, G.; Ade, H. *Macromolecules* **2003**, *36*, 3307.

(24) Walheim, S.; Ramstein, M.; Steiner, U. *Langmuir* **1999**, *15*, 4828.

(25) Ribbe, A. E.; Hashimoto, T. *Macromolecules* **1997**, *30*, 3999.

(26) Takeno, H.; Iwata, M.; Takenaka, M.; Hashimoto, T. *Macromolecules* **2000**, *33*, 9657.

(27) Wang, W.; Shiwaku, T.; Hashimoto, T. *Macromolecules* **2003**, *36*, 8088.

(28) Boltau, M.; Walheim, S.; Mlynek, J.; Krausch, G.; Steiner, U. *Nature* **1998**, *391*, 877.

(29) Sprenger, M.; Walheim, S.; Schafle, C.; Steiner, U. *Adv. Mater.* **2003**, *15*, 703.

(30) Grohn, F.; Gu, X.; Grull, H.; Meredith, J. C.; Nisato, G.; Bauer, B. J.; Karim, A.; Amis, E. *Macromolecules* **2002**, *35*, 4852.

(31) Wang, C.-W.; Moffitt, M. *Langmuir* **2004**, *20*, 11784.

(32) Wang, C.-W.; Moffitt, M. *Langmuir* **2005**, *21*, 2465.

(33) McConnell, G. A.; Gast, A. P. *Macromolecules* **1997**, *30*, 435.

CHAPTER 4

USE OF BLOCK COPOLYMER-STABILIZED CADMIUM SULFIDE QUANTUM DOTS AS NOVEL TRACERS FOR LASER SCANNING CONFOCAL FLUORESCENCE IMAGING OF POLYMER BLEND MORPHOLOGY

4.1. Introduction

Laser scanning confocal fluorescence microscopy (LSCFM) is a powerful imaging technique that has long been applied to biological systems and, in recent years, has become increasingly relevant to polymer science.[1-15] The main advantage of LSCFM is provided by special confocal optics, which only allows light from a thin focal plane (ca. 1 μm thick) to reach the detector at a given focus level; by adjusting the focus in a stepwise fashion, optical sections at different depths can be obtained and compiled into a three-dimensional image. Such fast and *in situ* three-dimensional imaging, without the need for destructive and time-consuming physical sectioning of the sample, has been used by several groups to obtain valuable 3D structural information in various systems of phase separating polymer blends, including detailed characterization of surface and bulk morphologies in polymer blend thick films,[5-10,12,13] and real-time visualization of bicontinuous morphology evolution in blends undergoing spinodal decomposition.[4]

Contrast for LSCFM is provided by light emission from fluorescent dyes, which are added to the sample as labels or tracers that become localized at specific structural features. These dyes are generally organic molecules, although for biological LSCFM imaging an increasing amount of attention has turned to the use of colloidal semiconductor nanoparticles, or quantum dots (QDs, e.g. CdS and CdSe), as fluorescent labels.[16-21] These quantum dots display intense and size-tunable light emission, high photostability, and broad excitation spectra, offering numerous advantages over more traditional organic fluorescent dyes. Most of the initial efforts towards applying colloidal quantum dots as labels in biological systems have focused on rendering them water-soluble and compatible with biological environments, by replacing the typical tri-*n*-

octylphosphine oxide (TOPO) surface ligands with hydrophilic and biocompatible surface groups. Similar issues are relevant to the potential application of quantum dots as fluorescent agents for LSCFM imaging of polymer blend systems: TOPO-coated quantum dots show poor compatibility with polymer environments, generally leading to quantum dot agglomeration and quenching of fluorescence within the polymer matrix.[22]

In recent years, several groups, including ours, have used various strategies for coating quantum dots with a polymer brush layer,[23-31] opening the door to uniform dispersions of inorganic nanoparticles within homopolymers that are compatible with the polymer brush.[23,28,32,33] These polymer-quantum dot composite nanoparticles have great potential as fluorescent tracers for LSCFM imaging of phase-separating polymer blends, since small amounts of polymer-stabilized fluorescent particles could be selectively dispersed within one phase of the blend, providing contrast for imaging the blend structure. However, to our knowledge, this application of polymer-coated quantum dots has yet to be demonstrated.

In Chapter 2, we described the characterization of static and time-resolved photoluminescence (PL) properties of CdS quantum dots grown and encapsulated in the hydrophilic cores of polystyrene-*b*-poly(acrylic acid) (PS-*b*-PAA)-based block copolymer reverse micelles.[23] The resulting nanoparticles are coated with an external brush layer of PS (Scheme 4.1), making them soluble in organic solvents and allowing them to be uniformly dispersed within a matrix of polystyrene homopolymer while maintaining their fluorescence properties. This suggests the possibility of using these block copolymer-stabilized quantum dots as fluorescent tracers for the polystyrene phase in LSCFM imaging of polystyrene/poly(methyl methacrylate) PS/PMMA blends, a

system in which structure evolution via phase separation of the immiscible polymer components has been widely studied.[5-7,34-37]

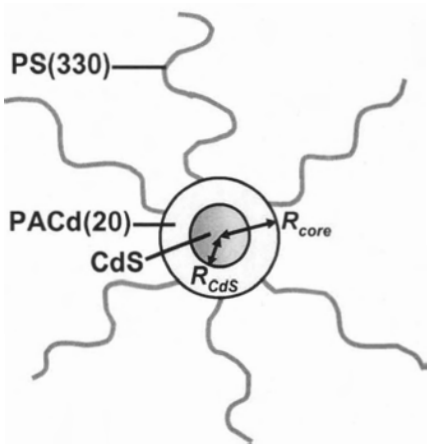

MIC-CdS4

Scheme 4.1. Representation of the polystyrene-*b*-poly(cadmium acrylate) stabilized CdS quantum dots MIC-CdS4. Numbers in brackets indicate number-average degrees of polymerization for both blocks. From static light scattering results, the chain aggregation number is ~ 430, R_{core} = 5.7 nm, and the PS brush density is ~ 1 chain/nm^2. From the absorption spectrum of the quantum dots, R_{CdS} = 2.7 nm.

In this chapter, we demonstrate the feasibility of quantum dots as fluorescent tracers for LSCFM imaging of polymer blends using the PS/PMMA blend system. In order to serve as effective tracers for the PS phase, our PS-*b*-PAA-coated CdS quantum dots must meet several criteria: 1) the quantum dots must maintain their fluorescence under the conditions of blend formation, 2) they must disperse uniformly within the PS phase, 3) they must be excluded from the PMMA phase and provide good fluorescence contrast between the two phases, and 4) the addition of suitable amounts of tracer must have a negligible effect on blend morphology. These criteria are tested by solution

casting various binary and ternary blends containing PS-*b*-PAA-coated CdS quantum dots, PS homopolymer, and PMMA homopolymer, and imaging the resulting thick films by LSCFM. Two different PS homopolymer samples are investigated for this system, with molecular weights differing by greater than a factor of 10, both to determine the versatility of the QDs as tracers for different PS phases, and to investigate the effect of molecular weight on PS/PMMA blend structure.

Along with demonstrating the applicability of a new type of quantum dot tracer for LSCFM imaging polymer blends, this work also reveals a number of interesting features in thick films (~20 μm) of 40/60 (w/w) PS/PMMA blends obtained by solvent-casting from toluene solutions. Kumacheva et al. have carried out extensive studies by LSCFM of thick films of a highly asymmetric PS/PMMA blend system (90/10 w/w) obtained by solvent casting, reporting distinct surface morphologies and surface enrichment by the PMMA component that were attributed to solvent evaporation effects.[5-7] However, more symmetric compositions of solvent-cast PS/PMMA blends have yet to be investigated in thick films, although spin-coated thin films have been extensively studied.[34-37] In the thick blend films investigated in this work, we observe a PMMA-rich layer at the glass substrate, which is found to result in a depletion of PMMA in the bulk. As well, we find a dramatic change in blend morphology for different molecular weights of the PS homopolymer. Importantly, these effects are shown to be independent of the amount of added block copolymer-stabilized quantum dots, suggesting that the QDs added to the PS phase serve as effective fluorescent tracers, without significantly affecting the evolution of phase structure within the blend.

4.2. Experimental

4.2.1. Synthesis of the Quantum Dot Tracer MIC-CdS4

The detailed synthetic procedure for the block copolymer-stabilized quantum dots MIC-CdS4 (Scheme 4.1) is provided in Chapter 2.[23] The procedure is based on the self-assembly of a polystyrene-*b*-poly(acrylic acid) (PS-*b*-PAA) block copolymer in organic solvents by the addition of cadmium acetate to form polystyrene-*b*-poly(cadmium acrylate) (PS-*b*-PACd) reverse micelles, followed by the synthesis of a single CdS quantum dot in the core of each micelle by treatment with H_2S.[38] The starting material for MIC-CdS4 was the amphiphilic block copolymer PS(330)-*b*-PAA(20) (M_w/M_n = 1.02), where the numbers in brackets denote number-average degrees of polymerization.

4.2.2. Preparation of Polymer Blend Films

Blends of MIC-CdS4, PS homopolymer, and PMMA homopolymer (Aldrich, M_w = 120,000 g/mol) were prepared by co-dissolving appropriate quantities of each component in spectroscopic grade toluene to a total polymer concentration of 4 wt %. The two PS homopolymer samples used in these experiments were prepared in our lab by anionic polymerization: PS(1250), M_w/M_n = 1.01 and PS(100), M_w/M_n = 1.04, where the numbers in parentheses indicate number-average degrees of polymerization. Blend solutions were stirred for ~2 h and left to stand overnight in the dark to equilibrate. Several drops of solution were then deposited on 18x18 mm glass cover slips, placed in Petri dishes covered with aluminum foil, and left in a fumehood to evaporate for 1 week. The resulting blend films were then dried overnight in a vacuum oven at 70 °C (below the

T_g of PS) to remove residual solvent. In some cases, subsequent annealing experiments were performed in a vacuum oven at 115 °C, ~15 °C above the T_g of PS.

Two types of blend films were prepared for the purpose of this study: 1) binary blends containing MIC-CdS4 and PS homopolymer, which were used to demonstrate dispersibility of polymer-stabilized quantum dots within the PS phase, and 2) ternary blends containing MIC-CdS4, PS homopolymer, and PMMA homopolymer, which were used to demonstrate the effectiveness of MIC-CdS4 as a fluorescent tracer for the PS phase in PS/PMMA blends.

4.2.3. Absorption and Photoluminescence Measurements

Absorption spectra were recorded on a Cary 50-scan UV-vis spectrophotometer. Static fluorescence measurements were recorded on an Edinburgh Instruments FLS 920 instrument equipped with a Xe 450W arc lamp and a red sensitive PMT (R928-P).

4.2.4. Static Light Scattering

Static light scattering (SLS) experiments were carried out on a Brookhaven Instruments multi-angle system equipped with a BI-200SM goniometer, a BI-9000AT digital autocorrelator, and a Melles Griot He-Ne Laser (632.8 nm) with maximum power output of 75 mW. To ensure the accuracy of SLS measurements, great care was taken to eliminate dust from the samples. Spectroscopic grade toluene was filtered through two membrane filters with 0.20 μm nominal pore size connected in series, and stock solutions of MIC-CdS4 colloid dispersed in toluene was filtered through two membrane filters with 0.45 μm nominal pore size connected in series. All scintillation vials were

thoroughly cleaned with filtered toluene, and stock solutions of the MIC-CdS4 were filtered into the dust-free scintillation vials. Successive dilutions of the colloids were carried out by adding known quantities of filtered toluene.

The stock solutions of MIC-CdS4 with concentrations of ca. 10 mg/mL were prepared the night before SLS measurements to ensure equilibration. SLS measurements were carried out in a concentration range from 1-0.2 mg/mL and the angles of detection ranged from 15-155° with 5 degree increments between measurements. 10 repeat measurements of scattered light intensity were taken at each angle and concentration. The reported aggregation number and radius of gyration were determined from the average results of two separate Zimm plots obtained from different stock solutions. All SLS measurements were conducted at 23 °C.

The differential refractive index *dn/dc* of MIC-CdS4 in toluene was required for Zimm plot analysis of static light scattering results. This was determined using a BI-DNDC Differential Refractometer which was calibrated using a known standard of polystyrene homopolymer in toluene. Five sample solutions in range of 5-0.5 mg/mL were used, giving *dn/dc* =0.1196 for MIC-CdS4 in toluene, compared to 0.1100 for polystyrene in toluene.

4.2.5. Laser Scanning Confocal Fluorescence Microscopy (LSCFM)

Laser scanning confocal fluorescence microscopy measurements of MIC-CdS4/PS and MIC-CdS4/PS/PMMA blend films were carried out on a Zeiss LSM 410 equipped with an Ar/Kr laser. All films were excited at 488 nm, using a bandpass 485 ± 20 nm line selection filter and a FT 510 dichroic beam splitter. A longpass 515 emission

filter was used such that only light above 515 nm reached the PMT and a Zeiss Plane-Aprochromat 63 x oil immersion objective lens was used for imaging. A pinhole diameter 0.984 Airy Units was used for all measurements, resulting in an optical section thickness of 0.62 μm FWHM. The theoretical lateral resolution is 0.21 μm.

To image the blend films, the glass cover slip on which a film had been deposited was fastened with tape to a glass microscope slide, so that the film was sandwiched between the slide and the cover slip (Scheme 4.2). A drop of Zeiss Immersionsoel 518 C

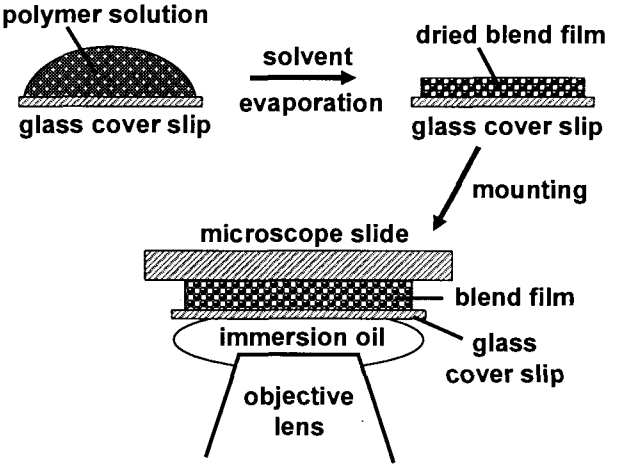

Scheme 4.2. Preparation and mounting of polymer blend films, showing geometry of LSCFM imaging: polymer/glass interface during film preparation represents the "top" of the film in imaging experiment.

oil (refractive index, n = 1.51) was then deposited on the cover slip to match the refractive index of glass, creating a constant-refractive index immersion medium between the objective lens and the sample and minimizing potential distortions and signal loss associated with a refractive index mismatch between the sample and air. Although PMMA has a refractive index very close to the immersion medium (n = 1.49), the

refractive index of PS is somewhat higher (n = 1.59); a slight overall mismatch between the sample and the immersion medium (n = 1.51) will therefore result in some loss of resolution and intensity for optical sections at increasing distances from the cover slip. As well, the refractive index difference between the PS and PMMA phases will result in some loss of fluorescence signal at increasing penetration depths due to scattering of light from the film. However, despite these experimental limitations, 3D imaging of the blend films by LSCFM can be achieved. As shown in Scheme 4.2, the polymer films are imaged from the glass cover slip downward, so that the "top" of the film in the collection of z-stacks is the film surface that was in contact with the glass substrate during solvent evaporation.

4.2.6. Transmission Electron Microscopy (TEM)

Transmission electron microscopy was performed on a Hitachi H-700 electron microscope, operating at an accelerating voltage of 70 kV. CdS QD blend films were first embedded in an Epon resin, and then 30-60 nm thick sections were produced with a diamond knife on Reichert UltraCut E ultra-microtone. The thin sections were then placed on carbon/formvar-coated 300 mesh copper grids for imaging.

4.3. Results and Discussion

4.3.1. Compatibility of MIC-CdS4 with PS Homopolymer of Different Molecular Weights

For MIC-CdS4 to serve as a tracer in PS/PMMA blends, the PS-*b*-PAA-stabilized quantum dots must be compatible with a matrix of PS homopolymer, so that they will

disperse evenly and provide uniform fluorescence contrast for the PS phase. As demonstrated in Chapter 2,[23] the PS brush layer coating the surface of the CdS nanoparticles renders MIC-CdS4 soluble in a wide range of organic solvents. As well, it was shown that 20/80 (w/w) MIC-CdS4/PS blends with PS homopolymers of different molecular weights (PS(1250) and PS(100)), solution cast from toluene, yielded optically transparent fluorescent films.[23] Figure 4.1 shows the absorption and fluorescence emission spectra of MIC-CdS4 in toluene solution, as well as the fluorescence emission of the 20/80 MIC-CdS4/PS(1250) blend film. The absorption spectrum is characteristic of colloidal CdS quantum dots, with a distinct exciton shoulder and an absorption edge that is blue-shifted with respect to bulk CdS; from the position of the absorption edge, the average diameter of the CdS quantum dots was determined to be 5.4 nm. The fluorescence spectrum of the quantum dots shows two distinct peaks: a band edge peak attributed to emission from states close in energy to the exciton, and a broad red-shifted peak attributed to surface trap states. The shape and peak positions of the quantum dots in solution and in the polymer film are found to be very similar, indicating that MIC-CdS4 maintains its fluorescence properties within the polymer matrix.

Along with probing the versatility of these potential quantum dot tracers in polymer melt environments, a comparison of the compatibility of MIC-CdS4 in PS homopolymers of different molecular weights provides some insight into the fundamentally interesting problem of spherical polymer brushes dispersed in a matrix of chemically identical homopolymer. Attachment of polymer brushes to the surface of spherical particles has been recognized as an effective way of promoting repulsive interactions between particles within an enthalpically "neutral" polymer matrix ($\chi = 0$ for

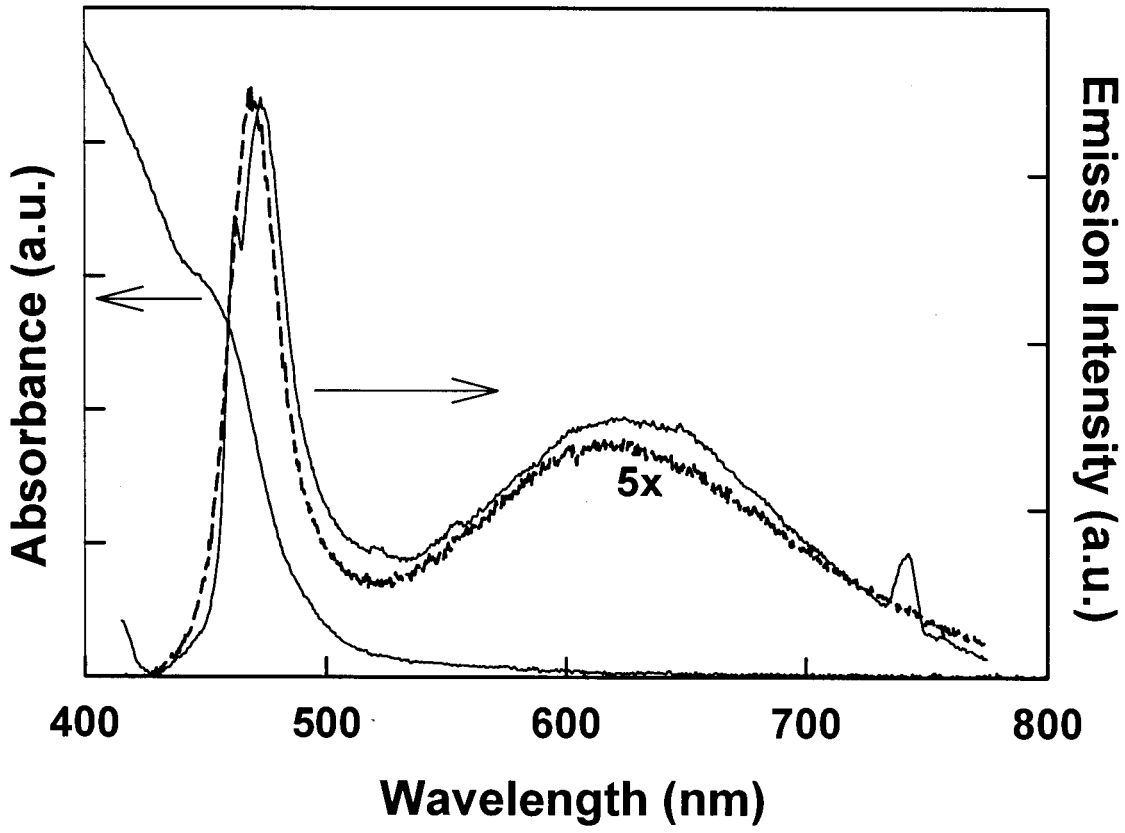

Figure 4.1. Absorption and photoluminescence emission spectra of MIC-CdS4. The absorption spectrum was obtained from a dilute toluene solution of MIC-CdS4, with the corresponding emission spectrum represented by a dotted line. The solid line shows the emission spectrum from a 20/80 solid film of MIC-CdS4/PS(1250).

matrix and brush polymers), thus enhancing particle dispersion.[28,32,33,39-43] Despite the simplicity of this idea, entropic effects place constraints on the wetting of the brush layer by the homopolymer solvent, so that repulsive interactions between particles are sensitive to the molecular weights of the brush and matrix polymers and to the grafting density.[32,33,39-45] In general, brush swelling and particle dispersion is promoted by brush chains that are long relative to the solvent chains, and a grafting density that is not too large. However, the high curvature in star-like systems (small cores relative to the brush layer) tends to increase brush swelling and thus the range of repulsive interactions between particles.[43,44,46,47] It is therefore difficult to predict the compatibility of different systems of polymer-stabilized particles in a polymer matrix, based solely on knowledge of relative chain lengths and grafting density; however, most empirical examples of good particle dispersion have been for systems with brush chains longer than the solvent chains and relatively low grafting densities.[39,41-43]

The PS-*b*-PAA-stabilized quantum dots MIC-CdS4 fit the description of star-like spherical polymer brushes (Scheme 4.1), with PS "brush" chains covalently attached to a CdS/PACd core. We carried out static light scattering (SLS) measurements of these particles in toluene solutions over a range of angles and concentrations, and determined from Zimm plot analysis a weight-average aggregation number of 430 ± 30 PS-*b*-PACd chains per composite particle. Also from SLS, the radius of gyration R_g of the particles was determined to be 40 ± 4 nm, compared to a hydrodynamic radius R_h of 37 nm in toluene as determined previously by DLS;[23] we thus obtain a ratio of $R_g/R_h \sim 1$ for these particles, consistent with individual star-like spherical brushes.[48,49] From the chain

aggregation number in toluene and the CdS nanoparticle radius of R_{CdS} = 2.7 nm, we calculate a total core radius of R_{core} = 5.7 nm for our spherical brushes, assuming a poly(cadmium acrylate) density of 2 g/mL. This gives a brush density of ~1 PS chain/nm^2 on the surface of the particles.

LSCFM images of the 20/80 MIC-CdS4/PS blends were used to probe the degree of dispersion of these composite particles, which have average brush chain lengths of 330 styrene units, in homopolymer matrices of PS(1250) (Figure 4.2A and 4.2B) and PS(100) (Figure 4.2C and 4.2D). Figure 4.2A and 4.2C show images of the blends after solvent evaporation and drying below the T_g of PS, while Figure 4.2B and 4.2D show the same films after annealing for 8 days at 115°C, above the T_g of PS. All four images show fluorescence that is spatially uniform, with no evidence of agglomeration or phase separation of MIC-CdS4 from either PS homopolymer, at least on optical length scales. Importantly, the dispersion of the quantum dots, along with their fluorescence, is stable to long periods of annealing. Such stable and spatially uniform fluorescence points to excellent potential for MIC-CdS4 as a fluorescent tracer for PS matrices of various molecular weights.

On the basis of these LSCFM results, MIC-CdS4, with brush chains of 330 repeat units and a PS brush density of ~1 chain/nm^2, appears to be equally compatible with the PS(100) and PS(1250) homopolymer. We find this compatibility to be thermodynamic in nature, and not simply a "freezing in" of nanoparticle dispersion due to fast solvent evaporation, since 8 days annealing above the T_g of PS has no effect on the QD dispersion. Though MIC-CdS4 compatibility with PS(100) is expected, considering the

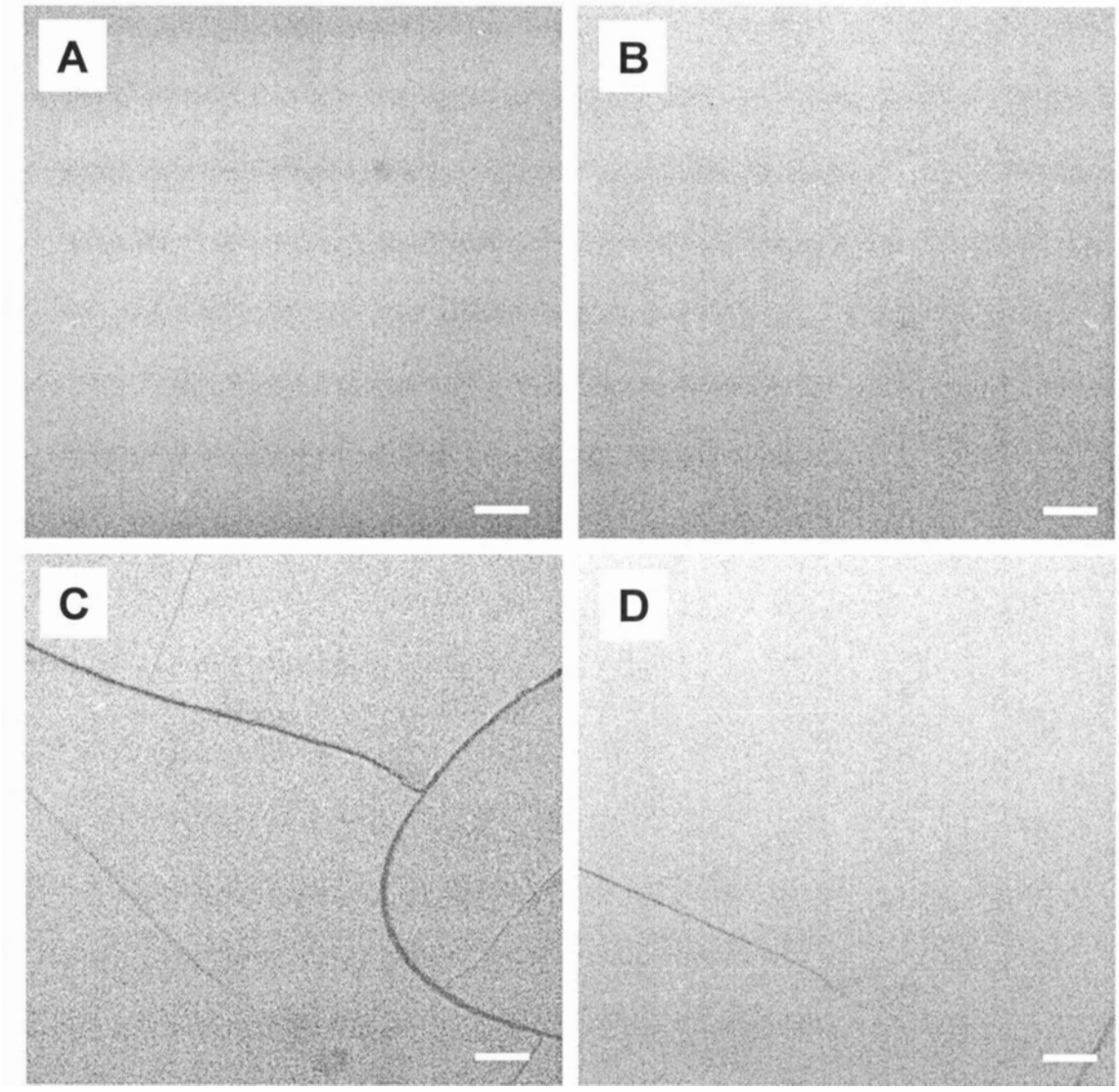

Figure 4.2. LSCFM images of 20/80 blend of MIC-CdS4/PS(1250) before annealing (A) and after annealing for 8 days at 115° C (B); and 20/80 blend of MIC-CdS4/PS(100) before annealing (C) and after annealing for 8 days at 115° C (D). The scale bars represent 20 μm.

short solvent chains relative to the brush chains, compatibility with PS(1250) is somewhat surprising, especially in light of the high brush density in the present system compared to optimum densities found by Hasegawa et al. (0.08 chains/nm^2).[39] However, we remind the reader of the high curvature of the present system, which tends to promote increased swelling and particle dispersion. In a star-like system with comparable curvature, Corbierre et al. have recently shown that gold nanoparticles decorated at grafting densities of ~ 1 chain/nm^2 with PS chains of 125 repeat units could be well dispersed in a PS matrix of chains with an average degree of polymerization of 450.[32,33]

More detailed information on the CdS particle dispersion in the two different PS matrices is gained from transmission electron microscopy (TEM), which is able to probe the spatial distribution of quantum dots well below optical length scales. TEM seems confirm the LSCFM results, showing uniform distribution of nanoparticles in both matrices with no visible agglomeration (Figure 4.3). We note that the patchy appearance in the background in Figure 4.3B (low-molecular weight matrix) is a feature of the polymer matrix and is not due to clustering of QDs. This was confirmed by inspecting several regions throughout the film, and confirming that the distribution of QDs is uniform and independent of the location of dark "patches"; the reason for these dark patches is unclear, though they may be attributed to fluctuations in the thickness of microtome sections obtained from the low-molecular weight blend.

4.3.2. LSCFM Imaging PS/PMMA Blends Using the MIC-CdS4 QD Tracer

Having found that these block-copolymer stabilized quantum dots could be well dispersed within PS homopolymers of different molecular weights, yielding uniform

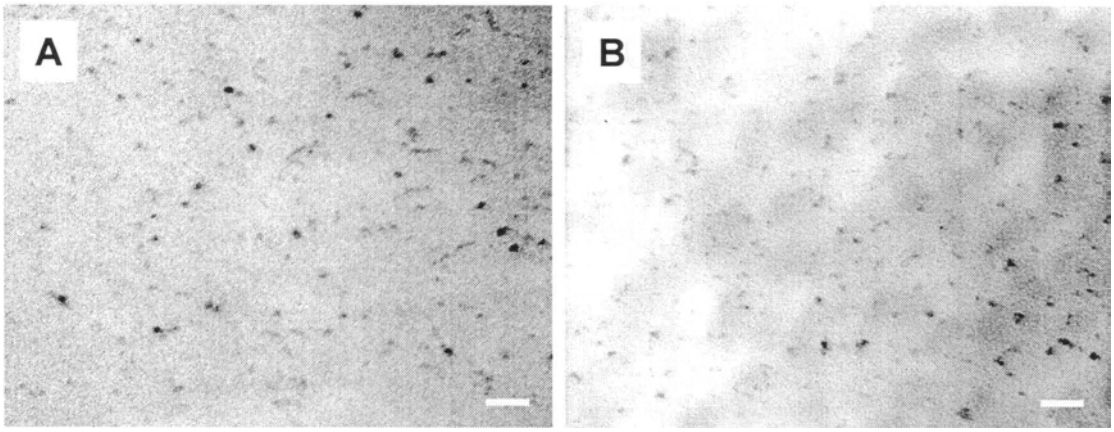

Figure 4.3. TEM of 20/80 blends of MIC-CdS4/PS(1250) (A) and MIC-CdS4/PS(100) (B). The scale bars represent 50 nm.

fluorescence on optical length scales, we wished to demonstrate their applicability as tracers for LSCFM imaging of PS/PMMA blends. For these experiments, the following two blends were prepared by solvent-casting from toluene solutions and overnight drying at 70 °C to remove residual solvent: 8/32/60 (w/w/w) MIC-CdS4/PS(1250)/PMMA and 8/32/60 MIC-CdS4/PS(100)/PMMA. Note that the only difference between these blends is the molecular weight of the PS homopolymer (and therefore the number of PS chains). The MIC-CdS4 content relative to the PS phase in both ternary blends is identical to that in the binary blends discussed previously, such that we can assume that the first two components in the ternary blends mix uniformly to form a single PS phase which consists of 20 wt % MIC-CdS4 tracer and 80 wt % PS(1250) or PS(100). In both cases, the ratio of PS components (MIC-CdS4 plus PS homopolymer) to PMMA is 40/60 (w/w).

Figure 4.4 shows LSCFM images of the 8/32/60 MIC-CdS4/PS(1250)/PMMA ternary blend, containing the higher molecular weight PS sample, both in the bulk (Figure 4.4A) and near the glass substrate (Figure 4.4B). The "bright" regions in these images represent the PS phase, with brightness provided by fluorescence emission from the CdS quantum dots uniformly dispersed throughout this phase, while "dark" regions are attributed to phase-separated PMMA. The distinct contrast between the PS and PMMA phases, and the well-resolved structure of these phase-separated films as observed by LSCFM, clearly indicates that the quantum dots are excluded from the PMMA phase, and thus serve as effective tracers for the PS phase in fluorescence imaging the blend structure. We will show later on that the presence of MIC-CdS4 tracer has a negligible effect on the observed blend morphology. For now, we turn our attention to a description of the PS/PMMA blend structure, as revealed by the quantum dot tracers.

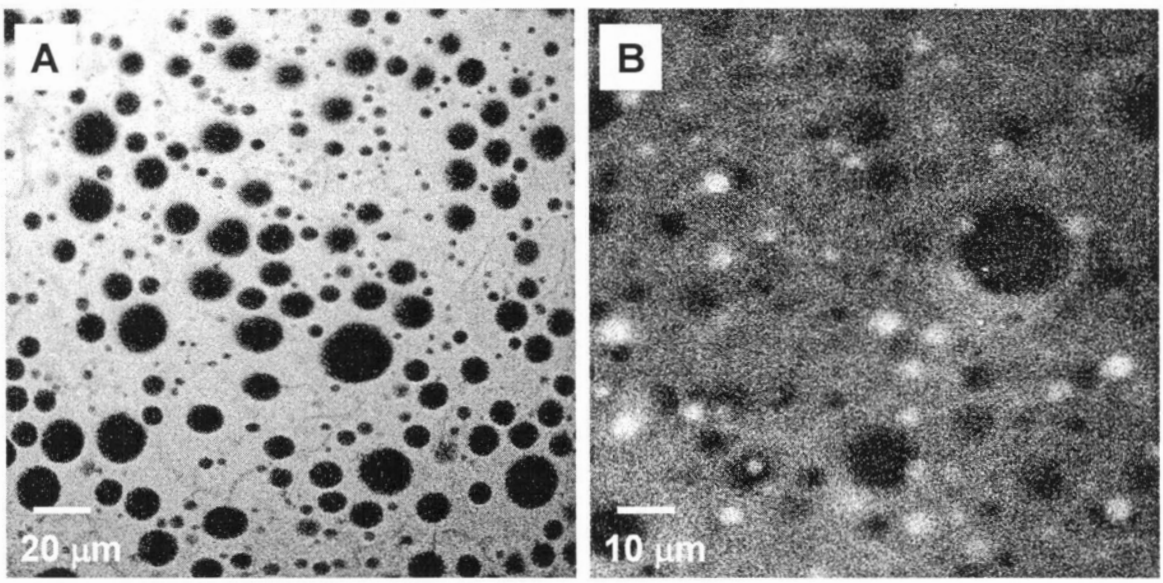

Figure 4.4. LSCFM images of bulk (A) and substrate interface (B) morphology of the 8/32/60 MIC-CdS4/PS(1250)/PMMA blend.

The bulk structure of the 8/32/60 MIC-CdS4/PS(1250)/PMMA film (Figure 4.4A) shows spherical droplets of PMMA, with sizes ranging from 2-25 μm, dispersed within a PS continuous phase. The spatial distribution of these droplets suggests that phase separation in the film occurred by a mechanism of spinodal decomposition (SD) during evaporation of solvent,[1-4,7] with an initial bicontinuous structure breaking down into discrete droplets (percolation-to-cluster transition, PCT) as a result of coarsening.[2] The broad droplet size distribution suggests further coarsening of droplets following the PCT via coalescence or Ostwald ripening.[7] Another observed feature in the bulk phase structure are some very faint dark and irregular lines throughout the "bright" PS phase; the origin of these lines is unclear: they may be cracks in the film which evolved during solvent evaporation, or phase-separated PMMA that has not yet coarsened into discrete droplets. They are not attributed to phase separation between tracer and the PS homopolymer, since lines of this type were not observed in the binary blends of homopolymer and tracer at the same tracer composition relative to PS, even after long periods of annealing (Figure 4.2A and B).

Notably, PS is the continuous phase in the bulk (Figure 4.4A), although PMMA is the overall major component at 60 wt %; this suggests a depletion of PMMA in the bulk since a dispersed phase consisting of the minor component is normally observed.[50] The "top" surface of the film with respect to the objective lens (Scheme 4.2) represents the interface between the polymer and the glass substrate, where we find a significant difference from the phase structure of the bulk: in contrast to the PMMA-in-PS morphology in the bulk, a layer near the substrate contains bright islands of the PS phase (3 – 6 μm in diameter), which suggests a continuous matrix of PMMA (Figure 4.4B) at

the interface between glass and the polymer film. The effect of surfaces on the phase separation of polymer blends has been found to result in significant differences between bulk and surface blend compositions in various systems of both thin and thick films, attributed to selective substrate wetting,[34-37] segregation of low-surface energy components,[34-37] or solvent evaporation effects.[7,34,35] In the present case, we attribute the formation of a PMMA-rich layer to strong attractive interactions between PMMA and the glass substrate during solvent evaporation. This concentration of PMMA at the glass substrate could account for a depletion of PMMA in the bulk and the observed PMMA-in-PS bulk morphology despite PMMA being the overall major component. A *z*-stack consisting of 0.5 micron steps shows the transition from the PS-in-PMMA layer at the glass substrate to the PMMA-in-PS phase structure which is observed throughout the bulk (Figure 4.5). We note that the apparent alignment of PMMA droplets into "strings" in the bulk region may be due to the fact that the droplets formed from an original bicontinuous structure (spinodal decomposition) which gave way to an eventual percolation-to-cluster transition during coarsening.

We have carried out domain area analysis for optical sections in the bulk and at polymer/glass interface in order to compare the depletion of PMMA in the bulk with PMMA enrichment in the interface layer. The percentage area of dispersed domains was determined by first binarizing the images, followed by blurring to reduce background noise and area analysis using Image-Pro Plus software. In this manner, we determined an average volume fraction of 0.26 for PMMA in the bulk, compared to 0.97 at the polymer/glass interface. From *z*-stacks collected through the film, the thickness of the interface layer is estimated to be ~ 4 μm, compared to a thickness of ~ 10-15 μm for the

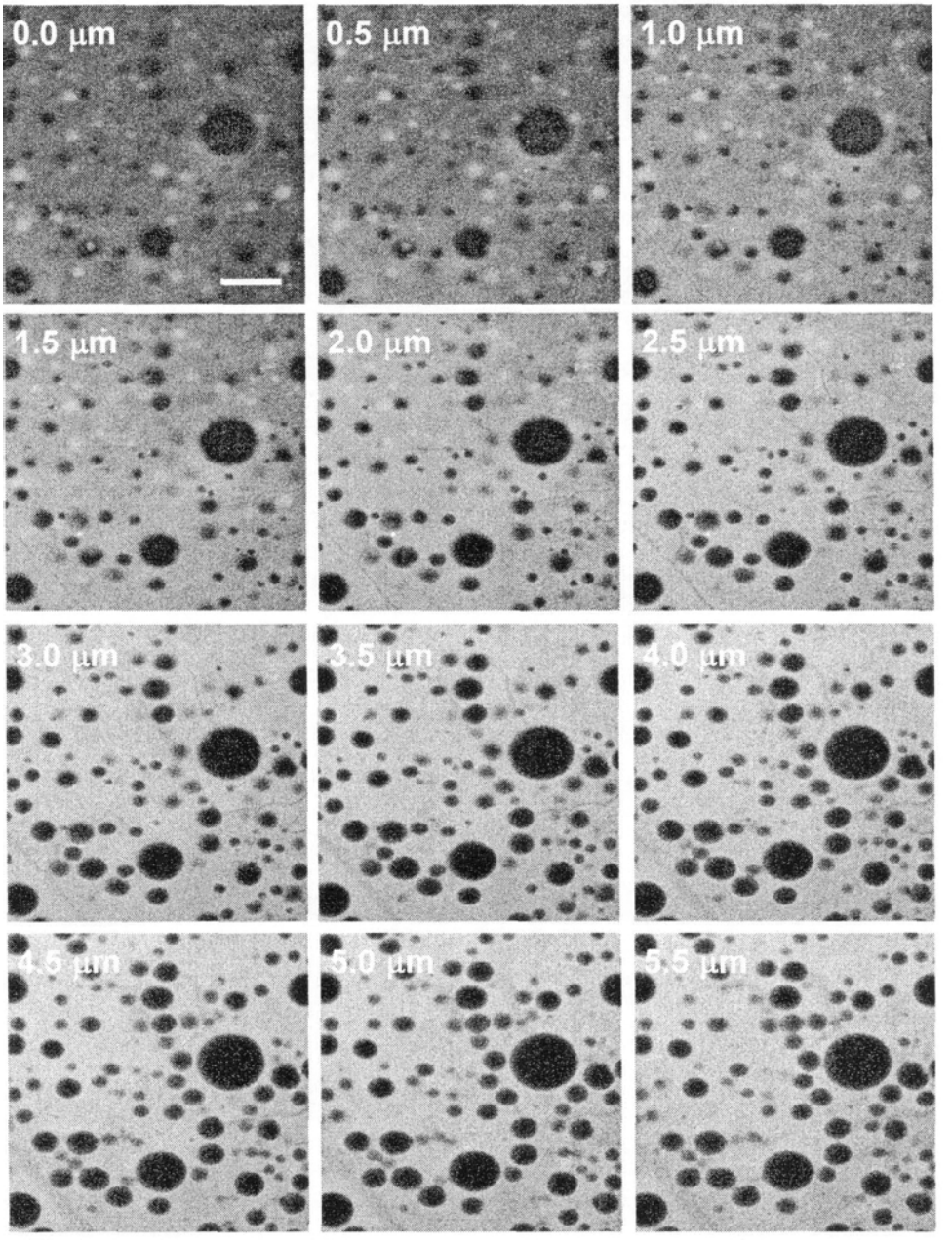

Figure 4.5. *z*-stack of LSCFM images of the 8/32/60 MIC-CdS4/PS(1250)/PMMA blend taken at different distances from the glass substrate, with 0.5 μm-steps between images. The scale bar represents 20 μm.

bulk region, which gives an overall volume fraction of 0.41-0.46 PMMA or a mass fraction of 0.45-0.51 in the film (accounting for the difference in densities of PS and PMMA). This is somewhat less than the known mass fraction of PMMA in the film (0.60), although the discrepancy can be accounted for by considering sources of error. First, the thickness of the PMMA concentration layer may be underestimated since it can only be detected by LSCFM due to the presence of bright PS islands (i.e. the presence of a layer of pure PMMA would not be detected). Second, the volume fraction of PMMA in the bulk is likely underestimated by area analysis, which tends to omit domains below a critical size. Therefore, it is reasonable to conclude that the formation of a wetting layer rich in PMMA at the glass substrate results in a depletion of PMMA in the bulk and a PMMA-in-PS bulk phase structure.

To determine further information on phase structure, the *z*-stack in Figure 4.5 was compiled to yield a 3D representation of film morphology. Cross-sections of the film could then be viewed by selecting a plane along the *x*- or *y*-direction. Samples of two cross-sections (cross-section planes indicated by lines in the accompanying *xy* image) (Figure 4.6) clearly reveal an interesting aspect of the PMMA droplet morphology: droplets with lateral dimensions less than the film thickness appear spherical, whereas droplets with lateral dimensions comparable to or larger than the film thickness are "flattened", with an ellipsoidal shape. This is exemplified by the appearance of cross-sections taken through the largest droplet in the *xy* image in Figure 4.6, showing that the droplet is elongated in both directions in the plane of the film. The ellipsoidal droplet morphology can be viewed as a compromise between 3D phase separation, and the constraints of a quasi-2D film of finite thickness.[35] Due to increased scattering of

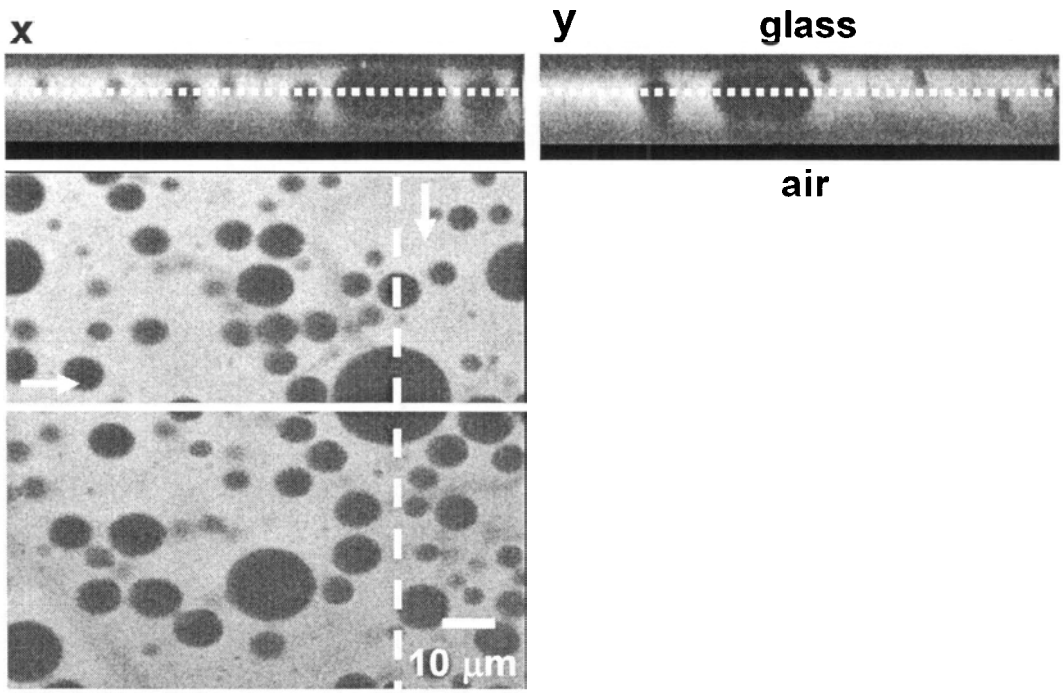

Figure 4.6. Cross-sections of the 8/32/60 MIC-CdS4/PS(1250)/PMMA blend taken from a 3D compilation of the *z*-stack. On the *xy* image, the solid line represents the plane of the "*x*" cross-section and the dashed line represents the plane of the "*y*" cross-section. Arrows indicate the "left-to-right" directions in the corresponding cross-sections. The dotted line through the cross-sections represents the plane of the *xy* image.

fluorescence emission moving toward the air interface of the film, the "bottom" of the large ellipsoidal droplet cannot be clearly imaged. However, it is clear that the top of flattened droplet is not "closed" by a PS/PMMA interface, but rather forms a direct contact with the PMMA-rich layer near the glass substrate.

An equivalent blend composition of 8/32/60 MIC-CdS4/PS(100)/PMMA, containing the lower-molecular weight PS homopolymer, shows a very different phase structure from the previous film following solvent evaporation (Figure 4.7). In contrast with the PS(1250) blend, the bright PS phase is now dispersed as large irregularly-shaped droplets (~ 20-100 μm lateral dimensions) in the dark PMMA continuous phase; in addition, these large droplets are found to contain a scattering of small dark domains (1-2 μm diameter), which are also attributed to phase-separated PMMA (Figure 4.7, insert). This type of phase-in-phase structural complexity has previously been observed in ternary blend systems, including spin-coated polystyrene/poly(methyl methacrylate)/poly (2-vinylpyidine),[51] and also in solvent-cast binary blends of polystyrene/poly(4-methylstyrene).[52] We believe the phase-in-phase structure in the present system has more in common with the latter case, since our ternary blends are two-phase systems which exhibit no phase separation between the tracer and PS homopolymer.

The effect of interfacial tension on morphology evolution in polymer blends has been well documented.[53] As well, the relationship between interfacial tension and polymer molecular weight has been studied both theoretically and empirically.[54,55] Anastasiadis et al. investigated molecular weight effects on interfacial tension in a number of systems, including PS/PMMA with PMMA ($M_n = 10^4$, $M_w/M_n = 1.05$) and PS ranging from M_n = 2200 to 43700 (M_w/M_n = 1.04-1.18), in which range the interfacial

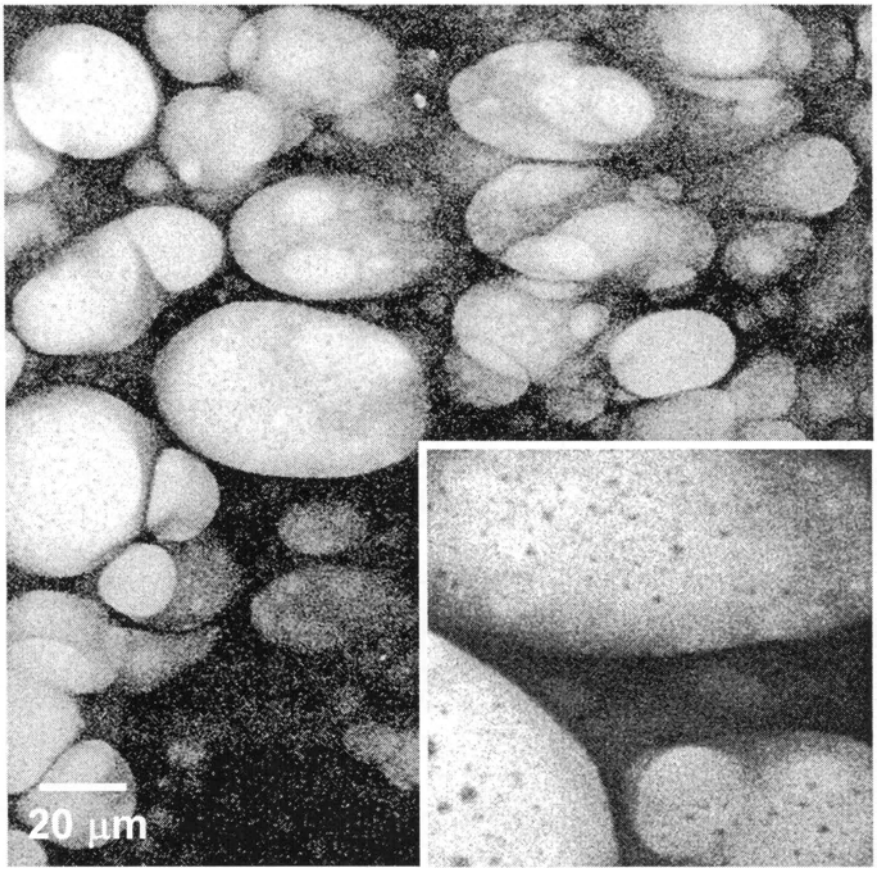

Figure 4.7. LSCFM image of the 8/32/60 MIC-CdS4/PS(100)/PMMA blend. The insert shows a higher-magnification image of the internal structure of the PS droplets, revealing small internal domains of PMMA.

tension showed a clear decrease with decreasing molecular weight of PS.[54] This is generally considered to be an entropic effect, related to an increase in the free energy of mixing for lower molecular weight polymers, which becomes less important as the interacting polymers approach infinite molecular weight.[55] In the present system, our low-polydispersity ($M_w/M_n \leq 1.04$) PS samples are M_n = 10400 and 130000, spanning the range of expected molecular weight dependence of interfacial tension from ref. 54. Our commercial PMMA sample is $M_w = 1.2 \times 10^5$, higher than the PMMA used by Anastasiadis et al., although our PMMA is more polydisperse, such that interfacial effects should be governed by the lower end of the distribution. Based on the results of Anastasiadis et al., it is therefore reasonable to attribute the differences in morphology between Figure 4.4 and Figure 4.7 to a decrease in interfacial tension associated with a decrease in the molecular weight of the PS homopolymer. This is supported by the nature of the phase-in-phase structure observed for the blend containing the lower-molecular weight PS: due to the many small (1-2 μm) PMMA domains scattered within the larger PS domains (Figure 4.7), this morphology should have a higher total interfacial area than the PMMA droplet morphology observed in the higher-molecular weight blend (Figure 4.4A); unfortunately, this is impossible to confirm without better spatial resolution of the phase structure, which can only be obtained using non-optical techniques such as TEM. We also note that other examples of phase-in-phase structural complexity for binary blends in the literature are in systems with low polymer-polymer interaction energies and low interfacial tension.[52] A *z*-stack of this blend reveals that a PMMA-rich layer is also present in this sample (Figure 4.8), as LSCFM imaging near the glass substrate reveals smaller PS droplets with a total area of PS domains that is lower than in the bulk.

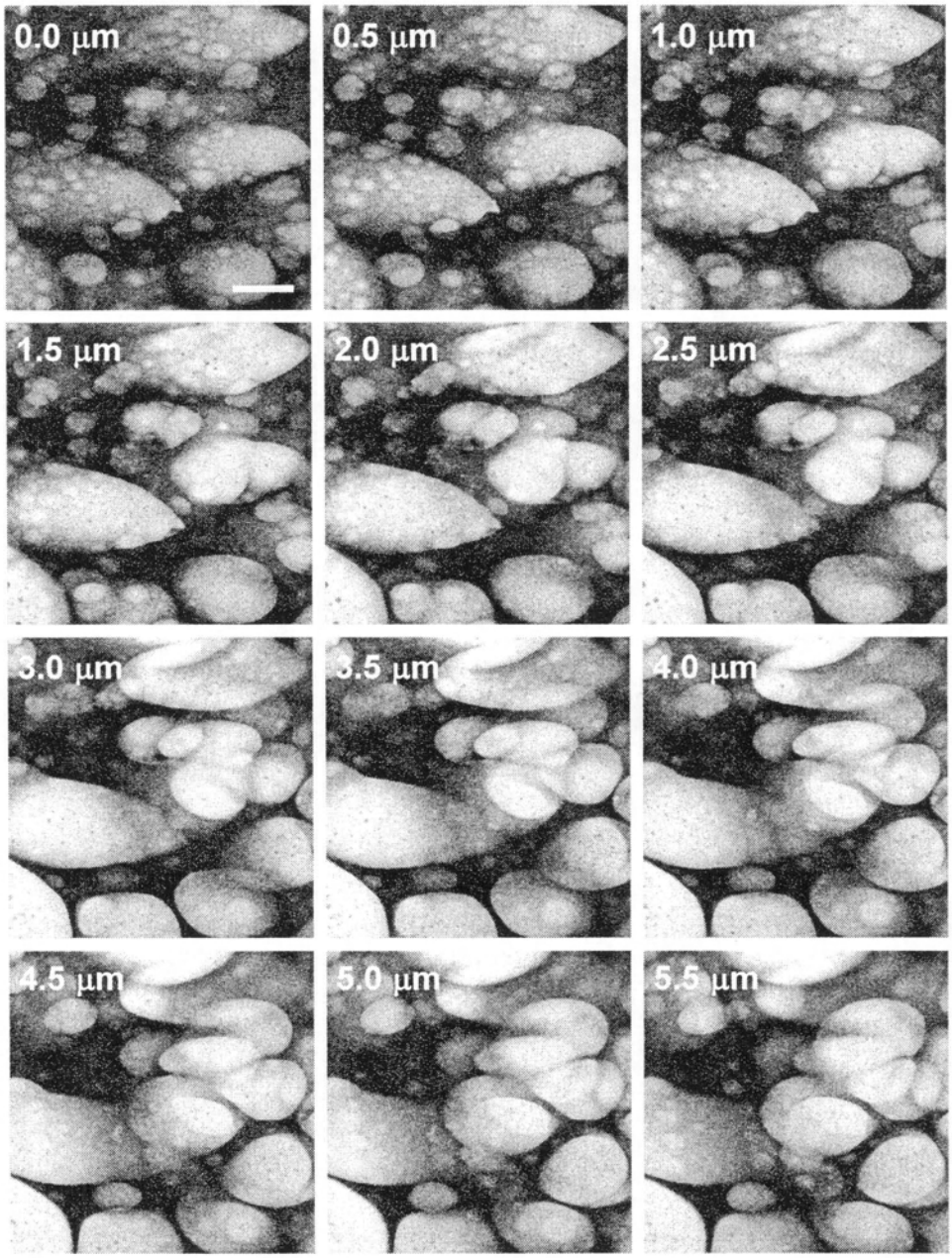

Figure 4.8. *z*-stack of LSCFM images of the 8/32/60 MIC-CdS4/PS(100)/PMMA blend taken at different distances from the glass interface, with 0.5 μm-steps between images. The scale bar represents 20 μm.

However, the transition from substrate to bulk morphology is much less dramatic than in the higher-molecular weight blend, since PMMA remains the continuous phase throughout the film, with no observed phase inversion from the glass substrate to the bulk. Cross-sections of the blend film from a compilation of the *z*-stack (Figure 4.9) reveal that the large PS domains with dimensions in excess of the film thickness are highly elongated in the plane of the film, due to quasi-2D confinement of phase coarsening.

Both of the samples discussed thus far contained a total of 8 wt % MIC-CdS4 tracer, or 20 wt % within the PS phase. In order for MIC-CdS4 to serve as an effective tracer for LSCFM imaging, it should provide suitable fluorescent contrast while having no significant affect on the evolution of phase structure. To explore this, we prepared blends under identical conditions and with identical PS/PMMA compositions (40/60) to those already described, but with both lower and higher contents of MIC-CdS4 in the PS phase. Figure 4.10 shows LSCFM images of both high-molecular weight PS blends (Figure 4.10A & 4.10B) and low-molecular weight PS blends (Figure 4.10C & 4.10D) containing either 4 wt % MIC-CdS4 (10 wt % within the PS phase)or 20 wt % MIC-CdS4 (50 wt % within the PS phase). In all cases, the morphologies are qualitatively identical to those observed using a total of 8 wt % MIC-CdS4. This suggests that the amount of added MIC-CdS4 does not have a significant effect on structure evolution in the investigated composition range, and that the QD tracer does not strongly influence phase separation in these systems. When we consider that the content of tracer is 50 % of the PS phase in the most extreme case, this observation is actually quite remarkable. We point out that TEM analysis of the high-molecular weight PS blend containing 50 % tracer in the PS phase revealed the formation of discrete QD clusters after 8 days

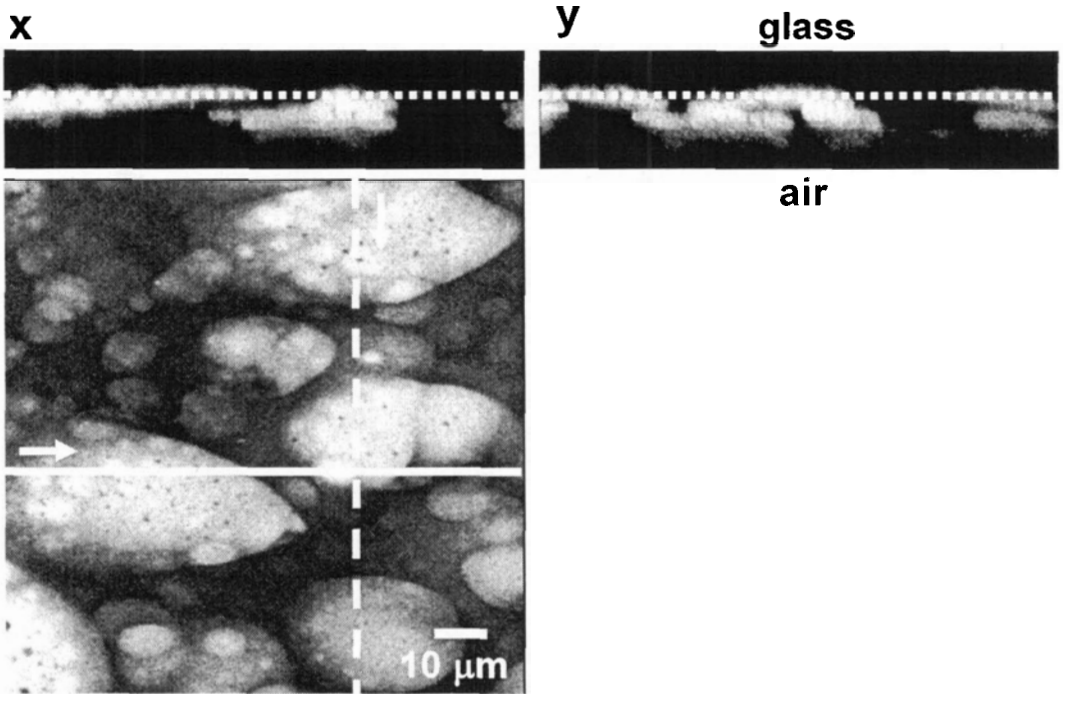

Figure 4.9. Cross-sections of the 8/32/60 MIC-CdS4/PS(100)/PMMA blend taken from a 3D compilation of the *z*-stack. On the *xy* image, the solid line represents the plane of the "*x*" cross-section and the dashed line represents the plane of the "*y*" cross-section. Arrows indicate the "left-to-right" directions in the corresponding cross-sections. The dotted line through the cross-sections represents the plane of the *xy* image

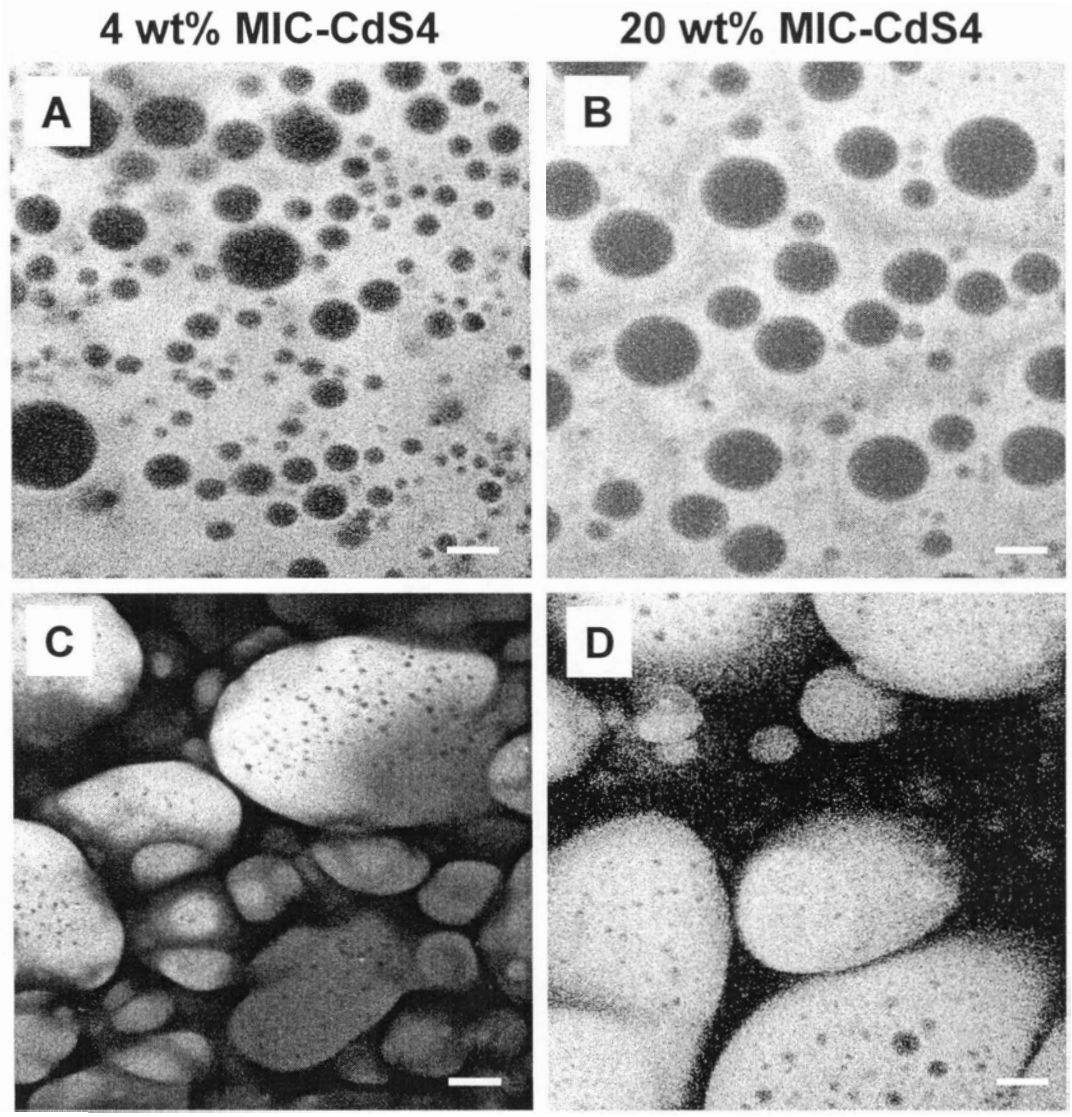

Figure 4.10. LSCFM images of 4/36/60 MIC-CdS4/PS(1250)/PMMA (A), 20/20/60 MIC-CdS4/PS(1250)/PMMA (B), 4/36/60 MIC-CdS4/PS(100)/PMMA (C) , and 20/20/60 MIC-CdS4/PS(100)/PMMA (D). The scale bars represent 10 μm.

annealing, suggesting some phase separation between the matrix and the tracer at the highest tracer content we investigated (Figure 4.11A). Importantly, these clusters contain well defined QDs which are separated by their protective polymer coatings and will therefore maintain their fluorescent properties. As well, the size and separation distances of these clusters within the PS phase are below the optical resolution of LSCFM; therefore, uniform fluorescence in the PS phase is still observed by LSCFM (Figure 4.11B), so that the QDs remain effective tracers despite phase separation on the nanoscale.

To understand the observed insensitivity of morphology to tracer content (Figure 4.10), we consider that in blends containing polydisperse components, entropy favours localization of the lower-molecular weight end of the distribution at the polymer-polymer interface, which will in turn determine the interfacial tension[55] In our system, the QD tracers, which behave as spherical PS brushes, have a much higher molecular weight than either PS(100) or PS(1250) homopolymers, and should therefore be excluded from the PS-PMMA interface. The interfacial tension of the blends, and the resulting morphology, will therefore be determined exclusively by the molecular weight of the PS homopolymer, regardless of the content of added tracer. Thus the polymer brush structure of MIC-CdS4, along with providing good dispersion throughout the PS phase, makes the tracer an additive with little influence on the PS-PMMA interfacial tension via its exclusion from the polymer-polymer interface. This allows more of the tracer to be added, providing greater fluorescence intensity and better phase contrast, without affecting the observed morphology under the present blending conditions of slow solvent evaporation. Of course, the addition of increasing amounts of MIC-CdS4 will increase the average molecular

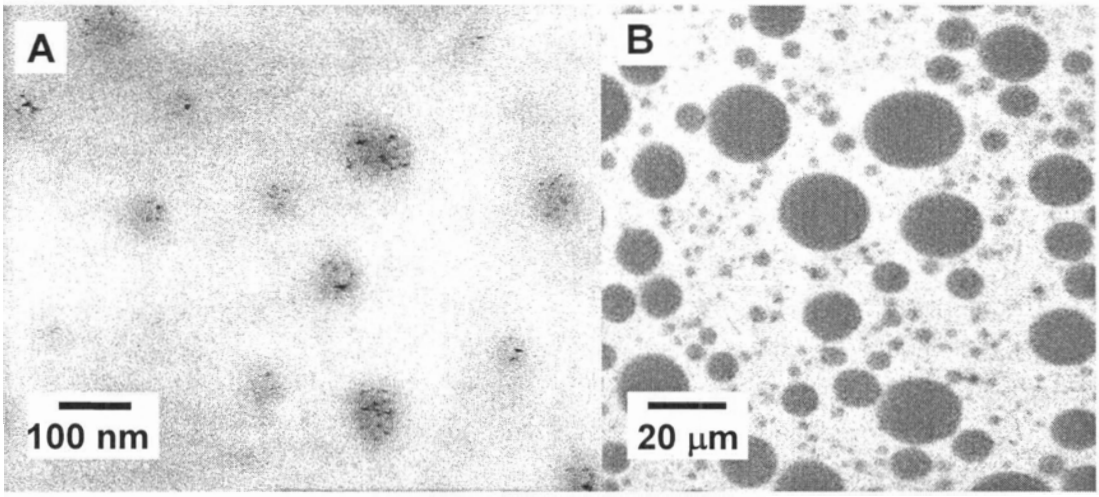

Figure 4.11. TEM of 20/20/60 MIC-CdS4/PS(1250)/PMMA blend after 8 days annealing, showing the formation of QD clusters within the PS phase via nanoscale phase separation (A) and LSCFM image of the same sample, showing that uniform fluorescence in the PS phase is still observed on optical length scales, despite nanoscale phase separation (B).

weight and viscosity of the PS phase, such that morphology evolution under high shear conditions such as melt blending is expected to be more sensitive to the presence of tracer. Therefore, the amount of added quantum dots would have to be kept relatively low for such applications. We point out that even the lowest tracer content investigated in this study (10 wt % in the PS phase) is high compared with the low concentration of fluorescent dyes added in other LSCFM applications. We do not believe that such high tracer contents are a fundamental limitation of this technique, but were employed in this study due to the relatively low quantum yield (QY ~ 2 %) obtained for the present MIC-CdS4 sample.

4.4. Conclusions

In this chapter, we have demonstrated the first use of polymer-coated quantum dots as fluorescent tracers for LSCFM imaging of polymer blend morphology. The quantum dots are stabilized at the surface with a PS-*b*-PAA block copolymer, such that the PAA blocks form an ionic core encapsulating the CdS QDs, and the PS blocks form an external spherical brush, allowing good dispersion of QDs in PS homopolymers of different molecular weights. In 40/60 (w/w) PS/PMMA blends obtained by solvent casting, the quantum dots are dispersed throughout the PS phase and completely excluded from the PMMA phase, providing excellent fluorescence contrast for LSCFM imaging of structure arising from phase separation between PS and PMMA. The percentage of polymer-coated quantum dots within the PS phase was varied from 10 – 50 wt % and was shown to have a negligible effect on the observed blend morphologies. We have used these novel fluorescent tracers to characterize several unique aspects of blend

morphology in solvent-cast 40/60 PS/PMMA blends. When the PS phase contained PS(1250) homopolymer, the bulk blend morphology was made up of spherical and ellipsoidal PMMA droplets (2-25 μm) in a continuous PS matrix, with an inverted morphology of PS islands in a PMMA matrix at the interface with the glass substrate. The surface dependence of the observed morphology is attributed to preferential wetting of the glass by the PMMA component. A very different blend morphology was found for the blend containing PS(100) homopolymer, resulting in phase-in-phase structure with large PS domains (20-100 μm) dispersed in a PMMA continuous phase, and small PMMA domains (1-2 μm) scattered throughout the larger PS droplets. This difference in morphology for equivalent blend composition and preparation conditions is attributed to a difference in interfacial tension, due to very different molecular weights of the PS homopolymer.

4.5. References

(1) Jinnai, H.; Nishikawa, Y.; Koga, T.; Hashimoto, T. *Macromolecules* **1995**, *28*, 4782.

(2) Takeno, H.; Iwata, M.; Takenaka, M.; Hashimoto, T. *Macromolecules* **2000**, *33*, 9657.

(3) Jinnai, H.; Yoshida, H.; Kimishima, K.; Funaki, Y.; Hirokawa, Y.; Ribbe, A. E.; Hashimoto, T. *Macromolecules* **2001**, *34*, 5186.

(4) Hashimoto, T.; Jinnai, H.; Nishikawa, Y.; Koga, T. *Marcomo. Symp.* **2002**, *190*, 9.

(5) Li, L.; Sosnowski, S.; Chaffey, C. E.; Balke, S. T.; Winnik, M. A. *Langmuir* **1994**, *10*, 2495.

(6) Li, L.; Sosnowski, S.; Kumacheva, E.; Winnik, M. A. *Langmuir* **1996**, *12*, 2141.

(7) Kumacheva, E.; Li, L.; Winnik, M. A.; Shinozaki, D. M.; Cheng, P. C. *Langmuir* **1997**, *13*, 2483.

(8) Morris, H. R.; Turner II, J. F.; Munro, B.; Ryntz, R. A.; Treado, P. J. *Langmuir* **1999**, *15*, 2961.

(9) Morris, H. R.; Munro, B.; Ryntz, R. A.; Treado, P. J. *Langmuir* **1998**, *14*, 2426.

(10) Prater, T. J.; Kaberline, S. L.; W., H. J.; Ryntz, R. A. *J. Coat. Technol.* **1996**, *68*, 83.

(11) White, W. R.; Wiltzius, P. *Phys. Rev. Lett.* **1995**, *75*, 3012.

(12) Tong, J.-D.; Moffitt, M.; Huang, X.; Winnik, M. A.; Ryntz, R. A. *J. Polym. Sci. A: Polym. Chem.* **2001**, *39*, 239.

(13) Moffitt, M.; Rharbi, Y.; Li, H.; Winnik, M. A. *Macromolecules* **2002**, *35*, 3321; Moffitt, M.; Rharbi, Y.; Tong, J.-D.; Farhina, J. P. S.; Li, H.; Winnik, M. A.; Zahalka, H. *J. Polym. Sci. B: Polym. Phys.* **2003**, *41*,637.

(14) Moffitt, M.; Rharbi, Y.; Chen, W.; Tong, J.-D.; Winnik, M. A.; Thurman, D. W.; Oberhauser, J. P.; Kornfield, J. A.; Ryntz, R. A. *J. Polym. Sci. B: Polym. Phys.* **2002**, *40*, 2842.

(15) Moon, B.; Hoye, T. R.; Macosko, C. W. *Polymer* **2002**, *43*, 5501.

(16) Bruchez, M.; Moronne, M.; Gin, S.; Weiss, S.; Alivisatos, A. P. *Science* **1998**, *281*, 2013.

(17) Chan, W. C. W.; Nie, S. *Science* **1998**, *281*, 2016.

(18) Han, M.; Gao, X.; Su, J. Z.; Nie, S. *Nature Biotech.* **2001**, *19*, 631.

(19) Dubertret, B.; Skourides, P.; Norris, D. J.; Noireaux, V.; Brivanlou, A. H.; Libchader, A. *Science* **2002**, *298*, 1759.

(20) Larson, D. R.; Zipfel, W. R.; Williams, R. M.; Clark, S. W.; Bruchez, M. P.; Wise, F. W.; Webb, W. W. *Science* **2003**, *300*, 1432.

(21) Wu, X.; Liu, H.; Liu, J.; Haley, K. N.; Treadway, J. A.; Larson, J. P.; Ge, N.; Peale, F.; Bruchez, M. P. *Nature Biotech.* **2003**, *21*, 41.

(22) Lee, J.; Sundar, V. C.; Heine, J. R.; Bawendi, M. G.; Jensen, K. F. *Adv. Mater.* **2000**, *12*, 1102.

(23) Wang, C.-W.; Moffitt, M. *Langmuir* **2004**, *in press.*

(24) Lemon, B. I.; Crooks, R. M. *J. Am. Chem. Soc.* **2000**, *122*, 12886.

(25) Guo, W.; Li, J. J.; Wang, A.; Peng, X. *J. Am. Chem. Soc.* **2003**, *125*, 3091.

(26) Carrot, G.; Scholz, S. M.; Plummer, C. J. G.; Hilborn, J. G.; Hendrick, J. L. *Chem. Mater.* **1999**, *11*.

(27) Erskine, L. L.; Emrick, T.; A.P., A.; J.M.J., F. *Abstr. Pap. Am. Chem. Soc.*, 219:387-POLY Part 212, Mar 226, 2000.

(28) Skaff, H.; Ilker, M. F.; Coughlin, E. B.; Emrick, T. *J. Am. Chem. Soc.* **2002**, *124*, 5729.

(29) Skaff, H.; Emrick, T. *Chem. Comm.* **2003**, 52.

(30) Potapova, I.; Mruk, R.; Prehl, S.; Zentel, R.; Basche, T.; Mews, A. *J. Am. Chem. Soc.* **2003**, *125*, 320.

(31) Wang, X.-S.; Dykstra, T. E.; Salvador, M. R.; Manners, I.; Scholes, G. D.; Winnik, M. A. *J. Am. Chem. Soc.* **2004**, *126*, 7784.

(32) Corbierre, M. K.; Cameron, N. S.; Sutton, M.; Mochrie, S. G. J.; Lurio, L. B.; Ruhm, A.; Lennox, R. B. *J. Am. Chem. Soc.* **2001**, *123*, 10411.

(33) Corbierre, M. K.; Cameron, N. S.; Lennox, R. B. *Langmuir* **2004**, *20*, 2867.

(34) Tanaka, K.; Takahara, A.; Kajiyama, T. *Macromolecules* **1996**, *29*, 3232.

(35) Walhein, S.; Boltau, M.; Mlynek, J.; Krausch, G.; Steiner, U. *Macromolecules* **1997**, *30*, 4995.

(36) Ton-That, C.; Shard, A. G.; Daley, R.; Bradley, R. H. *Macromolecules* **2000**, *33*, 8453.

(37) Harris, M.; Appel, G.; Ade, H. *Macromolecules* **2003**, *36*, 3307.

(38) Moffitt, M.; McMahon, L.; Pessel, V.; Eisenberg, A. *Chem. Mater.* **1995**, *7*, 1185.

(39) Hasegawa, R.; Aoki, Y.; Doi, M. *Macromolecules* **1996**, *29*, 6656.

(40) Ferreira, P. G.; Ajdari, A.; Leibler, L. *Macromolecules* **1998**, *31*, 3994.

(41) Lindenblatt, G.; Schartl, W.; Pakula, T.; Schmidt, M. *Macromolecules* **2000**, *33*, 9340.

(42) Lindenblatt, G.; Schartl, W.; Pakula, T.; Schmidt, M. *Macromolecules* **2001**, *34*, 1730.

(43) Yezek, L.; Schartl, W.; Chen, Y.; Gohr, K.; Schmidt, M. *Macromolecules* **2003**, *36*, 4226.

(44) Leibler, L.; Pincus, P. A. *Macromolecules* **1984**, *17*, 2922.

(45) Koizumi, S.; Hasegawa, H.; Hashimoto, T. *Macromolecules* **1994**, *27*, 6532.

(46) Daoud, M.; Cotton, J. P. *J. Phys. (Paris)* **1982**, *43*, 531.

(47) Lin, E. K.; Gast, A. P. *Macromolecules* **1996**, *29*, 390.

(48) Burchard, W. *Adv. Polym. Sci.* **1983**, *48*, 1.

(49) Forster, S.; Zisenis, M.; Wenz, E.; Antonietti, M. *J. Chem. Phys.* **1996**, *104*, 9956.

(50) Lee, J. K.; Han, C. D. *Polymer* **1999**, *40*, 2521.

(51) Walheim, S.; Ramstein, M.; Steiner, U. *Langmuir* **1999**, *15*, 4828.

(52) Chang, L. L.; Woo, E. M. *Macromol. Chem. Phys.* **2001**, *202*, 636.

(53) Paul, D. R.; Bucknall, C. B. *Polymer Blends Vol 1: Formulation*; Wiley-Interscience, 2000.

(54) Anastasiadis, S. H.; Gancarz, I.; Koberstein, J. T. *Macromolecules* **1988**, *21*, 2980.

(55) Broseta, D.; Fredrickson, G. H.; Helfand, E.; Leibler, L. *Macromolecules* **1990**, *23*, 132.